Universidad Autónoma de Madrid

Departamento de Física de Materiales

Synthesis and characterization of Ag_2S-based nanoparticles as luminescence nanothermomethers.

Diego Ruiz Gómez

Madrid, 2019

Abstract

The study and applications of semiconductor nanoparticles (NPs) have grown in the last 30 years due to their attractive and exceptional optical and electronic properties. Their highly efficient photo- and electroluminescence is tunable in a wide range of the electromagnetic spectrum, allowing the preparation of NPs with an emission centered form the UV to the mid infrared range. Their reduced size is one of the attractive features for some applications in biology such as drug-delivery or selective bio-labelling. Due to their small size (comparable to that of proteins or nucleic acids), semiconductor NPs can be coupled to biological molecules and with them reach the inside of cells, what has been vastly developed for fluorescent optical tracking both *in vitro* and *in vivo*. The high absorption and scattering of biomolecules and tissues in the Vis range has trigger the seek of other non-toxic NPs whose optical response is centered in the second or third biological windows, NIR spectral ranges where light extinction is minimized. In this way, some NIR NPs can result in higher spatial resolution, deeper tissue penetration, and improved overall image quality. Silver sulfide (Ag_2S) based NPs have been appointed as one of the most promising materials since they are not toxic and their photoluminescence centered in the NIR region. The synthesis of Ag_2S NPs dates from the mid-90's although their interest has started growing in the last 10 years. The easy preparation of bright NPs with a photoluminescence centered in the region called NIR-II (1000-1400 nm) triggered their use in many biological assays with positive results in imaging, targeting and therapy experiments with negligible toxicity making this material more adequate than other semiconductors like Pb or Hg chalcogenides. In Chapter 2 it is described how these appealing properties are taken advantage by adding a previously not studied property: their capability to be used as luminescence thermometers (LThs) in the NIR-II

range. The as-synthesized NPs were thoroughly characterized, and transferred to water using a newly developed one-step procedure. This ligand exchange step preserves their thermometric sensitivity as evidenced in their use for the *in vivo* monitoring of the temperature change in a mouse's brain during a heating/cooling experiment. Furthermore, these previously described routes are found to produce NPs with a dense surface coating and embedded in the silver precursor formed in the course of the synthesis reaction. In Chapter 3, a new synthetic route is developed to obtain NPs with a lighter surface coating that allow for a more versatile and efficient ligand exchange procedure. Moreover, the preparation of monodisperse individual NPs using this new route allows for the preparation of other structures based on Ag_2S NPs: $Ag_2S/Ag_2(S,Se)$ and $Ag_2S/Ag_2(S,Se)$ /ZnS core/shell NPs. Both structures show higher PLQY and improved stability towards oxidation while retaining their labile surface that allows the easy tuning of their surface chemistry. In the case of the CS NPs their surface can be coated with different biocompatible polymers and even with oligonucleotides, biomolecules that may be biologically active allowing the targeting of specific sequences. In Chapter 4, the preparation of multifunctional composites is explored using two different approaches. These composites consist on a single nanostructure able to simultaneously produce hyperthermia (either optical or magnetic) and provide temperature reading to prevent undesired damage in healthy zones. The correct formation of these composites is achieved by the encapsulation of Iron Oxide Superparamagnetic Nanoparticles (SPIONs) and Ag_2S-based NPs inside a sphere formed by a stack of bilayers of a polyethylene glycol modified phospholipid. These liposomes, with a hydrodynamic size of around 100 nm are of an ideal size for their use in living organisms. Incipient cell culture studies suggest their correct internalization in cells, opening the door for simultaneous heating and temperature control in cancer cells.

Resumen

El estudio y las aplicaciones de las nanopartículas (NP) basadas en semiconductores ha crecido en los últimos 30 años gracias a sus atractivas y excepcionales propiedades ópticas y electrónicas. Su alta eficiencia en procesos de foto y electroluminiscencia se puede sintonizar en un amplio range del espectro electromagnético, favoreciendo la preparación de NPs con una emisión desde el rango ultravioleta hasta el infrarrojo medio. Su tamaño reducido es uno de los principales rasgos que las hace atractivas para ciertas aplicaciones en biología como para la liberación de fármacos o el marcaje selectivo. Dado que su tamaño es parecido al de proteínas y ácidos nucleicos, las NPs semiconductoras pueden asociarse con moléculas biológicas de forma que pueden penetrar en células. Este hecho ha sido ampliamente desarrollado para el marcaje tanto *in vitro* como *in vivo*.

El alto coeficiente de absorción y de dispersión de la luz de los tejidos y las biomoléculas en el rango de luz visible ha hecho que aumente el interés en la búsqueda de NPs con respuesta óptica en las llamadas "segunda y tercera ventana biológica"; regiones del espectro donde laa extinción de luz es mínima. De esta forma, algunas NPs con emisión en el rango infrarrojo cercano (NIR, en sus siglas en inglés) permiten un aumento en la resolución, penetración en tejido y, en general, una mayor calidad de las imágenes obtenidas con su fluorescencia. Las NPs basadas en sulfuro de plata (Ag_2S) han sido identificadas como uno de los materiales más prometedores dado que no son tóxicas y por su emisión en el rango NIR. . La síntesis de este tipo de NPs data de mediados de los años 90, aunque su interés ha aumentado exponencialmente en los últimos 10 años. La fácil preparación de estas NPs ha aumentado su uso para diversas aplicaciones como imagen por fluorescencia, marcaje o experimentos terapéuticos sin toxicidad apreciada probando ser un material mucho más adecuado para estos usos que otros

materiales con emisión en el rango NIR como los calcogenuros de plomo o mercurio.En el capítulo 2, se describe como a las ya valiosas propiedades de este material se añade otra nueva: su capacidad para ser termómetros de luminiscencia en el rango NIR-II (situado entre 1000-1400 nm). Las NPs sintetizadas han sido caracterizadas de forma exhaustiva y transferidas a medios acuosos usando una nueva metodología de un solo paso. Este procedimiento de cambio de ligando preserva sus propiedades termométricas con alta sensibilidad como se evidencia en un experimento donde se observa a tiempo real el cambio de temperatura en un ratón vivo después de un proceso de calentamiento y enfriamiento. Además, gracias a una serie de estudios por Difracción de Rayos X y Resonancia Magnética Nuclear se ha descubierto que las rutas para la síntesis de este tipo de NPs hacen que se encuentren en una densa matriz de un precursor generado en la síntesis. En el capítulo 3, una nueva ruta de síntesis es desarrollada para obtener NPs con un recubrimiento superficial más ligero, obteniendo un mayor rendimiento en el paso de cambio de ligando. La obtención de estas NPs libres posibilita su uso como semillas para producción de otras estructuras más complejas como $Ag_2S/Ag_2(S,Se)$ y $Ag_2S/Ag_2(S,Se)/ZnS$. Ambas estructuras muestra un mayor rendimiento cuántico y una mayor estabilidad química frente a la oxidación mientras retienen su superficie lábil que permite una mayor versatilidad en su química en superficie. En el caso de las NPs $Ag_2S/Ag_2(S,Se)/ZnS$, la capa de sulfuro de zinc permite que su superficie sea recubierta por una serie de polímeros biocompatibles e incluso con oligonucleótidos, biomoléculas que pueden ser biológicamente activas permitiendo dirigirse a ciertas secuencias específicas de nucleótidos complementarios. En el capítulo 4, se explora la preparación de compuestos multifuncionales con dos estrategias distintas. Estos compuestos consisten en una sola nanoestructura que es capaz simultáneamente de producir una hipertermia (óptica o magnética) y dar una lectura de temperatura de forma

que se puede prevenir el daño en zonas sanas. La correcta formación de estos compuestos se consigue con la encapsulación de NPs de óxido de hierro (Fe_3O_4) y las previamente sintetizadas NPs basadas en Ag_2S dentro de una esfera formada por varias bicapas de un fosfolípido modificado con un extremo de polietilenglicol. Estos liposomas, que tienen un radio hidrodinámico de alrededor de 100 nm son de un tamaño ideal para su correcta internalización dentro de células cancerosas. De esta forma, estos compuestos son potencialmente útiles para conseguir ajustar la dosis de hipertermia causando el mínimo daño posible a zonas no tumorales.

Tabla de contenido

Chapter 1. Introduction

1.1. Nanoparticles

Thanks to profuse studies and synthetic efforts during the last 30 years, the amount of materials successfully synthesized in the form of nanoparticles (NPs) or nanocrystals (NCs) is enormous nowadays, and is still growing. Nanoparticles are defined as materials having at least one characteristic length scale in the range 1-100 nm, and with at least one property being considerably different from that of the bulk counterpart as a result of their nanoscale dimensions.[1] Their properties depend on the nature of the material they are made of (metallic, magnetic, semiconductor, dielectric, etc.). The applications of the different kinds of NPs are already numerous and range from optoelectronics [2] to biomedicine.[3] The important relation between the size and the optical, electronic or magnetic properties of nanomaterials has opened a new era in which many important issues regarding different aspects of science or technology can be overcome by the correct tuning of the size, aspect ratio or chemical composition of a particular material.

Concerning the properties that arise different from that of their bulk counterpart as a result of the nanoscale size, in the case of ferromagnetic materials, when the size of the crystals starts to approximate the size of the magnetic domain, important changes in their magnetic properties are observed. This change is evidenced in the appearance of two different magnetic behaviors: single domain ferromagnetism and superparamagnetism (SPM). Among the ferromagnetic materials synthesized as NPs, iron oxide-based NPs and, in particular, Fe_3O_4 NPs or SPIONs (Superparamagnetic Iron Oxide Nanoparticles), are the most popular. When the size of these NPs is reduced to less than 30-50 nm the material losses its ferromagnetic behavior and exhibits superparamagnetism.[4, 5] Superparamagnetism consists in the ability of these nanocrystals to show high susceptibility and saturation magnetization when an external magnetic field is applied, and the capacity to lose it when the field is stopped without remanence. This behavior is analogous to paramagnetism but, instead of individual electronic spins displaying the response, in SPM it is the collective moment of the whole NP.[6] Hyperthermia treatments, one of the main applications of these NPs, are based on this unique property. These treatments consist in the intentional heating of a certain region of the body in order to achieve a therapeutic effect. Magnetic hyperthermia therapy has been extensively studies for the treatment of certain kinds of localized malignant tumors.[7] The temperature increase of the cancerous cells up to 41-42°C promotes the malfunction of different regulatory

biological mechanisms like cell growth and differentiation, transmembrane transport and the inhibition of repair enzymes that correct DNA.[8] All these effects promote different types of cell death, thus reducing the tumor. Due to the high absorption coefficient of iron oxide NPs, both visible light and magnetic fields can be used to induce heat in different biological entities (cells, tissues, organelles, etc.). Furthermore, the low toxicity of iron, which is found in some biomolecules like ferritine, has promoted their use for the treatment of a wide variety of tumors with promising results and negligible toxicity.[9]

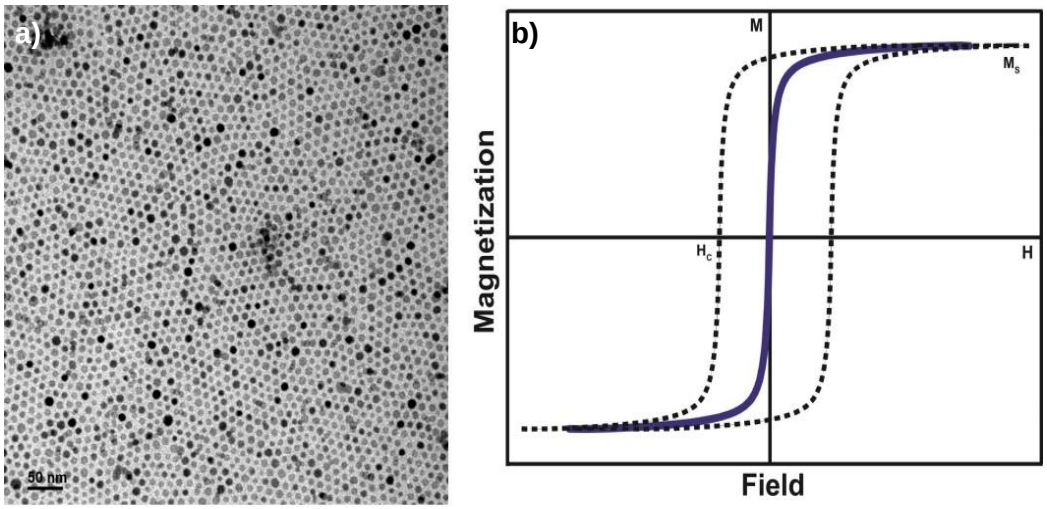

Figure 1.1. a) TEM image of Superparamagnetic Iron Oxide Nanoparticles (NPs) b) Comparison between the evolution of the magnetization of the SPIONs when an external magnetic field is applied. The black dotted line represents a ferromagnetic material and the blue continuous line SPM NPs. TEM image courtesy of Dr. Gorka Salas.

On the other hand, metallic NPs have been successfully synthesized at the nanoscale. Metals like gold, silver, copper, palladium or bismuth show attractive properties when their size is decreased.[10] These features include the localization of surface plasmons, whose resonance can be tuned by the variation of several factors like their chemical composition, their size and morphology. The main applications of these NPs include catalysis, drug delivery, photothermal therapies, tumor targeting, as well as Surface Enhanced Raman Spectroscopy (SERS), due to the position of their localized surface plasmon resonance (LSPR) in the visible range.[11]

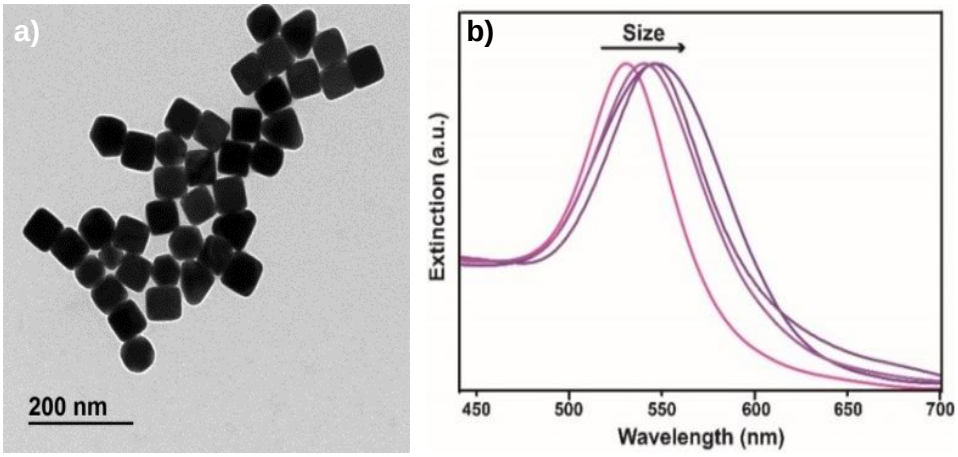

Figure 1.2. a) TEM image of gold nanocubes b) LSPR dependence with the size of the gold nanocubes

1.2. Semiconductor nanoparticles

In the case of semiconductor NPs, when their size is reduced to be close to 2 times the exciton Bohr radius for the material, their charge carriers undergo an energetic confinement. These NPs are then known as Quantum Dots (QDs). The confinement of the valence and conduction band electrons in the 3 dimensions causes the quantization of the energy levels and the increase of the bandgap energy. The discretization of levels causes the improvement of the Photoluminescence Quantum Yield (PLQY) of optical transitions, hence turning the NPs in more efficient emitters compared to their bulk counterpart. In the quantum confinement regime, the energy levels can be calculated using the model of a *particle in a box*.[1] This calculation was first resolved by Brus[12] in the equation named after him (Brus equation, equation 1), where Eg is the bulk semiconductor bandgap, R the radius of the crystal, m_e and m_h the effective mass of the electron and hole in the valence band, respectively, and ε the dielectric constant of the material.

As can be observed in equation 1.1, the increase in the Eg is inversely proportional to the radius of the NPs to the square. This strong dependence between the bandgap and the size of the NP explains the large tunability in the optical properties of several semiconductors.

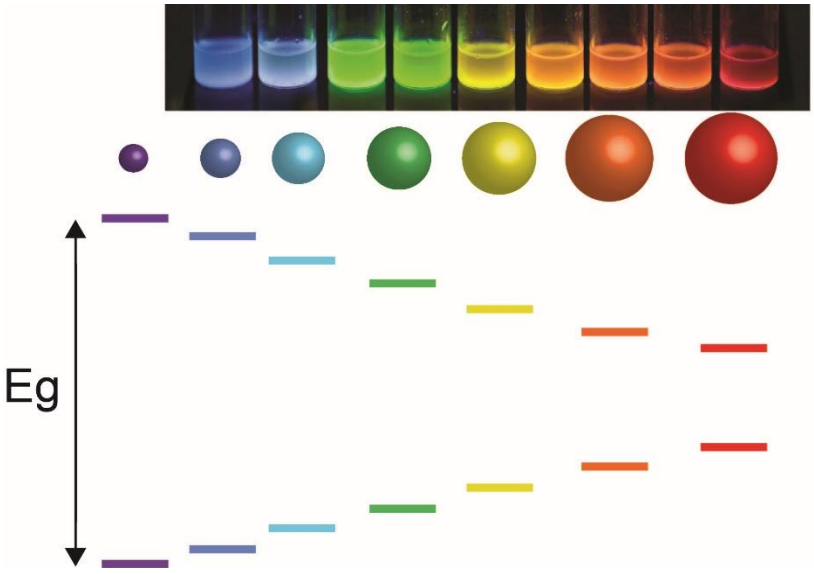

$$E = E_g + \frac{h^2}{8R^2}\left(\frac{1}{m_e} + \frac{1}{m_h}\right) - \frac{1.8e^2}{4\pi\varepsilon R^2} \quad (1.1)$$

Figure 1.3. The dependence of the optical bandgap with the size of the NP in semiconductor materials allows to tune their PL in a wide range for some materials. This behavior is given by the Brus equation (Equation 1.1).

As described in equation 1.1, the change in the energy bandgap of the nanomaterial depends not only on the size of the crystal but also on the intrinsic properties of the material. This way, due to these intrinsic properties (refraction index, curvature of the valence and conduction bands, etc) of every semiconductor, some are more "easily tunable" than others. All these magnitudes affect the Bohr radius of the exciton, which is directly proportional to the binding energy of the electron and the hole. So, for excitons with a big radius (low binding energy) the quantum confinement regime will be wider, allowing for high optical properties tunability, and, on the contrary, for materials with a tightly bound exciton (low radius), only in very reduced sizes the strong quantum confinement regime will be achieved. Depending on the relative size of the NP and the Bohr radius, the quantum confinement can be strong or weak. The strong quantum confinement regime applies when the NP size is less than twice the exciton Bohr radius (twice the "size" of the exciton). In contrast, in the weak confinement regime, the electrons are not fully confined thus not following the *particle in a box* approach. In this case the electrons wavefunction is not fully confined in the NP[13] showing properties that are intermediate between the bulk semiconductor and the strong quantum confinement regime.

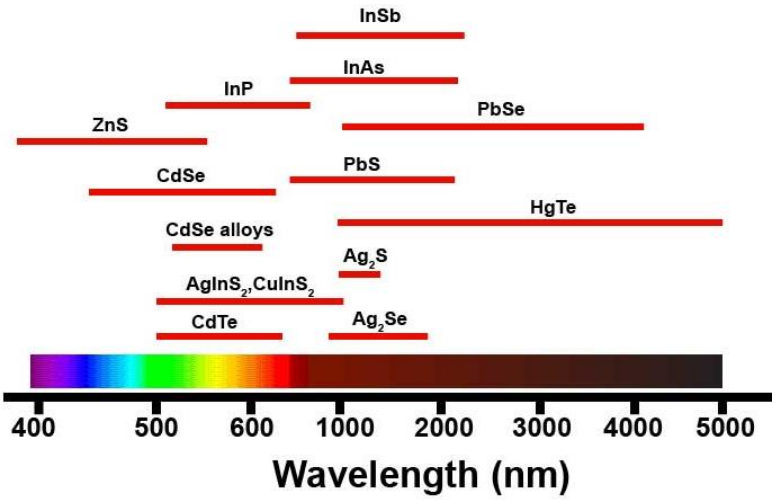

Figure 1.4. PL tunability of some of the most well-known semiconductor NPs

One of the most important properties to characterize the quality of a luminescent NP, such as QDs, is their Photoluminescence Quantum Yield (PLQY,$\boldsymbol{\Phi}$) which is defined as:

$$\boldsymbol{\Phi} = \frac{\boldsymbol{emitted\ photons}}{\boldsymbol{absorbed\ photons}} \quad (1.2)$$

This magnitude measures how efficient the light emission is, depending on the absorption. The process of photoluminescence (PL) in NPs is affected by several factors like the presence of surface traps, a consequence of a poorly capped surface or imperfections in the crystalline structure, including the presence of impurities. The optimization of synthetic methods at high temperature in inert atmosphere has successfully reduced the PL quenching through non-radiative processes due to poor crystallinity. However, the most efficient approach to increase the PLQY has been the formation of core/shell (CS) structures, an approach that drastically reduces surface traps and localizes charge carriers selectively in the core or shell materials. To produce CS NPs it is necessary the controlled growth of a few layers of a different semiconductor material around that of the emissive core. The band alignment between the core and shell materials is one of the key factors that will determine the optical response of the hybrid structure. In general, CS NPs are classified in 4 types depicted in Figure 1.5.

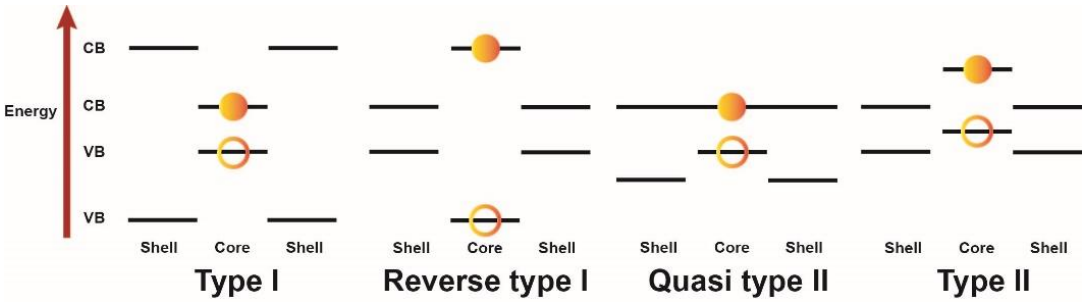

Figure 1.5. Types of core/shell nanostructures depending on the relative position of the energy levels of the core and shell materials.

In order to obtain more efficient emitters, type I CS structures are pursued. In these structures, the gap of the outer semiconductor material is larger than that of the core, what forces the hole and the electron wavefunctions to be confined inside the core material. This strategy prevents losses by recombination of the charge carriers in the shell and makes the radiative processes in the core more efficient. In the case of reverse type I alignment, the bands of the shelling material fall inside the bands of the core material favoring the delocalization of both charge carriers in the whole structure. In this kind of CS NPs the extraction of both charge carriers from the structure is favored. In quasi type II configuration, only one carrier is confined inside the core of the NC while the other is partially delocalized over the whole structure due to the small energy difference of both materials' conduction bands. This is case of CdSe/CdS NPs. The growth of the CdS covering layer around the CdSe core is observed as a slight red shift in both the absorption features and the PL energy due to the loss of quantum confinement. If the position of the bands is staggered the conformation is known as type II. In these structures the charge carriers are spatially separated in the core and shell materials, respectively, thus, reducing the effective band gap. The optical properties of these structures are characterized by a large red shift of the emission energy (although it significantly reduces the PLQY), and are of special interest in the development of photovoltaic devices including solar cells. The separation of the charge carrier allows for the extraction of the charge carriers by an external applied bias, therefore obtaining photocurrent.

1.3. Near infrared emitting semiconductor NPs

The interest of luminescent NPs operating at the near infrared range (NIR, region between 700-1400 nm) points towards the development of IR photovoltaic devices[14, 15] and their use in biomedical applications.[16] The latter is a side effect of their advantages in biological media compared to QDs emitting in the visible region (380-700 nm). Visible light is strongly attenuated when it goes through biological tissues, which effectively reduces the optical

penetration of visible-emitting NPs, as exemplified in Figure 1.6.a. In this figure, it can be observed how the scattering and absorption of water and biomolecules, as well as autofluorescence, are reduced in the NIR region. There are two spectral regions were the optical extinction in tissues is particularly reduced: NIR-I (700-1000), and specially in NIR-II (1000-1400 nm).[17, 18]

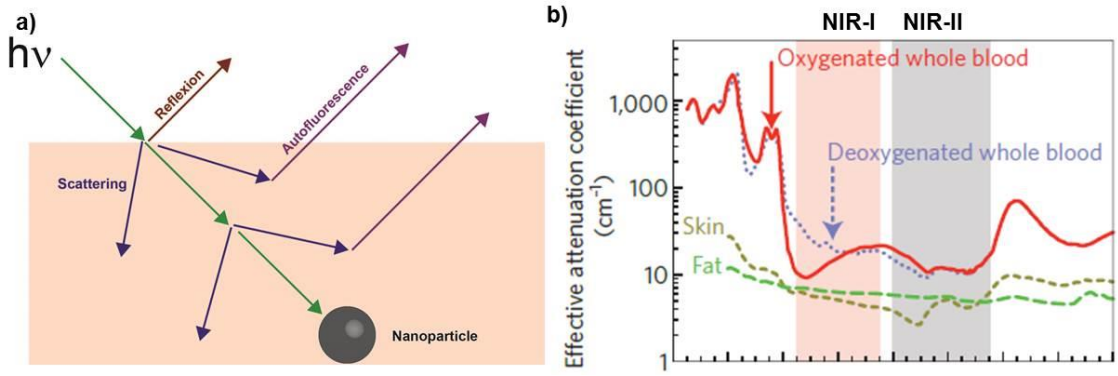

Figure 1.6. a) Scheme of the different processes that light undergoes when it is applied to a biological tissue, b) Representation of the optical absorption of different parts of the body. It can be observed how absorption is minimized in the NIR-I and NIR-II regions. Reproduced with permission from reference [18]

Therefore, the preparation of highly efficient NPs working in the NIR-II range would allow higher penetration depths and, as a result, higher resolution imaging than using visible emitting QDs. Among colloidal semiconductor NPs with optical properties centered in the IR range, lead chalcogenides QDs stand out due to the wide variety of reported synthetic routes that allow controlling their size, morphology, and surface chemistry.[19] Furthermore, the optical properties of lead chalcogenides QDs can be tuned from the red to the mid-IR due to the high exciton Bohr radius in these materials (20 nm for PbS and 46 nm for PbSe[20]) allowing selecting the required PL range at will. Their crystalline structure also allows the formation of CS structures by the shelling with CdS, ZnSe or ZnS with PLQY as high as 60%.[21] Lead-based NPs have already been used in successful experiments of *in vivo*[22-24] imaging and they are also being studied for their use in solar cells due to the unique transport and electronic properties including the multiple exciton generation (MEG), a mechanism that allows for the extraction of various photons from one energetic photon increasing the efficiency of solar cells.[25] HgTe and $Cd_{1-x}Hg_xTe$ NPs also show remarkable PLQY for core-only NPs (40%)[26] and can be tuned from the NIR to the mid-IR. However, as in the case of Pb-based NPs, the use of heavy and toxic metals still raises questions about their biocompatibility although they have been successfully used in some bioimaging studies.[27] Other semiconductor NPs, whose emission covers this range are based on compounds of the I-VI and I-III-VI groups of the periodic table. I-III-VI NPs

include $AgInS_2$, $CuInS_2$ and $CuInSe_2$. Since these materials form solid solutions with different ratios of the components, their optical properties can be widely modified, not only by the variation of size but also by varying their chemical composition. It has been observed that an increasing Ag content[28] in $AgInS_2$ NPs yields high PLQY, evidencing that small changes in the chemical composition of the crystals entails a drastic change in their properties. Using different solid solutions the optical properties can be enhanced as in the case of Ga^{3+} containing $AgInS_2$ NPs with a remarkable PLQY of about 45% emitting in the NIR range.[29]

Among all transition metal chalcogenides with valence I, only silver-based NPs show PL in the NIR region (copper chalcogenides show LSPR absorption). Ag_2Se has been synthesized in different sizes allowing for a PL tuning between 1000-2000 nm. Different *in vivo* imaging studies have been carried out using Ag_2Se[30-32] although there are concerns about the use of Se in living organism. Since the main subject of this Thesis is Ag_2S, a more detailed analysis of this semiconductor based on elements from groups I-VI is developed in the next section.

In the case of lanthanide containing NPs, the generated PL signal does not come from the emission of a semiconductor in a quantum confinement regime but from the available energy levels in lanthanide cations included in different matrices, like $NaYF_4$ or $NaGaF_4$. The great number of emissive levels in these elements allows for the emission from the red to the NIR by the variation of the lanthanide used or combinations of more than one. Lanthanides emitting in the NIR range vastly employed are: Er^{3+}, Tm^{3+}, Ho^{3+} and Pr^{3+}. They are normally used in the presence of a photosensitizer (Yb^{3+} or Nd^{3+}). Some advantageous properties of lanthanide doped NPs are their long luminescence decay times, that allows overcoming autofluorescence signals using a time gated mode and their high photostability with negligible photobleaching or photo-blinking. In addition, synthetic strategies to increase absorption include the formation of CS structures.[33]

1.4. Silver sulfide (Ag_2S)

Even though the first reported synthetic routes for the preparation of Ag_2S NPs dates from 25 years ago,[34] the interest in these NPs is relatively recent compared to other more extensively studied chalcogenide NPs, like CdSe or PbS. The interest in these NPs has grown in the last 10 years principally in the biological context due to their low toxicity and NIR emission. In its bulk form, this semiconductor was described in 1833 by Michael Faraday that discovered his insulator behavior that changed upon heating to a high conductor at elevated temperature. This behavior is caused by the crystalline nature of Ag_2S that presents a monoclinic phase (α)

up to 178°C. Above that temperature, the lattice melts obtaining very high values of ionic conductivity near the phase change. Afterwards, the lattice forms a body-centered cubic structure (β) and, with further heating, a face-centered cubic (γ, above 600°C).

1.4.1 Synthesis methods

The first route for the synthesis of semiconductor NPs was developed by Murray et al[35] in 1993, and it is known as the "hot injection method". This method consists on the injection of organometallic precursors in a solution at high temperature of organic molecules that bind to the surface of the nuclei controlling their size and morphology. This procedure allows the separation between the nucleation and growth steps proposed in 1950 by La Mer and Dinegar,[36] producing NPs with a narrow size distribution. Another useful technique to this aim is the method known as "heat-up". In this case, the precursors are all placed inside the reaction flask and heated controllably until the nucleation stage starts. Although using this method the separation between nucleation and growth is harder to control, different strategies have been developed to obtain monodispersed NPs even in high quantities.[37] The synthesis of Ag_2S NPs was first reported by the group of Dr. Henglein[38] using a simple coprecipitation reaction, which occurs rapidly due to the low solubility product of Ag_2S ($K_s=6.3\cdot10^{-51}$). Afterwards, M. P. Pileni reported the use of a reverse microemulsion system.[39-42] For this synthesis, the polar phase (water) contained $AgNO_3$, which is the most used silver salt due to its high stability. The non-polar medium consisted on a solution of dodecanethiol in toluene. Dioctyl sulfosuccinate (AOT) was used as the surfactant to form the emulsion. However, no PL were reported in any of the previously mentioned methods. The preparation of Ag_2S NPs with different sizes and emission ranges have been successfully carried out by means of any of these two synthetic procedures.

1.4.1.1. Synthesis methods in polar media

The main advantage of synthesizing Ag_2S NPs in polar media is their solubility in water. Their hydrophilic surface ligands allow for their use in biological media which easies the way for their functionalization with biologically active biomolecules.

The heat-up synthetic routes for the synthesis of Ag_2S NPs in polar media consist mainly on the thermal decomposition of small thiolated molecules, like 1,2-dimercaptosuccinic acid (DMSA)[43] or 3-mercaptopropionic acid (MPA),[44] which are used both as the sulfur source and ligand. The carboxylate termination of these two molecules allow for the direct functionalization of these

NPs. For example, Tang et al[45] through EDC/NHS chemistry attached the peptide cRGDfK that targets the $\alpha_v\beta_3$ receptor, which is up-regulated in tumor cells, observing how the NPs accumulated in the tumor area. More recently, Zhang et al[46] achieved the electrostatic bond between the negatively charged groups of MPA and a positively charged histidine end of an affibody targeting a growth factor in small tumors. Also using the EDC/NHS chemistry, Wang et al[47] attached an antagonist of a receptor found in highly metastatic tumor cells being able to identify them and slowing their growth.

In the case of hot injection syntheses for Ag_2S NPs, the reaction temperature is limited to 100°C and the injection normally consists on a solution containing Na_2S or sulfur powder dissolved in hydrazine.[48-50] The hot injection routes using these sulfur precursors allow for the use of biomolecules as reaction ligands: A Cys modified DNA aptamer, proteins like β-Lactoglobulin[51] (β-LG), Bovine Serum Albumin (BSA) and Human Serum Albumin[52] (HSA) or small peptides like glutathione (GSH) have been used in these kinds of syntheses.[48, 49] The Ag_2S NPs synthesized using HSA were prepared by Yang et al[52] showing a NIR-II emission centered at 1060 nm, inside the II-BW, although in general NPs synthesized using these routes do not emit in the NIR-II range as discussed in Section 4.2.

1.4.1.2. Synthesis methods in non-polar media

The synthetic methods in non-polar media are also widely used for the synthesis of this kind of NPs. The most popular routes are the heat-up based on silver (I) diethyldithiocarbamate (AgDDTC), a commercial salt that allows the formation of Ag_2S NPs in the presence and absence of thiols, firstly reported by Du et al.[53] These routes are popular due to the easy synthetic procedure and the moderately high temperatures necessary (T<220°C).

Hot injection routes in non-polar media have also been reported for this kind of NPs. Using an extremely reactive sulfur source like bis(trimethylsilyl) sulfide (TMS), monodisperse NPs can be synthesized. Jiang et al achieved a synthetic procedure based on seeded growth allowing for huge PL tunability from 700 to 1200 nm.[54] The injection of other highly reactive sulfur source like $(NH_4)_2S$ has also been reported as a useful precursor for Ag_2S NPs. Its use allowed for a gram-scale synthesis of these NPs.[55] However, TMS and $(NH_4)_2S$ are unwanted chemicals in NPs synthesis due to their high reactivity and toxicity, what requires well-controlled inert conditions and make the system non-straightforward to handle. For this reason, other milder sulfur precursors have been used for the synthesis of these NPs like sulfur powder[56] or sulfur dissolved in Toluene,[57] Oleylamine[58] or Trioctylphophine.[59] All these routes yield hydrophobic

NPs that need an extra step to be dispersed in aqueous media. In general, there are two main strategies to obtain hydrophilic NPs: ligand exchange or encapsulation.

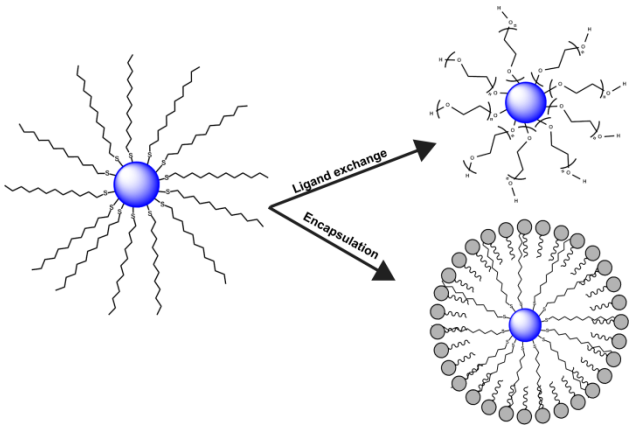

Figure 1.7. Different strategies for the water-solubilization of NPs

Ligand exchange

In this approach, the hydrophobic organic molecules used in the synthesis of the NPs may participate forming intermediates, controlling size and shape, or passivate the final NPs surface are replaced by new ones that provides aqueous solubility. The methodology requires the use of high excess of ligands with higher binding energy to the semiconductor surface than the original one. The choice of the hydrophilic ligand and the ligand exchange procedure is key in order to minimize the PLQY loss during the ligand-exchange process. The decrease in PLQY is a concomitant effect due to the generation of surface imperfections acting as surface-trap states that increase the probability of non-radiative exciton deactivation processes. Other possible sources of the PLQY drop includes other parameters like the relative energy levels of the molecule attached to a particular surface atom (*e.g.*, sulfur atoms forming part of ligands have been observed to attract charge and thus reduce the PLQY).[60, 61] In the case of Ag_2S NPs synthesized by heat-up routes, Hong et al[62] developed a two-step ligand exchange procedure to obtain fully stable NPs in aqueous media. The first ligand exchange is carried out using a multifunctional thiol-containing molecule like dihydrolipoic acid (DHLA). After that, the carboxylate ending (not bound to the surface of the NC) is activated to introduce a multifunctional PEG-based polymer.

Encapsulation

The encapsulation of the NPs is an alternative procedure that can be followed if the hydrophobic ligands are tightly bound or the ligand exchange process causes an important

quenching of the PL. Different strategies have been developed for the encapsulation of NPs depending on the matrix that will contain them. The introduction of NPs inside SiO_2 spheres is a popular strategy due to the possibility of controlling the sphere size with a narrow size distribution.[63] This strategy also contributes to avoid the release of metallic ions that could harm biological entities. Amphiphilic polymers like polyvinyl alcohol (PVA), poly(lactic-*co*-glycolic-acid) (PLGA) or different co-polymers based on poly(ethylene oxide) (PEO) have also been used for the formation of NPs capsules.[64] The encapsulation mechanism includes the interaction of these polymers with the passivating ligand sphere of the NPs and therefore, does not affect the surface of the NPs, what drastically reduces the generation of surface states. Other explored strategies for the encapsulation of NPs consist in the use of phospholipids or their modifications with PEG-based polymers.[65] These molecules are also amphiphilic and show some extra advantages like high biocompatibility, the possibility of forming micelles of different sizes and high interaction with cell membranes, facilitating cell-cultured studies.

1.4.2. Optical properties

Due to the existence of such diversity of synthesis routes, it is possible to find in the literature numerous works reporting the synthesis of Ag_2S NPs with different optical properties. In order to establish a correlation between particle size and emission properties it is represented in Figure 1.8a the central emission wavelength of Ag_2S NPs as a function of their size. Strong variations in the emission peak position are observed for Ag_2S NPs with sizes below ~4 nm. In contrast, Ag_2S NPs with sizes above 4 nm present emission peaks localized between 1050 and 1250 nm in most reports. The analysis of the published data shown here can be well-explained considering a Bohr exciton radius for Ag_2S close to 2 nm. The fluorescence of NPs smaller than 4 nm is, therefore, affected by strong quantum confinement effects that results in a blueshift of the emission for decreasing sizes. On the other hand, Ag_2S NPs with diameters larger than 4 nm behave as “bulk” units or in a weak quantum confinement regime and their fluorescence emission wavelength is purely given by the intrinsic bandgap of Ag_2S. It is worth mentioning, however, that the synthetic route seems to play a critical role in the optical properties of Ag_2S NPs. Ag_2S NPs produced by synthetic routes based on the decomposition of metallic salts in organic media (normally in the presence of 1-dodecanethiol) show emission bands in the NIR-II range (1000–1500 nm), even if their size is lower than 4 nm. In contrast, most of the synthesis routes carried out in polar media (water, ethylene glycol) yield Ag_2S NPs with blue shifted emission bands (500–1300 nm) and higher PL tunability. This is exemplified in the selected

examples shown in Figure 1.8b, where blue and red lines correspond to syntheses carried out in polar and organic media, respectively. The dots, squares and triangles embedded in each of the lines correspond to the central emission wavelengths of different NP sizes depending on their synthesis method. These results underline the need of profuse synthetic and morphological studies to understand the disparity in the final optical properties depending on the synthesis route. The potential presence of complexes or polymers with distinct photoluminescence properties and the crystallography and/or presence of lattice defects in the final inorganic NP should be evaluated.

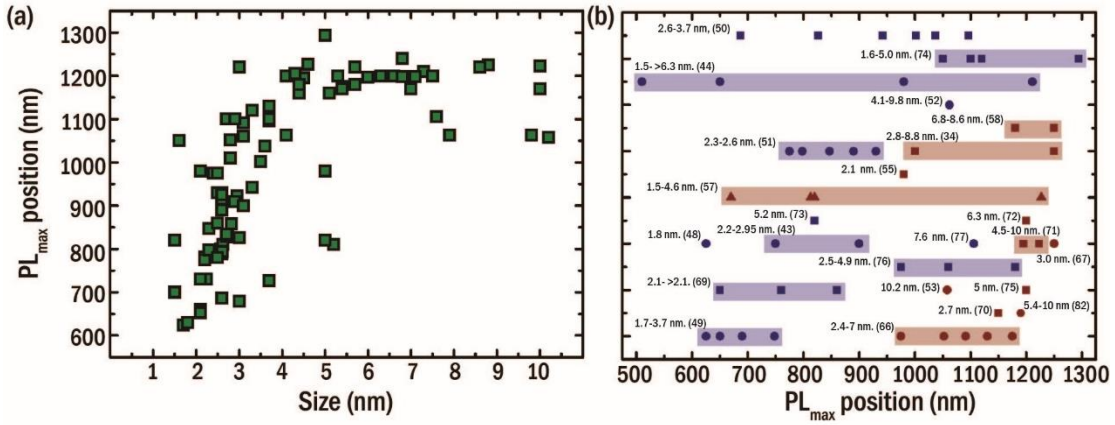

Figure 1.8. a) Comparison of the PL maxima of Ag_2S NPs with their size as reported in references [43, 44, 46, 48-50, 52-55, 57, 66-82] b) Spectral position of the PL maximum depending on the synthetic approach (■ -for hot injection, ●- for heat-up and ▲- for seeded growth) and the polarity of the media (organic in red and polar in blue). The NP size range for each synthesis is specified next to the line, along with the corresponding reference.

1.5. Applications

Taking advantage of all the attractive properties of this kind of NPs several applications have been found for them. So far, Ag_2S NPs have been successfully used in bioimaging and selective targeting, as therapeutic agents and for luminescence thermometry.

1.5.1. Bioimaging and selective targeting

The acquisition of images using NIR probes has grown in the last years due to several factors: it's a non-invasive technique, the minimized optical extinction from body tissues and the high resolution obtained (as high as 10 μm with Ag_2S).[83] Different *in vitro* assays using different cells lines were carried out as the first hydrophilic Ag_2S NPs were synthesized and now it is use for a wide range of fields of interest in biology and biomedicine. These NPs have been used for some interesting assays like as a probe to follow the fate of transplanted mesenchymal stem cells.[84] In this assay, the NPs were inserted inside the cells allowing for the observation of the

therapeutic effect of the stem cell in liver failure without affecting their DNA or causing apoptosis. In another experiment, these NPs effectively allowed the observation of the angiogenesis in a small tumor (the formation of new vessel from which the tumor obtains blood) thanks to the high resolution provided from their NIR PL.[85] Furthermore, this material does not only provide fluorescence-based imaging but it is also a potential probe in photoacoustic imaging (PA).[52, 86] In this case, the image is obtained through the lattice vibrations after laser irradiation. Thanks to this imaging technique and the response of the NPs, Wu and co-workers[86] observed how the NPs deposited in an atherosclerotic plaque due to the hydrophobic interaction with a surface ligand thus targeting that area of the mouse body.

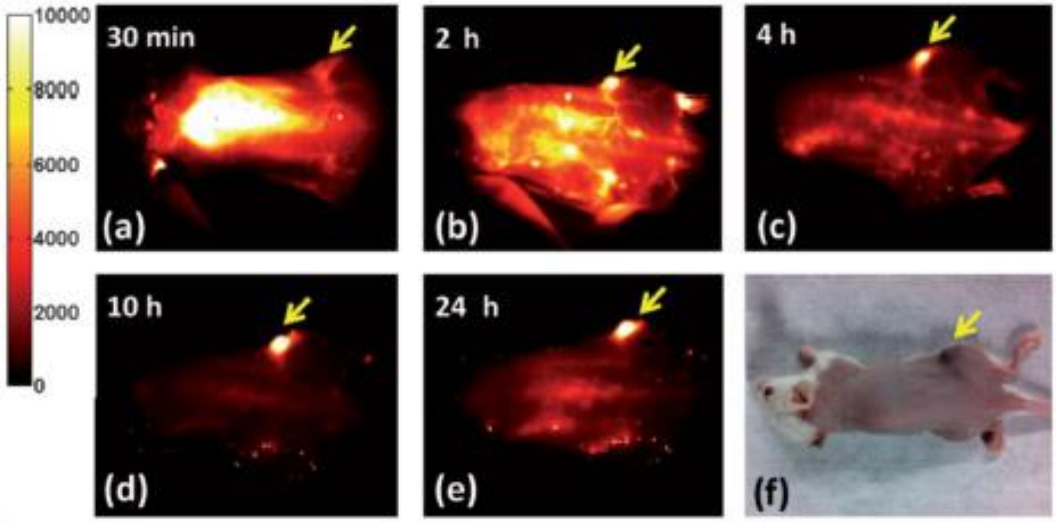

Figure 1.9. Intravenous injection of Ag_2S and their biodistribution during 24h. It can be observed that thanks to their surface coating the NPs end up in the region where the tumor is located. Reproduced with permission from reference [62]

1.5.2. Therapeutic agents

Different strategies are being developed to take advantage of the small size of NPs to turn them into therapeutic agents in different medical conditions. In the case of Ag_2S, the main fields in which these NPs are being used are in photothermal therapies (PTT), as well as a drug delivery unit.[87] For example, Yang et al[52] were able to fully eliminate a tumor using PTT at an Ag_2S concentration of 50 μg/kg. At that concentration, no damage was observed in any other organ, eliminating the NPs through renal clearance. Other studies show the use of this Ag_2S NPs, like the one by Cheng et al,[88] in which the NPs were introduced along with DOX in phospholipidic micelles. When the NPs arrived at the tumor thanks to the use and the high

penetration of NIR light the drug was released killing the tumor cells. This is an efficient way to avoid the secondary effect of these drugs since they are only released where the laser light is applied. It is worth noting also the study by Cheng et al, which reported how the irradiation of the Ag_2S catalyzes the appearance of ROS species like $^1O_2$ causing local cell death. These authors went one step further and by the conjugation of polydopamine to the NPs they achieved higher rates of $^1O_2$ showing the potential role of these NPs as photosensitizers in some therapeutic applications.[89]

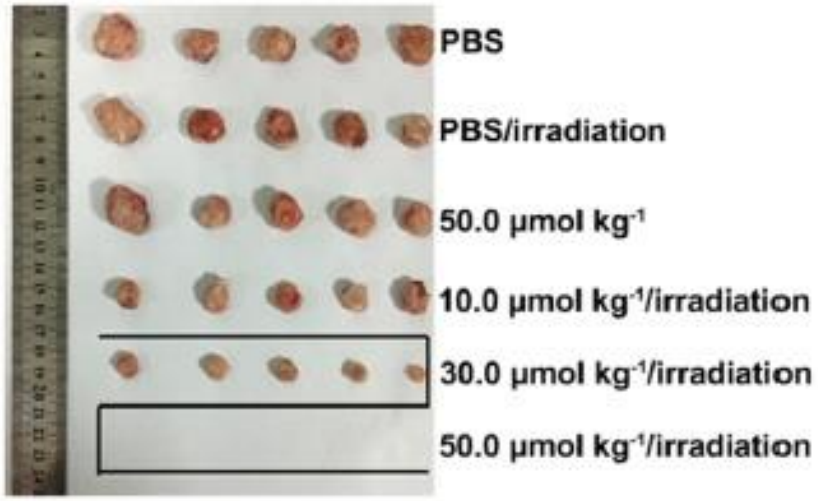

Figure 1.10. Effectiveness of PTT treatment in a tumor depending on the concentration of Ag_2S NPs injected. Reproduced with permission from reference [52]

1.5.3. Luminescence thermometry in the biological context.

Luminescence nanothermometry is an emergent application of luminescent NPs. The change in the different properties of the light emitted by the NPs carries information about intrinsic properties of the material and also its environment. The limitations of contact-based temperature readings at the sub-micron scale make these methods unable to address issues like intracellular temperature fluctuations, temperature mapping of microcircuits and microfluids.[90] Luminescence thermometry is a useful technique in biology due to the connection between a local temperature rise and some diseases. The presence of tumors of some articulation diseases provoke inflammation in the surrounding tissues, causing a temperature raise compared to their environment.[91] The presence of surface or close to surface injuries can be studies directly using thermographic cameras. However, if the region of interest lies deep inside the body, a different technique must be developed. Different kinds of NPs have been used in recent years that are able to measure temperature in deep regions like CdSe/CdS QDs, PbS/CdS/ZnS QDs and lanthanide ions-containing nanostructures.[90] The main

problems that QDs are facing in this application are, first, their chemical composition based on Cd and Pb that are toxic to living organisms. Secondly, the thermal sensitivity of these structures is not high enough, thus making it difficult to monitor small temperature changes that are of interest. Lanthanides like Nd^{3+}, Yb^{3+} or Er^{3+} have been as well promising thermometric probes due to their high number of emitting states that are strongly dependent on thermal energy. However, these systems have also some drawbacks like the self-absorption of their emitted energy (blurring the intensity response) and their optical power-dependent spectra.[92]

The quality of luminescence thermometer is measured through their thermal sensitivity, which is defined as:

$$S(T) = \frac{1}{P} \cdot \frac{P}{dT} \quad (1.3)$$

Where P is the parameter used for the thermal sensing. The higher the sensitivity the litter changes will the thermometer be able to distinguish. In order to facilitate thermal reading, it is preferable that the sensibility is linear with temperature. Otherwise, the analysis would become complex and the measurement uncertainty would be enhanced. In general, there are several approaches to measure temperature using the photoluminescence from NPs.[93]

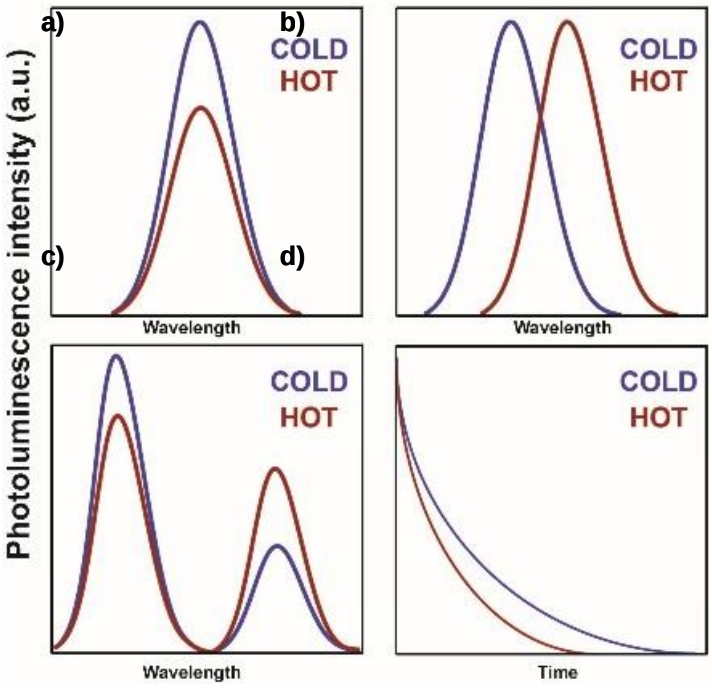

Figure 1.11. Different strategies for the temperature measurement through the PL of NPs

1.5.3.1. Intensity-based thermometry

In this approach, the decrease in the emitted intensity is correlated to the increasing temperature. This is produced due to the activation of phonon assisted processes that attract the charge carriers to non-radiative deexcitation pathways. In order to obtain a constant sensitivity in all the working temperature range it is desirable that the decrease in PL with T follows a linear trend.

1.5.3.2. Spectral position thermometry

In this case, the temperature raise causes the shift of the spectral position of the PL maximum. This feature is mainly determined by the energy difference between the valence and conduction band of the nanostructure and it is strongly temperature dependent due to the inner properties of the material.

1.5.3.3. Band-shape or ratiometric thermometry

In this approach, the temperature reading is based on a luminescent probe that has multiple emission bands whose PL intensity strongly varies with temperature. Thus, one emission can be considered as reference while the other varies. These bands may come from the same structure (e.g. Mn^{2+} doped QDs) or from two different emitting centers (e. g. In hybrid nanostructures containing two different kind of photoluminescent NPs). The ratio between the intensity of the two peaks can then be calibrated with temperature obtaining an intensity-independent temperature reading free from random noise.

1.5.3.4. Lifetime thermometry

The photoluminescence lifetime (τ) is defined as the time at which the PL intensity decays down to 1/e of its initial value. This parameter is inversely proportional to the probability of the transition. Due to different temperature related processes like energy transfer processes or phonon assisted non-radiative decays, τ is strongly dependent on temperature, allowing for its use as a measurement tool.

Objectives of this thesis

1. The synthesis and detailed optical, and morphological characterization of Ag_2S-based NPs including passivated and core-shell structures, and their evaluation as possible candidates for luminescence thermometry assays in the spectral region NIR-II , from 1000 to 1400 nm.

2. The preparation of optimized hybrid systems combining Ag_2S-based and iron oxide NPs to be used as biological markers, nanothermomethers, and heaters, simultaneously. These combined capabilities are required for controlled iron-oxide-NPs-based hyperthermia therapies.

Chapter 2: Synthesis and evaluation of Ag_2S as luminescence thermometers

2.1. Introduction

Temperature sensing in biological media has become essential in the development of diagnostics and therapeutic strategies.[91, 94-97] Among the different approaches for thermal control, luminescence thermometry is rapidly spreading. The main limitations of this approach include: (i) the reading of temperature-induced changes in the luminescence intensity from single emission lines and (ii) the short penetration depths of luminescent nanothermometers operating in the visible range[98, 99] for *in vivo* applications, along with autofluorescence background signals.[100] As mentioned in the introductory chapter, the former can be overcome by the use of ratiometric-based luminescent nanothermometers (hereafter RLNThs) in which the readout is extracted from the ratio between their photoluminescence intensity at different wavelengths, and the later requires the use of NPs working in the near-infrared range, in particular in the second biological window, expanding from 1000-1400 nm. Some examples of RLNThs working in the NIR-II include rare earth doped and co-doped NPs (RE-NPs) or the combination, in a single structure, of both RE-NPs and QDs.[101-104] In the case of RE-NPs, their thermal sensitivity is lower than 0.5%·°C^{-1} and the reduced absorption cross sections per NP leads to low signal-to-noise ratios during in vivo experiments. The combination of these two factors results in thermal uncertainties typically above 1 °C. On the other hand, hybrid nanostructures containing RE-NPs and QDs provide good thermal sensitivities (>2 %·°C^{-1}) but at the expense of relatively large sizes (>100 nm) that could limit their application in certain in vivo experiments.[102] As mentioned in the Introduction, high sensitivity and high penetration in vivo temperature sensing requires the design and development of alternative nanomaterials.

Ag_2S NPs have been identified as suitable materials with reported low cytotoxicity and excellent heating properties upon optical excitation, which has already triggered their application for several *in vivo* experiments. Despite its potential interest for biological applications, the use of Ag_2S NPs for thermal sensing has vaguely been explored,[48] and never as RLNThs in the NIR-II. In this Chapter, a profuse morphological and structural study of the NPs has been carried out by advanced microscopy techniques. Additionally, their optical absorption has been studied by means of transient absorption spectroscopy (TAS), and the factors that affect their emission response are also discussed. Their potential use as RLNThs operating in the NIR-II based on both temperature-induced spectral shifting and PL intensity quenching is

evaluated. Proofs of concept of the suitability of these NPs as subtissue temperature sensors are given by a simple *ex vivo* experiment. Furthermore, the as-synthesized NPs are subjected to a ligand exchange step in order to obtain water-dispersible hydrophilic NPs. This ligand step affects especially the surface of the NPs, where these ligands interact with the NPs. The possible appearance of surface states or defects was studied using time resolved optical techniques to evaluate the quality of the hydrophilic NPs. The potential for *in vivo* temperature measurement of the hydrophilic NPs is finally tested in an *in vivo* cooling experiment where the NPs were injected in the prefrontal cortex of a mouse to monitor the physiological reaction in the event of severe body hypothermia.

2.2. Results and discussion

2.2.1. Synthesis and morphological, chemical and optical characterization

The NPs described in this Chapter were synthesized by a thermal decomposition route described on Section 2.2 of APPENDIX I. Similar routes have been used in the synthesis of Ag_2S NPs,[62] yielding samples of an average size between 4-5 nm with a good size dispersity (≅±1nm). These samples, however, are composed of two easily differentiated parts: individual, well-dispersed and stable NPs in solution (supernatant), and aggregates forming part of a precipitate with sizes between 100 nm-5 μm, as shown in Figure 2.1a-b. The absorption and emission spectra of these samples are depicted in Figure 1c. It can be seen how no excitonic features appear in the steady-state absorption spectrum that hinders the determination of the optical bandgap of the NPs. The NPs show a bright PL centered in 1200-1250 nm, right in the NIR-II.

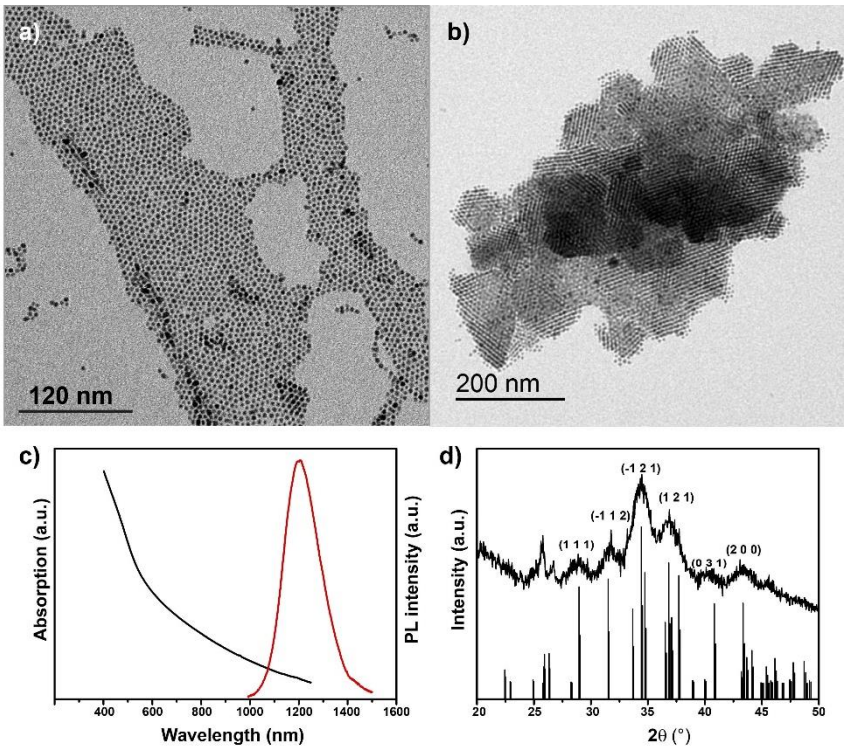

Figure 2.1. a-b) TEM images of the NPs obtained in this synthetic approach, supernatant and sediment, respectively. c) Optical absorption and room temperature PL of the NPs d) XRD diffractogram of the as-synthesized NPs

The XRD diffractogram in Figure 2.1.d shows the presence of plane distances that can be assigned to the low temperature phase (α-Ag_2S, acanthite). In order to obtain more information about the crystalline and chemical composition of these NPs, HREM inspections were carried out. Individual Ag_2S NPs show good stability under the electron beam of a TEM working at 100 kV of acceleration voltage; however, the aggregates are clearly affected by the beam, as it is evidenced in Figure 2.2, where the time evolution of an aggregate under the beam evidences blurring of the NPs and the appearance of dark spots.

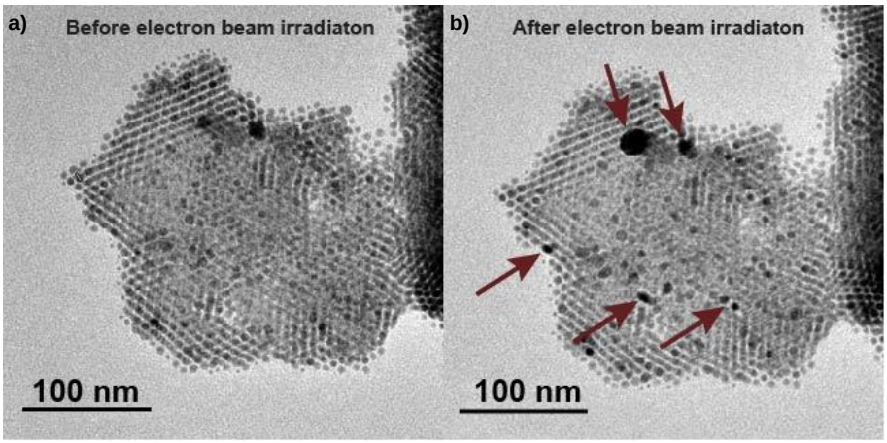

Figure 2.2. TEM image of an arrangement of NPs a) Before exposure to a current density of 100 $\mu A/cm^2$ and b) After 1 min of exposure

This effect has not been reported for these NPs but similar observations have been made for silver metal organic compounds as it will be discussed in Chapter 3. The high contrast of the structures growing from the NPs' aggregates in comparison with the Ag_2S NPs points out that the possible chemical nature may be of Ag^0 that is reduced due to the electron beam and the high reduction potential of Ag^+ ($E° (Ag^+|Ag) = 0.799$ V).

To gain further insights about the NPs, different HRTEM techniques were used in collaboration with Miguel López-Haro and Ana B. Hungría at the University of Cádiz. Further HRTEM inspections showed that the supernatant NPs were not stable under the beam at the acceleration voltage of 200-300 kV, requiring an aberration corrected TEM operating at 80 kV to minimize the electron beam damage and Ag^+ migration. Figure 2.3 shows Scanning Transmission (STEM, Figure 2.3a) and high resolution (HRTEM, Figure 2.3b) images of the as-synthesized Ag_2S NPs. The structural analyses of HRTEM images, using Digital Diffraction Patterns (DDP) show a silver multi-twinned core. The small size of the shell (ca. 1 nm) hampers the high-resolution observation in that area. NPs have an average size of 4.3±1.5 nm although a second population of larger Ag_2S NPs is also observed (not shown). The X-ray Energy Dispersive Spectroscopy (EDS) mapping images shown in Figure 2.3c-f reveal the presence of an Ag rich core (80% Ag, 20% S) surrounded by an Ag_2S stoichiometric shell. The presence of this structure may result from the low reduction potential of the Ag^+ ions and the presence of thiols that can act as reducing agents and ligands.[105] This is further observed in Figure 2.3g-h where the x-ray intensity profile proves the excess silver in the core while the stoichiometric composition is found only on the edges of the NP.

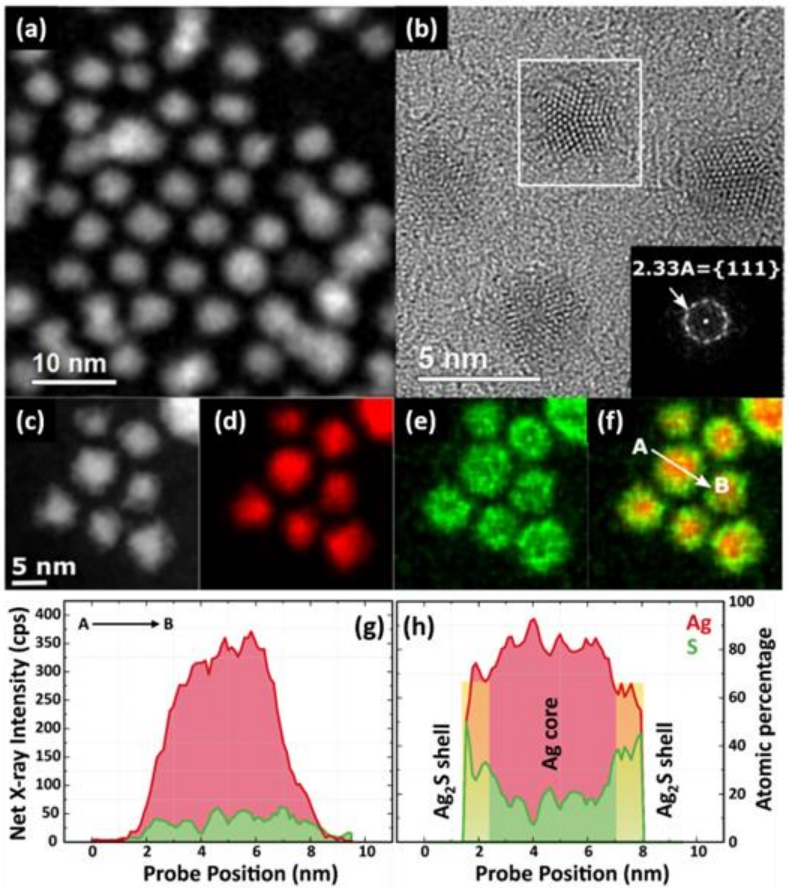

Figure 2.3. (a) HAADF-STEM of Ag/Ag_2S NPs recorded at medium magnification. (b) Monochromated HREM images of Ag_2S NPs showing a Ag multi-twinned core (inset a DDP performed on the marked white square). (d-f) EDS elemental mapping showing the spatial distribution of (d) Ag (red), (e) S (green) and (f) Ag+S of the set of NPs shown in (c). The EDS maps are deconvoluted and smoothed to improve the visualization. (g) Net X-ray intensity profiles extracted from the white arrow marked in image (f) together with atomic quantification of the intensity profile (h). Note how the Ag/S ratio corresponds to Ag_2S in the shell region (marked in yellow). High resolution images and EDS quantitative information

As discussed in Chapter 1, the optical properties of these NPs are still controversial. There are reports including unusual absorption and emission spectra. In one of these reports, it is discussed that the formation of defects in the internal structure of the NPs leads to different energy levels that generates three emission peaks.[106] We have also observed this three-peak emission and, contrarily, we correlate it to the absorption of the NPs' dispersant. Figure 2.4 shows the PL spectra of the Ag_2S NPs dispersed in TCE (Figure 2.4a) and toluene (Figure 2.4b). Figure 2.4a also includes the NIR absorption of toluene between 1000-1500 nm as well. Indeed, the emission spectrum obtained when Ag_2S NPs are dispersed in toluene experiences a strong modulation that results in the appearance of three pseudo-peaks at 1142, 1189 and 1236 nm. Both spectra correspond to the same NPs firstly measured in tetrachloroethylene and then transferred into toluene after washing and drying.

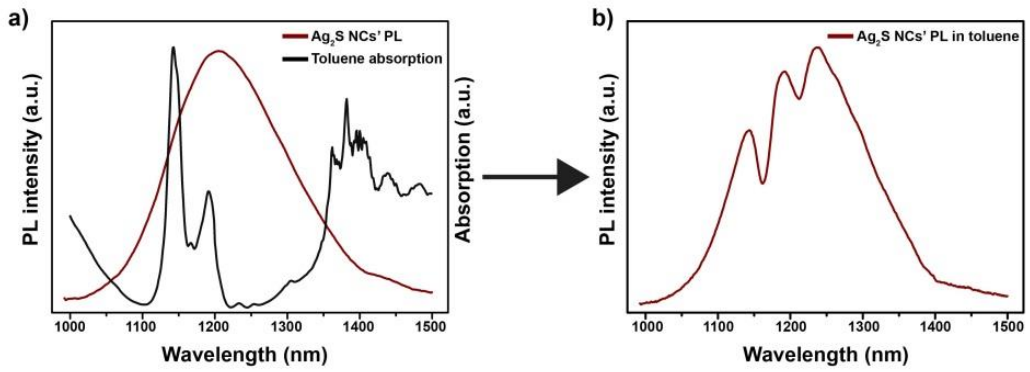

Figure 2.4. Influence on the NPs' dispersant on their NIR emission

The fact that these peaks disappear when the solvent is changed points out that the line shape is not related to intrinsic defects but to radiative re-absorption of the Ag_2S NPs emission by the solvent molecules. Such spectral modulation has been found to be especially evident when the Ag_2S NPs are suspended in solvents with C-H bonds. C-H bonds-containing groups show strong absorption lines in the 1000-1400 nm range due to highly efficient vibrational overtones absorptions, which results in the modulation of the Ag_2S emission spectrum.

Some nanostructures (for example QDs) present discrete energy levels as a consequence of the quantum confinement of the photo-carriers, which are evidenced by sharp resonances in steady-state absorption spectra. In contrast, as it is observed in Figure 2.1c, the absorption spectrum of the here synthesized Ag_2S NPs in solution is characterized by a long featureless tail and absence of any resonance. This absence of sharp resonances has been discussed in the literature,[66, 79] although its origin is still not clear. It is however accepted that the main reason may be the high exciton binding energy for Ag_2S (100 meV)[79] that implies a small exciton radius. This would imply that the NPs presented here are too big to be inside the strong quantum confinement regime, thus presenting bulk-like optical behavior.

In order to determine the optical band gap of the as-synthesized NPs, Transient Absorption Spectroscopy (TAS) measurements were carried out. By means of ultrashort laser pulses, this technique allows for the study of the absorption dynamics at the femtosecond scale.

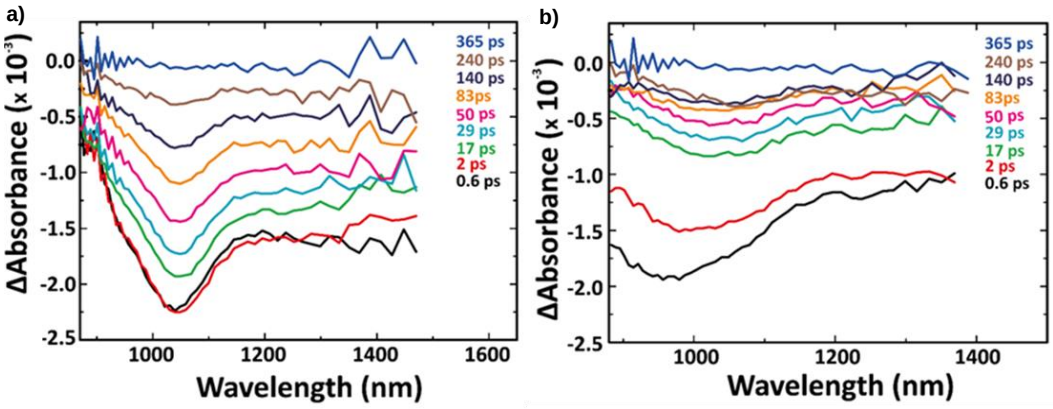

Figure 2.5. Transient absorption spectroscopy of the as-synthesized NPs at different delay times from the excitation pulse in a) Colloidal dispersion and b) Deposited on a transparent substrate

The use of this technique on a colloidal dispersion of the NPs (Figure 2.5.a) reveals a strong negative band at 1050 nm (1.18 eV) attributed to the photobleaching of transitions from the valence to the edge of the conduction band, in fairly good agreement with the bandgap of bulk Ag_2S. A broad negative TA signal extends towards lower energies being likely caused by a combination of pump-induced scattering changes and stimulated emission. Similarly, the spectrum of the NPs deposited onto a transparent quartz substrate (Figure 2.5.b) shows the broadening of the resonance due to electronic coupling which is promoted when the NPs are deposited. It is also observed that, in the film, the resonance shifts with time towards the red until 3.7 ps. This effect can be related to the state filling of the upper energy levels and the presence of some accessible levels below the conduction band maximum. The fact that this effect is more pronounced when the NPs are deposited may be due to some electronic coupling that generates these levels below the conduction band maximum, as a slight red shift of the transition is also observed.

In order to characterize the quality of our semiconductor NC, we studied the PLQY. Despite it is one of the most important semiconductor NC quality indicators, as described in the Introduction, the measurement of PLQY in the NIR region is challenging due to the lesser sensitivity of the infrared detectors compared to the visible range ones, and due to the instability of the NIR emitting dyes like those commonly used (IR-125 and IR-26) which are easily degraded by oxygen, humidity, and light making the recording of reproducible measurements an exhausting task. The absolute PLQY of all the samples synthesized in this work was measured using an integrating sphere, in collaboration with Dr. José Marqués Hueso

from the Heriot-Watt University of Edinburg. This method has the advantage of measuring directly the amount of absorbed and emitted photons by the whole sample, which results in more accurate values than other methods such as dynamics measurements because it considers physical limitations like reabsorption. The PLQY of IR-26, which is employed as standard, has been recently reviewed after accurate measurements with an integrating sphere.[107, 108] Details of the procedure are described in Section 2.4.4. of APPENDIX I. The PLQY of the here studied samples was found to be 2.5% in tetrachloroethylene (TCE).

Technique	Solvent	PLQY (%)	Ref
Integrating sphere	Tetrachloroethylene	2.5	This work
IR-26	Hexane	15	[109]

Table 1. PLQY of the Ag_2S NPs depending on the measurement technique

As a comparison, in the case of the NPs synthesized following the same route, the PLQY reported in the literature in hexane is 15% when measured using the dye IR-26.[109] In our case, measured with the integrating similar samples gave a QY in tetrachloroethylene (TCE) of 2.5%, which is around 5 times less than the one obtained using the dye, making it difficult to compare the yield from these two different methods. As previously stated, the value obtained by means of the direct comparison with IR-26 is likely an overestimation caused by the instability of the standard dye. While higher values are desirable, our work show that these PLQY values are enough to perform optical studies *in vivo*,[110] as will be further briefly explained. Different approaches can be followed to increase the PLQY of semiconductor NPs like the elimination of surface defects, the preparation of CS structures or other post-synthetic treatments.

2.2.2. Luminescence thermometry

The potential use of this kind of NPs for luminescence thermometry was ascertained by a series of experiments detailed in Figure 2.6. The detailed experimental set-up is described in Section 2.5.1. of APPENDIX I. The thermometric characterization was carried out in collaboration with Dra. Blanca del Rosal from the Fluorescence Imaging Group led by Dr. Daniel Jaque(Universidad Autónoma de Madrid). The thermometric characterization was carried out using a spin coated dispersion of the NPs embedded in a flexible polymeric thin film (TF). A characteristic Ag_2S TF is shown in Figure 2.6a, in which the dark color due to visible absorption

of Ag_2S NPs can be clearly observed. The Ag_2S TF showed a strong luminescence in the 1000-1400 nm range under 800 nm laser excitation, as it is evidenced in the fluorescence image included in Figure 2.6b. The emission spectrum of an Ag_2S TF is included in Figure 2.6c as obtained at different temperatures ranging from 15 up to 50 °C.

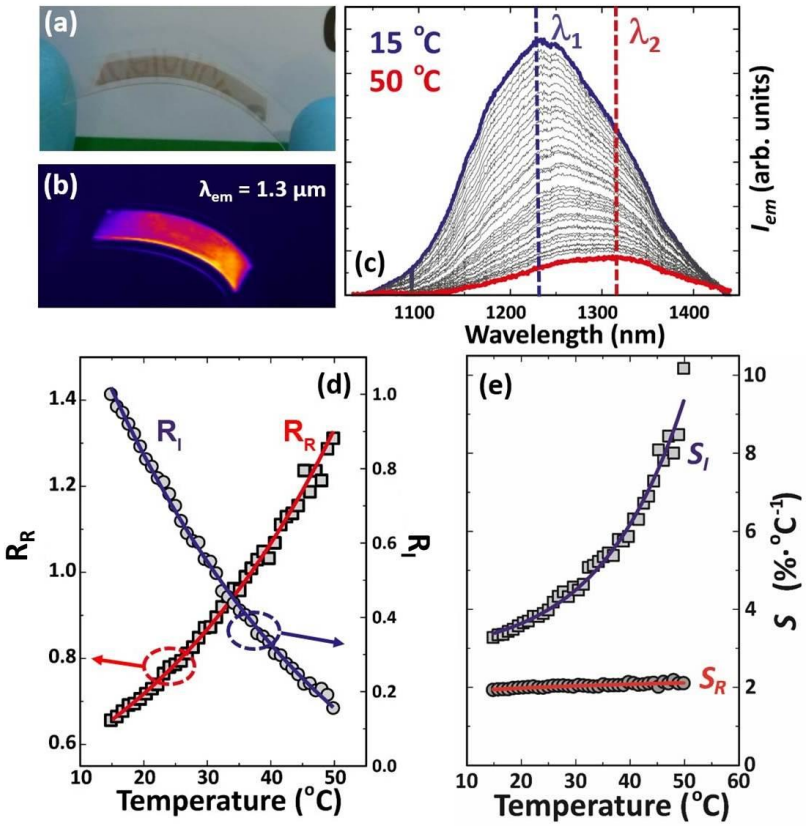

Figure 2.6. Optical properties and sensitivity of Ag_2S TF. (a) Optical and (b) infrared fluorescence images of a flexible Ag_2S NPs TF. The infrared fluorescence image was obtained by using an 800 nm laser for excitation and collecting the infrared luminescence at 1.3 µm. (c) Emission spectra of the TF from 15 up to 50 °C. (d) Temperature evolution of the integrated emitted intensity (I_{em}) and the ratio R_R as calculated from emission spectra included in (c). (e) Temperature variation of the thermal sensitivities S_I and S_R as obtained from the analysis of data included in (d). Dots are experimental data and solid lines are guides for the eye.

As it can be observed, there are two well-observable effects: a strong luminescence quenching and a remarkable temperature-induced redshift of the maximum PL wavelength. The former is related to the temperature activation of phonon related processes that lowers the possibility of radiative recombination.

The temperature-induced redshift is observed from the emission wavelength centered at $\lambda_1 \approx 1205$ at 15°C to $\lambda_2 \approx 1298$ nm at 50 ºC. The wavelength increases linearly with temperature at a rate of 2 nm·°C^{-1}, which corresponds to a temperature-induced energy shift of 1.7 meV·°C^{-1}. The change in the PL energy is in good accordance with the value reported for the change in the band gap energy of bulk Ag_2S.[111]

$$E_g\,(T) = E_0(0) - \frac{\alpha T^2}{T+\beta}\ (2.1)$$

The fact that the temperature dependence of the Ag_2S NPs can be approximated without taking into account terms affecting NPs exhibiting quantum confinement confirms that NPs of sizes around ~4 nm (as evidenced by TEM) are out of that regime. This result opens the possibility of not only using these NPs for the intensity-based temperature reading approach but also using the energy change which is less dependent on the environment. It is also noticed in Fig. 2.6c that the emission peak is broadened at high temperatures due to the energy loss by photons in the temperature activated phonon processes.

As explained in the Introduction, (equation 1.2), the quality of a luminescence thermometer is measured through their thermal sensitivity, (S), which is defined as the evolution of a temperature dependent parameter, P. For the results shown in Figure 2.6 c, P can be defined as $\mathrm{R_I}$, the normalized intensity as the result from dividing the integrated emitted intensity at a certain temperature by the intensity at a reference temperature $(\mathrm{T} = 15°\mathrm{C})$. The integrated emission intensity, R_I, (Figure 2.6d, data in blue) is reduced by almost 80% when the temperature is increased by only 35 °C. Thus, this quenching makes possible temperature reading from the evaluation of $\mathrm{R_I} = \frac{\mathrm{I_{em}^{int}(T)}}{\mathrm{I_{em}^{int}(T_0)}}$. The thermal sensitivity achievable from the experimental determination of the intensity ratio, $\mathrm{S_I}\,(\mathrm{T})$, is thus given by:

$$\mathrm{S_I(T)} = \frac{1}{\mathrm{R_I}}\,\frac{\mathrm{dR_I}}{\mathrm{dT}}\ (2.2)$$

The variation of $\mathrm{S_I}\,(\mathrm{T})$, with temperature is included in Figure 2.6e (data in blue). At room temperature, $\mathrm{S_I}$ has been found to be as high as 3%·°C^{-1}, which is almost three times larger than the intensity-based sensitivity recently provided by infrared emitting PbS/CdS/ZnS QDs successfully used for temperature feedback during *in vivo* photothermal therapy.[22]

Furthermore, the PL response of the NPs' PL allows for the ratiometric determination of temperature. For thermal sensing purposes we can now define P as the intensity ratio $R_R = \frac{I_{em}(\lambda_2)}{I_{em}(\lambda_1)}$ as the quotient of the emitted intensities at 1311 nm (λ_1) and 1235 nm (λ_2) (see Figure 2.6.d, data in red). Similar to R_I (T), R_R increases with temperature and the thermal sensitivity is given by:

$$S_R(T) = \frac{1}{R_R}\,\frac{dR_R}{dT}\ \ (2.3)$$

Figure 2.6e (data in red) shows that the ratiometric thermal sensitivity S_R is almost temperature independent and close to 2 %·°C^{-1}. This value is compared in Figure 2.7. to the thermal sensitivities reported in literature for other luminescence thermal sensors based on NPs.

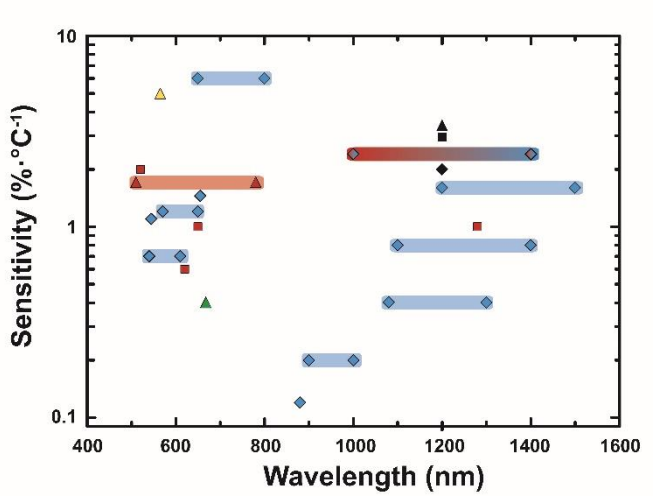

Figure 2.7. Thermal sensitivities reported in the literature for other luminescence thermal sensors in the first (BW-I) and second (BW-II) biological window. The color legend depicts yellow as polymers, green as metallic clusters red as semiconductor, black as Ag_2S and blue as rare-earth doped NPs. The shape stas for: triangle- lifetime based thermometry, square- intensity based, diamonds- intensirty ratio. Mixed colors are heterostructures based on two types of NPs

The ratiometric thermal sensitivity of the as-synthesized Ag_2S NPs is comparable to the highest thermal sensitivities reported for the widely used erbium-based RLNThs, with the advantage of operating in the NIR-II, a requisite for subtissue thermal sensing. Furthermore, when comparing with other RLNThs also operating in the NIR-II, it is found that the here reported Ag_2S NPs provide thermal sensitivities several times higher than those of RE-NP systems such as Nd:LaF_3 NPs or Nd:Yb core/shell nanostructures (both having thermal sensitivities below 1%·°C^{-1}, Figure 2.7). In addition, the thermal sensitivity of our Ag_2S NPs is close to that of hybrid nanostructures based on the polymeric encapsulation of PbS/CdS QDs and neodymium-doped NPs.[102] As mentioned in Chapter 1, the intensity-based approach in luminescent thermometry is the most used due to its simplicity but sometimes it is not the most reliable due to the possibility of external factors that may produce an intensity change that is not related with temperature, such as diffusion.

2.2.3. Subtissue thermometry

In order to evaluate the ability of these NPs to perform ratiometric LNTh studies in biological environments a simple ex vivo experiment was designed (Figure 2.8). A solution containing

Ag_2S NPs was injected 1 and 4 mm deep into a dead tissue sample followed by the application of heat pulses of different time lengths. Figure 2.8b shows the change in the spectral position of the PL after the application of a heat pulse. The temperature increase is calculated on the basis of the change in the ratio of emitted intensity at two different wavelengths, as explained above.

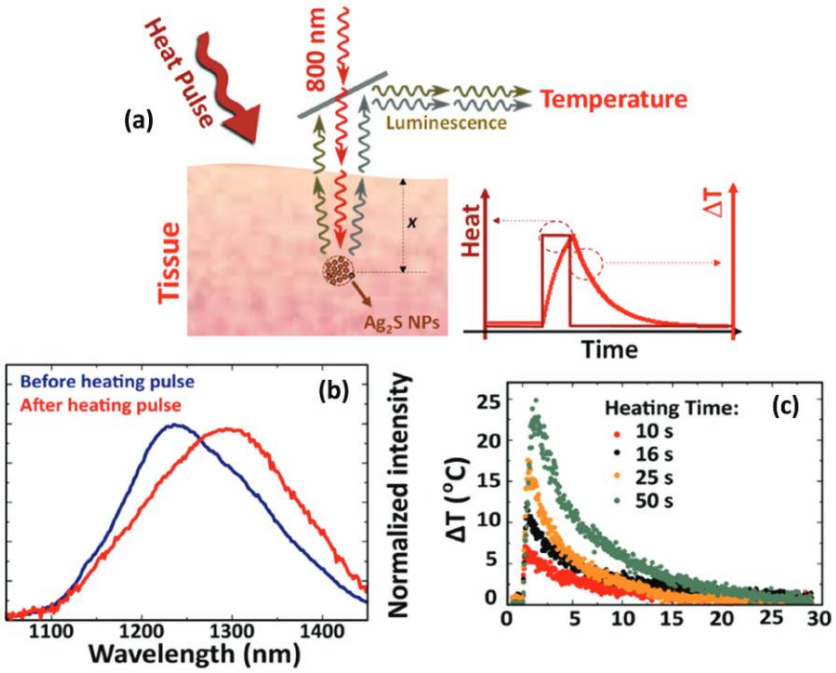

Figure 2.8. Subtissue thermal measurements of colloidal dispersions. (a) Schematic representation of the experimental procedure designed for the evaluation of colloidal Ag_2S NPs as subtissue thermal sensors **(b)** Subtissue emission spectra obtained from a 1 mm deep injection of Ag_2S NPs as obtained before and after the application of a 50 s long heating pulse. **(c)** Time evolution of the subtissue temperature increment at a depth of 1 mm as obtained for different durations of heating pulses.

In particular, the intensity ratio between emitted intensities at 1235 and 1311 nm, previously defined as R_R suffered a reduction close to 40 %, revealing a temperature increment at the injection site close to 20 °C.

The experimental arrangement schematically drawn in Figure 2.8a does not only allow for a quantification of the subtissue temperature increment (ΔT_{stiss}) but also to monitor its time evolution ($\Delta T_{stiss}(t)$). To do so, the emission spectrum generated by the injected NPs was measured every 2 s before, during, and after the heat pulse. The calculation and calibration of the intensity ratio leads to the time profile of the temperature at the injection site. Figure 2.8c shows the time evolution of ΔT_{stiss} at a depth of 1 mm as obtained for different durations of the heat pulse. In all cases, temperature is found to increase during the heating pulse, being the maximum temperature increment higher for longer heating pulses. This is clearly shown in Figure 2.8d, in which the maximum temperature increment (ΔT_{max}, obtained at the end of

heating pulse) is represented as a function of pulse duration. The maximum temperature increment is found to be, in a first order approximation, proportional to pulse duration, as could be expected since the total energy deposited in the tissue is proportional to the heating time. Therefore this experiment proves the ability of the NCs to perform intensity and spectral position based thermometric measurements with high sensitivity and to monitor in real time their evolution.

2.2.4. Preparation and optical study of water-dispersible NPs

In order to use the as-synthesized NPs in biological applications it is mandatory to replace the native hydrophobic ligands used for their synthesis for hydrophilic and biocompatible ones. To obtain individual water-dispersible Ag_2S NPs, a ligand exchange strategy was developed using a thiol-modified polyethylene glycol polymer (PEG-SH). Through rough sonication in the presence of a high excess of the polymer, the aggregates can be broken and the NPs transferred to a stable dispersion in aqueous media including phosphate buffers (PBS), necessary for biological studies (see details in Section 2.4 of APPENDIX I). This ligand exchange process is tedious, not very efficient, and causes a slight increase in the NPs size (see Figure 2.9a,b for TEM and size histogram prior to ligand exchange and Figure 2.9d,e for data after this process).

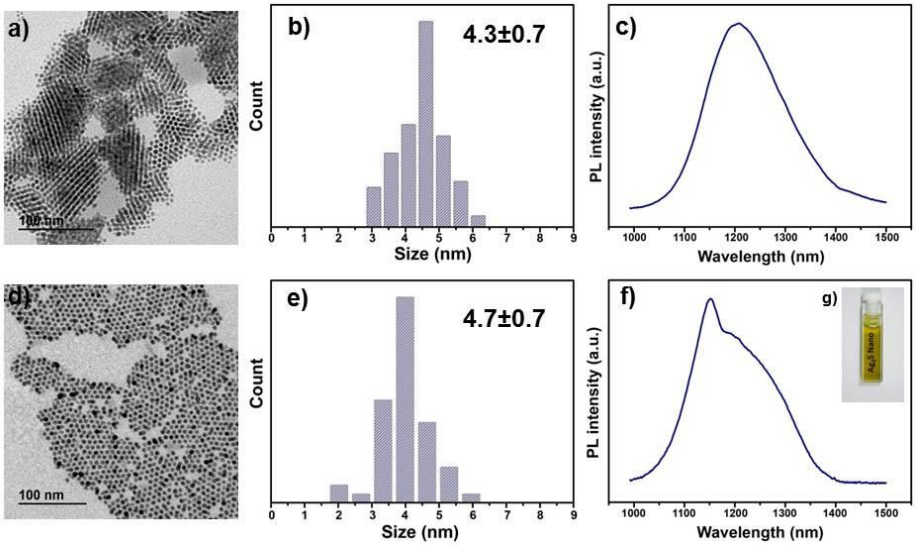

Figure 2.9. a-c) TEM and PL characterization of organic dispersible NPs and d-f) TEM and PL characterization of water dispersible NPs. A dilute water solution containing the Ag_2S NPs is shown in g).

As observed in Figure 2.9f, the as prepared water dispersible NPs retained the NIR PL inside the second biological window, necessary for optimal imaging and temperature sensing. The PL appears in Figure 2.9f deformed due to the absorption of water, contrary to pristine NPs that

can be dispersed in TCE to obtained PL spectra without solvent absorption features (Figure 2.9c). No polar solvent without absorptions bands in that wavelength interval has been found. After the ligand exchange process, the NPs preserve their high thermal sensitivity in intensity based thermometric measurements as observed in Figure 2.10. Consequently, these NPs can be used successfully as intensity-based LNThs in aqueous media. However, the spectral position approach is lost due to the absorption of water that blurs the peak maximum, making the ratiometric measurement not as reliable as it was before the ligand exchange.

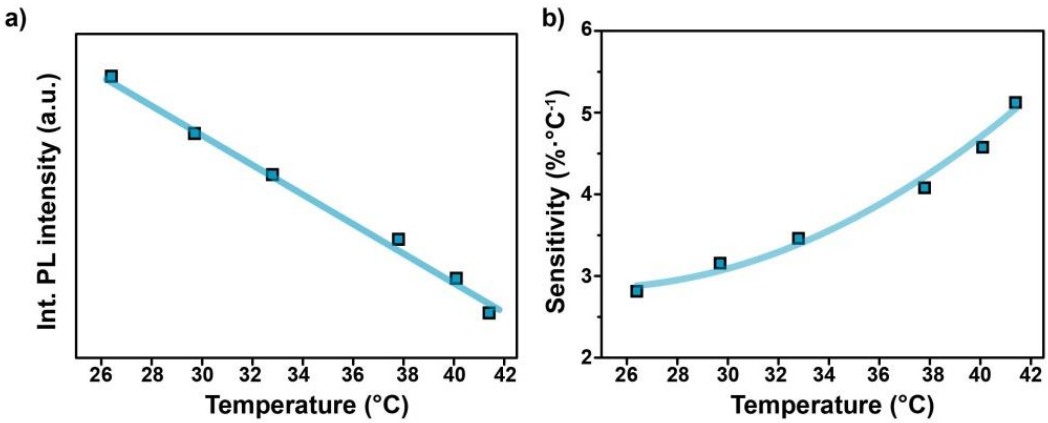

Figure 2.10. Intensity based luminescence thermometry measurements

The PL emission of water dispersible NPs is reported to be strongly dependent on the environment which could lead to intensity changes when the NPs find regions with different pH due to the own tissue or metabolic changes.[112] However, the as-synthesized NPs are capable of enduring pH change up to 1 unit with an intensity change of less than 1.2%. The PEG-SH coverage makes robust luminescent probes ready to be used in different biological media regardless its pH, as observed in Figure 2.11

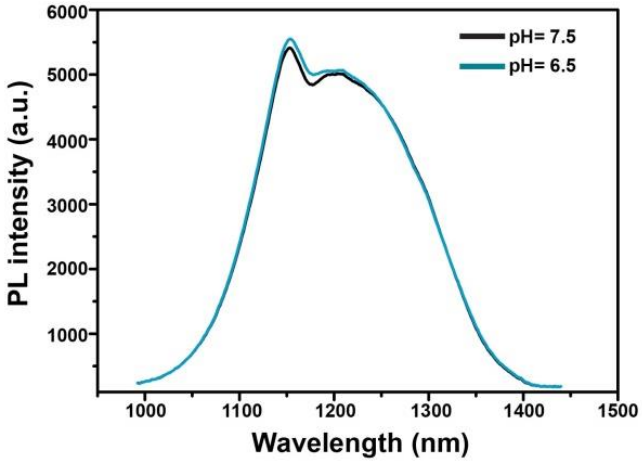

Figure 2.11. Intensity change due to the presence of acidic pH

As extensively reported for QDs, the ligand exchange process affects the surface of the NPs (where ligands are bound). As previously discussed, the surface of the NPs has a significant influence in their PL. The low coordination number of the surface atoms compared to the one of the bulk may lead to the formation of mid-gap states that ease non-radiative recombination pathways, hindering their optical properties (Figure 2.12).

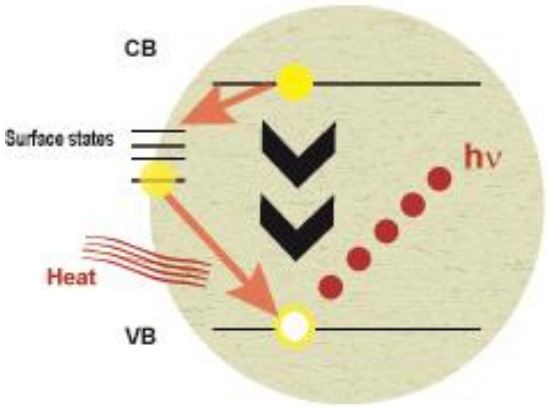

Figure 2.12. Scheme of the radiative and non-radiative dexcitation paths.

The ligand exchange process can be a source for the formation of this kind of surface defects, especially when it involves rough sonication. In order to study the effect of the ligand exchange process in the surface of the NPs, a time-resolved PL study was carried out as shown in Figure 2.14. These spectra were acquired by Harrisson Santos form the group of Dr. Carlos Jacinto in the University of Alagoas (Brazil).

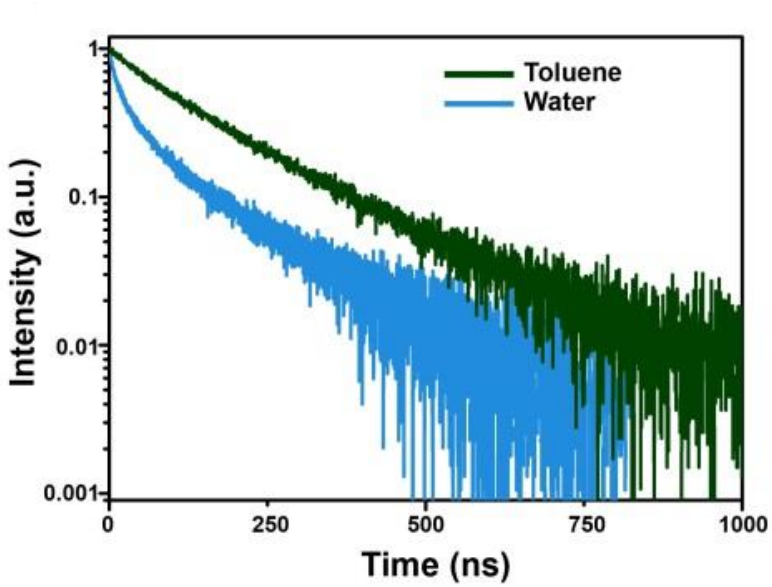

Figure 2.14. Room temperature luminescence decay curves of Ag_2S NPs in toluene and water.

Despite the colloidal solutions of Ag_2S NPs in water and toluene showed similar emission spectrum, their fluorescence decay at room temperature curves were found to be remarkably different, as it can be appreciated in Figure 2.14. The differences in the PL emission decay dynamics of these two samples could be attributed to different surface-related phenomena and not to a size effect, as in both cases the size of the NPs is well above that producing quantum confinement effects. Furthermore, no differences in their morphology are observed in the TEM images. On one side, hydrophobic Ag_2S NPs dispersed in toluene showed a single exponential decay.[113] According to previous works, this behavior suggests that in this case surface related nonradiative de-excitations (via surface defects or environment assisted multiphonon relaxations) are not a main deexcitation pathway for photoexcited electrons. Thus, the observed single exponential decay obtained for hydrophobic Ag_2S NPs dispersed in toluene reveals the single contribution of "bulk" radiative relaxations. This result is consisting with the dense surface-coating of the as-synthesized NPs whose surface is well isolated from oxygen and other reactive species that may degradate the NPs' surface. Under this assumption, we can state that the room temperature "intrinsic" bulk fluorescence lifetime of the hydrophobic Ag_2S NPs is close to $\tau_B \approx 180$ ns. Differently from the hydrophobic NPs, the PEG-SH coated hydrophilic Ag_2S NPs dispersed in water showed an evident nonexponential decay. Fitting the decay curve obtained at room temperature a fast and a slow decay times of τ_S^{PEG}=17 ns and τ_B^{PEG} =140 ns, respectively are obtained. The differences between fluorescence decay curves of Ag_2S NPs in toluene and water can be unequivocally attributed to surface-related processes. These values can be compared with those previously reported for Ag_2S NPs with bi-exponential decays. Again, a large variety of results have been found. The slow and fast lifetime values obtained for the here studied NPs are found to be significantly

larger than those reported by W.J. Mir et al.[106] (1 and 11 ns) but comparable to the values found by P. Jiang and co-workers[54] (10 and 75 ns). However, our results are in good agreement with the ones obtained by Zhang et al.[66] These last NPs are synthesized in a heat-up route based on AgDDTC while the others are not, which again shows the high dispersity in the results obtained for these NPs depending on the synthetic route.

2.2.5. *In vivo* brain thermometry

The as-synthesized hydrophilic Ag_2S NPs were successfully used for the *in vivo* temperature measurement inside a mouse's brain. The experiments were carried out by members of the Fluorescence Imaging Group led by Dr. Daniel Jaque at UAM, in particular, by Dr. Irene Chaves Coira, Dr. Nuria Fernández, and Dr. Luis Monge from the Faculty of Medicine in the Universidad Autónoma de Madrid. In a first stage, an ex-situ calibration temperature experiment was performed to correlate PL intensity and temperature. Further, the NPs were injected subcranially at the prefrontal cortex of the mouse using a syringe, as depicted in Figure 2.14.a. Thanks to the high penetration of the NIR-II photons in biological tissues, the emission from the NPs was able to propagate from the interior of the brain up to the NIR camera from which the intensity could be read and transformed into a temperature reading. The laser used for the NPs excitation operated at 822 nm and worked in a time modulated regime with a delay of 100 μs between pulses in order to avoid the laser-heating as a consequence of the skin and tissue absorption. The overlaid PL and brightfield images of NPs injected in the brain of a mouse can be observed in Figure 2.14b. The mouse was subject firs to a moderate temperature increase (below 7 degrees). From the PL signal of the previously injected NPs, temperature measurements can be recorded and compared to those obtained by infrared thermography (data not shown). These studies also evidenced the brain thermoregulation system that efficiently kept the brain temperature stable even in extreme hypothermia scenarios.

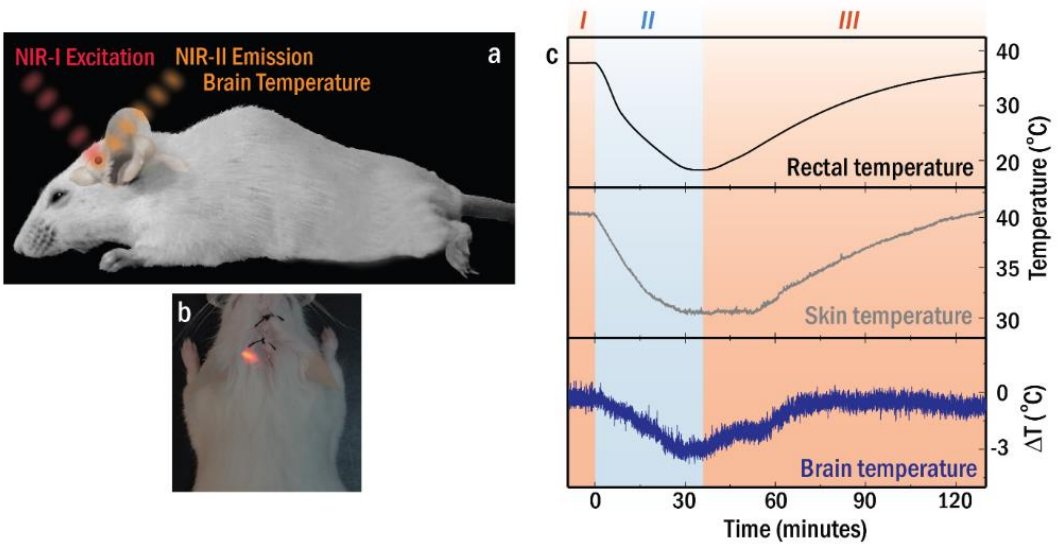

Figure 2.14. a) Scheme of the *in vivo* brain temperature measuring, b) Injection site c) Temperature change of the reactal, body and brain temperature of the mouse during a cooling process using a spray of isopropanol.

In this scenario and, in order to decrease the body temperature, the mouse was sprinkled with isopropanol. The cooling process was followed using a rectal thermometer, a thermographic camera to measure the skin temperature and using the change in the PL of the NPs *ex vivo* as shown in Figure 2.14c. Using the change of the PL of the NPs it was found that even when the body temperature falls up to 15°C the temperature inside the brain falls only 3°C with a much slower dynamic. Under further induced-comma scenarios (not shown), where the activity of the brain ceases, the NPs were capable to detect temperature changes below 1 degree. Thus, this result shows that Ag_2S NPs are efficient systems for simultaneous imaging and thermometry with high sensitivity.

2.3. Conclusions

Ag_2S nanocrystals have been synthesized using a previously reported heat-up route obtaining NPs with a dense surface coating that promotes the formation of aggregates of different sizes. The synthetic approach allows for the synthesis of NPs with narrow size distribution. HRTEM studies reveal the presence of NPS with a rich silver core. Although the effect of this core in their optical properties is still unclear, their optical bandgap could be determined by TAS measurements. Through different experiments these NPs have been found to be optimum for intensity and spectral position luminescence thermometry due to their high sensitivity and their ability to work even in a ratiometric approach with a temperature-independent sensitivity. The ability of the as-synthesized NPs for temperature sensing was first tested in an

ex vivo approach in which the NPs successfully monitored temperature changes due to laser-induced heating of dead tissue.

A new one-step ligand exchange procedure has been developed in order to successfully transfer these NPs to aqueous solutions, obtaining stable dispersions. Even though the change in the surface ligands causes the forming of surface defects states as observed in transient PL spectroscopy measurements, these NPs can be used for the *in vivo* temperature measurement maintaining their thermometric properties unchanged and showing good robustness even in acidic media since only the surface results affected after the ligand exchange and not the emissive core.

The final test for the applicability of the as-synthesized NPs was proven in a complex *in vivo* experiment inside a mouse's brain. The approach used for the experiment was intensity based due to the absence of possible diffusion (the injection was directly in the organ) and for the sake of experimental simplicity. The NIR PL allowed for the penetration through brain, bone and skin of the animal. This high penetration allowed for the monitoring of intensity changes that were successfully ascribed to temperature changes during different heating /cooling experiments. Thanks to this set-up and the high sensitivity of the NPs it was possible to observe the brain thermoregulation during an induced hypothermia, probing that these NPs are capable to measure small temperature changes (below 1 degree) *in vivo*.

Chapter 3. Novel hot injection route for the preparation of Se covered and core/shell Ag_2S-based NPs

3.1. Introduction

As discussed in Chapter 2, the heat-up synthesis of Ag_2S NPs produces aggregated NPs with an Ag-rich core. The observation of this aggregation has been reported since the early studies of Ag_2S NPs[40-42, 114] and it is also mentioned in more recent ones.[115, 116] In these reports, the formation of aggregates is ascribed to the high degree of monodispersity of the sample and the interdigitation of the thiolated ligands covering the NPs surface. However, not all highly monodisperse NPs synthesized using thiol ligands exhibit the formation of this kind of aggregates. This is indeed observed in the case of the synthesis of other metal sulphide NPs like $Cu_{2-x}S$, when using heat-up routes with alkylthiols.[117] The reason for the aggregation has not been deeply explored, but one report points out that primary amines as useful reactants to prevent it.[118] Despite the poor stability in dispersion of the aggregates, one of the main drawbacks of this kind of NPs is, as many authors have emphasized, the difficulty to further use these metal-sulfide NPs due to this dense surface coating thus reducing their potential applications.[119-123] For these reasons, the disaggregation of such NPs arrangements is essential for the applicability of these NPs. The main objective of this Chapter is to understand the formation of the heat-up based NPs and to develop an alternative route in order to obtain individual NPs with a different surface coating. To this aim, the reaction of silver (I) diethyldithiocarbamate (AgDDTC) and 1-dodecanethiol (DDT), which are the main reagents in the heat-up synthesis, has been studied by different techniques in order to identify the cause of the aggregation.

After that, stable Ag_2S NPs that can be further used as seeds to obtain Se-passivated Ag_2S NPs, $Ag_2S(S,Se)$ NPs, as well as Ag_2S-ZnS core-shell (CS) NPs, with improved optical properties.

As described in Chapter 1, the production of CS NPs is a successful strategy to optimize the optical properties of QDs in terms of PLQY values. The addition of layers of different semiconductor materials with higher energy band gaps (Type I CS NPs) allows for a more efficient charge carriers confinement and yields a dramatic increase of the PLQY. To synthesize an effective coating the crystalline structures of the core and shell materials must be carefully chosen. If the interface between both materials is not smooth (*i.e* large mismatch between the lattice parameters), trap states promote non-radiative de-excitation paths, thus reducing the PLQY. For CdSe, PbS and PbSe the most employed materials fulfilling these requirements are

CdS or Zn chalcogenides, because of their high bandgap and the appropriate matching between their crystalline lattice parameters.[124] In the case of Ag_2S, no homogeneous core/shell structure has been synthesized so far due to its uncommon monoclinic crystalline phase at RT. Only matchstick hybrid heterostructures have been successfully synthesized using ZnS, without any PL improvement with respect to Ag_2S NPs.[115] Therefore, the development of core/shell structure in Ag_2S is key in order to compete with other NIR emitters like PbS or PbSe, showing much higher PLQY values (up to 60%), but with important restrictions for biological studies due to their content of toxic heavy metals. In this Chapter, it is described how the new synthetic procedure along with a low temperature shell growing route allows the formation of core/shell Ag_2S/ZnS with improved optical properties. This strategy is complementary to others that also seek for enhance PLQY value, such as doping or ultrafast laser pulses irradiation-based post-treatments.[125]

Thanks to the here reported studies discerning the reason of the aggregation, the newly proposed synthetic approach and the possibility to further tune the composition of the NPs, Ag_2S, Ag_2S(S,Se), and CS Ag_2S/(Ag_2S,Se)/ZnS NPs can be synthesized and easily transferred to water achieving samples up to 6 times brighter than commercially available Ag_2S NPs dispersions. The chemical state and composition of all systems has been ascertained by X-Ray Absorption Spectroscopy (XAS) experiments at different absorption edges, using a synchrotron X-ray source.

3.2. Results and discussion

3.2.1. Identification of the reaction intermediate

It is known that the addition of metal salts to solutions that contain 1-dodecanethiol (DDT) form the corresponding metal dodecanethiolate. In the case of metals such as Au,[126] Cu,[127] Pd,[128] Ag,[129] Ni[130] or Pb[131] the resulting dodecanethiolate salts form polymeric structures with different phases: columnar, lamellar or amorphous. Particularly, in the case of Ag, the reaction taking place between AgDDTC and DDT yields silver dodecanethiolate ($AgSC_{12}H_{25}$).

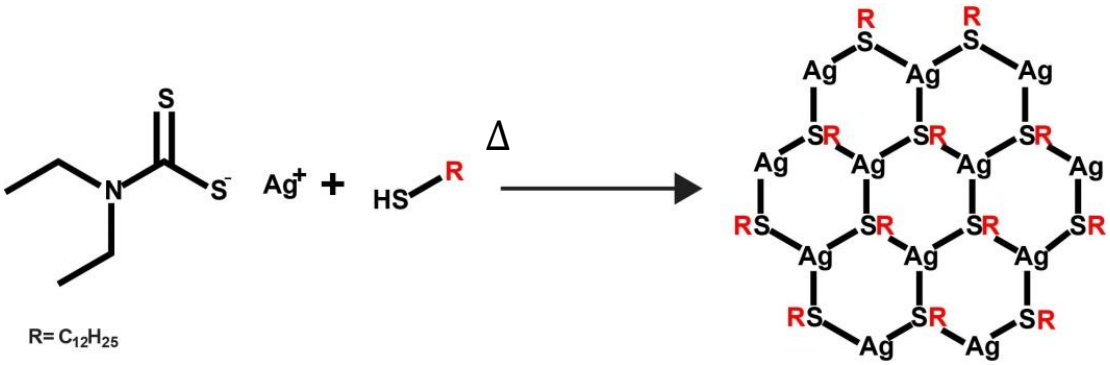

Scheme 1: Formation of $AgSC_{12}H_{25}$ in the reaction conditions

These polymers present high decomposition temperatures ranging from 200°C to 300°C.[129] Indeed, due to their high thermal stability, they have been used as templates for the synthesis of nanostructures of different shapes like sheets or wires.[132] In our case, the reaction intermediate between AgDDTC and DDT was isolated and studied by XRD and NMR. The presence of $AgSC_{12}H_{25}$ in the course of the reaction was confirmed by a simple XRD study as shown in Fig 3.1, where the XRD diffractograms of the AgDDTC used as silver precursor in the synthesis, $AgSC_{12}H_{25}$ produced following a previously reported route,[133] and the reaction intermediate are compared.

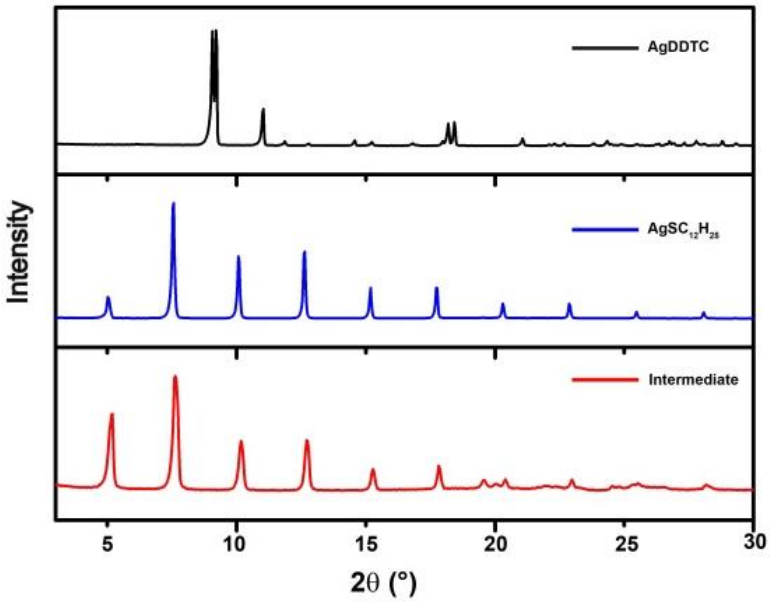

Figure 3.1. XRD diffractograms of the AgDDTC, $AgSC_{12}H_{25}$ and the reaction intermediate

The diffractogram of the intermediate matches very well the structure of the silver polymer indicating that the compound undergoing the thermal decomposition that starts the NPs' nucleation must be $AgSC_{12}H_{25}$, and not the AgDDTC used as silver precursor.

The high colloidal solubility and stability of the $AgSC_{12}H_{25}$ intermediate allows for its observation by TEM. As observed in Figure 3.2, the shape of the intermediate (Figure 3.2.a-b) reminds that of the aggregates obtained in heat-up routes (Figure 3.2.c-d), suggesting that the NPs may be embedded in this polymer. Indeed, the ability of metallic thiolates to embed other metal chalcogenide NPs has been previously observed for $Cu_{2-x}S$ obtained by thermal decomposition from copper dodecanethiolate and octanethiolate.[134] In order to confirm that this reaction intermediate drives the final surface chemistry of the as-synthesized NPs, different studies were carried out by means of NMR, a surface sensitive technique.

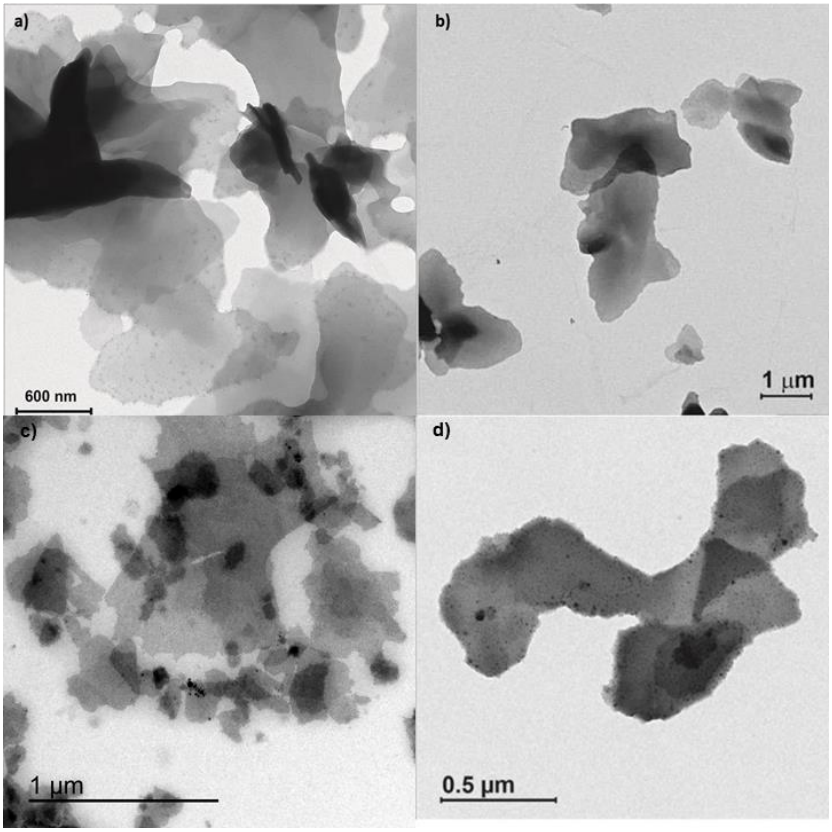

Figure 3.2. a-b) TEM images of the reaction intermediate and c-d) Low magnification TEM images of NPs arrangements

NMR offers a versatile toolbox to identify the nature of the different ligands and their strong or labile interaction to the NC surface.[135] Figure 3.3 compares the ^1H NMR spectra of (a) DDT, (b) a dispersion of Ag_2S NPs produced by heat-up and (c) the intermediate $AgSC_{12}H_{25}$. As

evidenced, most of the signals present in the Ag_2S NPs spectrum (b) are shared by the metal-organic polymeric product signals (c), and related to the protons in the α and β positions to the thiol group in the DDT spectrum (a) at $\delta = 2.50$ ppm and $\delta = 1.60$ ppm, respectively. The existence of DDT associated to colloidal quantum dots of different compositions or $CuInS_2$ NPs has been reported as a broad peak between 2.5 and 2.7 ppm.[121, 136] The presence of DDT, both as a free specie or bound to the surface of our NCs, is discarded by the absence of these signals in the spectrum shown in Figure 3.3.d.

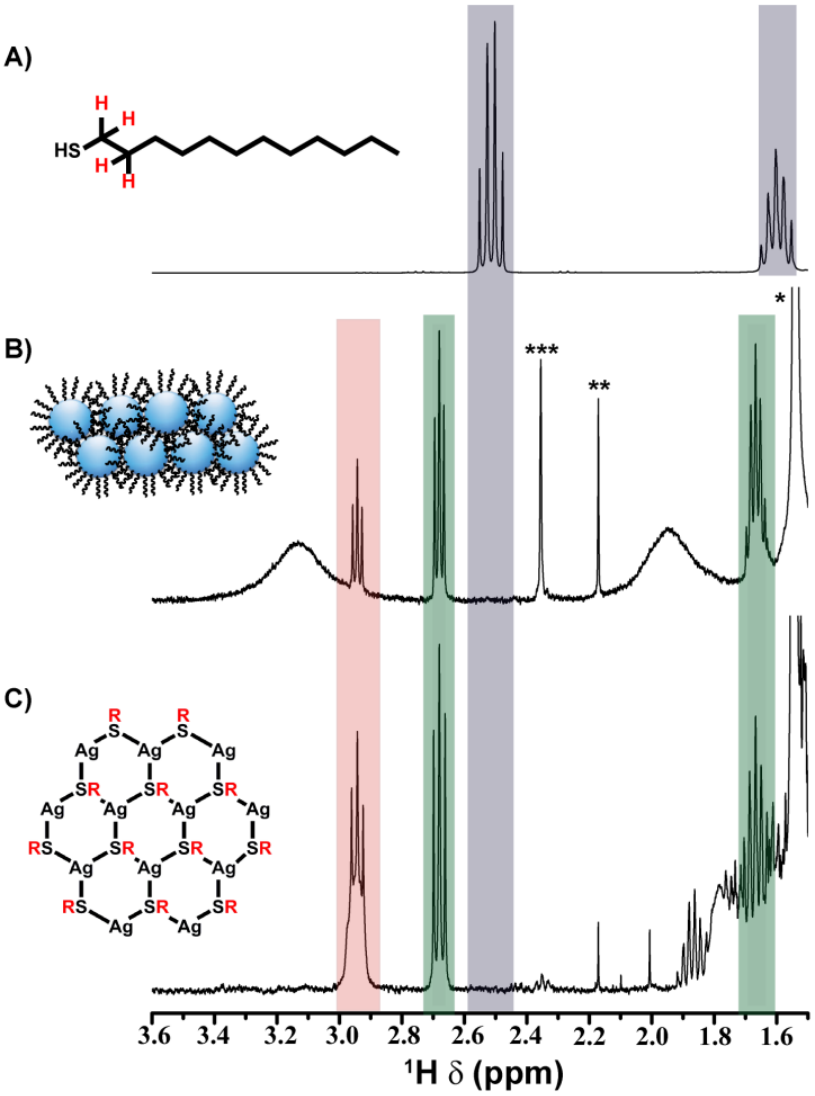

Figure 3.3 ^{1}H NMR spectrum of A) DDT, B) NPs synthesized by heat-up route A and C) the reaction intermediate (silver (I) dodecanethiolate). Signals marked in purple correspond to dodecanethiol, in green correspond to dodecyl disulfide and in red to silver (I) dodecanethiolate. Signals marked with three, two and one star (*) correspond to residual toluene, acetone and water, respectively. Insets depict DDT (a), NPs-aggregates by the effect of $AgSC_{12}H_{25}$ and the polymer, $AgSC_{12}H_{25}$.

The signals at 2.70 ppm and 1.65 ppm (marked in green), which are present both in the polymer ($AgSC_{12}H_{25}$) and the NPs spectra, are assigned to the α and β protons of the disulfide group in dodecyl disulfide ($C_{12}H_{25}SSC_{12}H_{25}$), a well-known side product in the synthesis of metal sulfide NPs, produced upon the oxidation in the course of the reaction of DDT.[119, 137]

Likewise, the $AgSC_{12}H_{25}$ and the NPs spectra share a triplet signal at 2.95 ppm related to the α-protons to the thiol group in the polymer. This signal, along with those related to dodecyl disulfide, are narrow and show multiplicity, suggesting that they are species can be forming part of the ligand shell, but are not directly anchored to the surface. In contrast, the spectra of the NPs exhibit two additional broad signals centered at 1.95 and 3.10 ppm. Their widths suggest a strong interaction with the NPs surface, which is confirmed by the Diffusion-Ordered Spectroscopy (DOSY) spectrum shown in Figure 3.4.

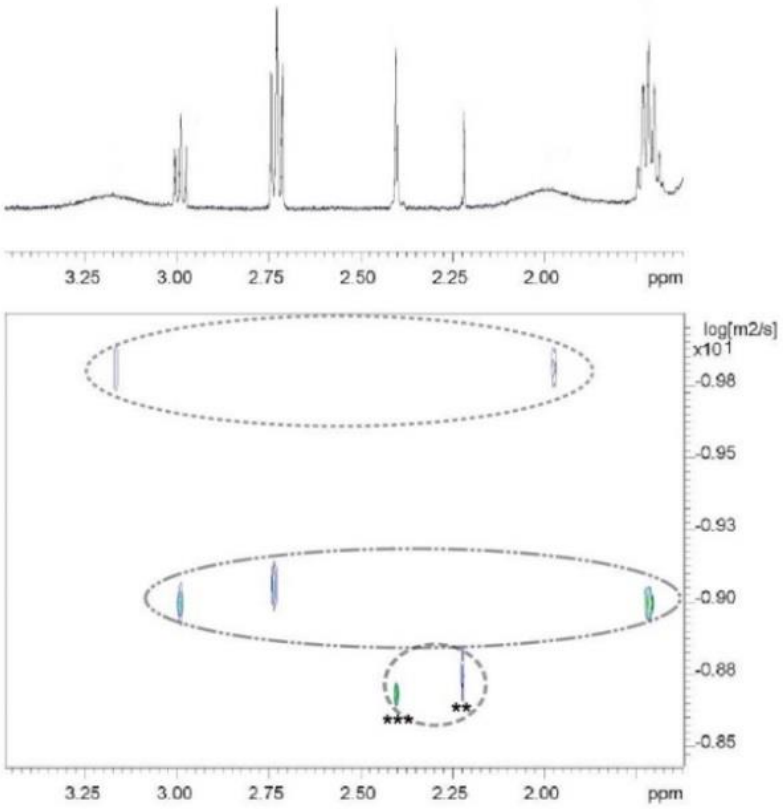

Figure 3.4 DOSY spectrum of NPs synthesized by the heat-up route. Signals are recorded using a diffusion time of 250 ms. From bottom to top, three set of signals can be distinguished, corresponding to solvents, non-anchored species and anchored species, respectively.

In this spectrum, two different sets of signals can be distinguished (apart from those coming from solvents marked with asterisks): signals with diffusion coefficients far from bound species ($\sim 1 \cdot 10^{-9}$ m^2/s), and two signals with diffusion coefficients of $1.4 \cdot 10^{-10}$ m^2/s, a reasonable value for tightly bound ligands to NPs surfaces.[138] The first set of signals is related to free $AgSC_{12}H_{25}$ (at δ=2.95 ppm) and dodecyl disulphide (at δ = 1.65 and δ = 2.70 ppm). The second set of signals at δ= 3.10 and δ = 1.95 ppm, is associated to the $AgSC_{12}H_{25}$ polymer. Applying the Stokes-Einstein relation (see Section 3.8 of APPENDIX I),[135] the hydrodynamic diameter of these species is calculated to be 5 nm, close to the size of the NPs observed in TEM images of the heat-up NPs (see Chapter 2).

3.2.2. Synthesis of monodisperse Ag_2S NPs based on a hot injection route

Silver salts are generally very insoluble and, in the case of these high molecular weight Ag-containing polymers, the only reported solvent is toluene near its boiling point (110°C).[139] The dissolution mechanism that these polymers undergo is still not clear, but several authors have postulated that, once these species are solubilized, monolayers of the metal alkylthiolate appear free-standing in solution.[128] In order to prevent the formation of stacks of these monolayers, toluene was used as solvent in the reaction. The injection of a sulfur source (sulfur powder dissolved in oleylamine, S-OLA) in this medium allows the nucleation of NPs. The S-OLA solution contains alkylammonium polysulfides at RT. However, upon heating, H_2S is produced causing the rapid formation of metal sulfide NPs upon injection.[140] The nucleation of the NPs in this synthesis takes place rapidly, as evidenced by the instantaneous change of colour of the reaction medium, from yellow to black, in sharp contrast with the slow colour change observed in heat-up routes. Figure 3.6a-b shows the result of the proposed hot-injection route, where the presence of non-aggregated but isolated NPs is evident. As discussed in Chapter 2, the heat-up synthesis yields Ag_2S NPs with an Ag-rich core. However, the hot-injection NPs consist of pure Ag_2S NPs, as can be concluded from the HRTEM studies shown in Figure 3.6 performed by Dr. Almudena Torres Pardo from the group of Dr. José María González Calbet, from Centro Nacional de Microscopía Electrónica de Madrid (CNME).

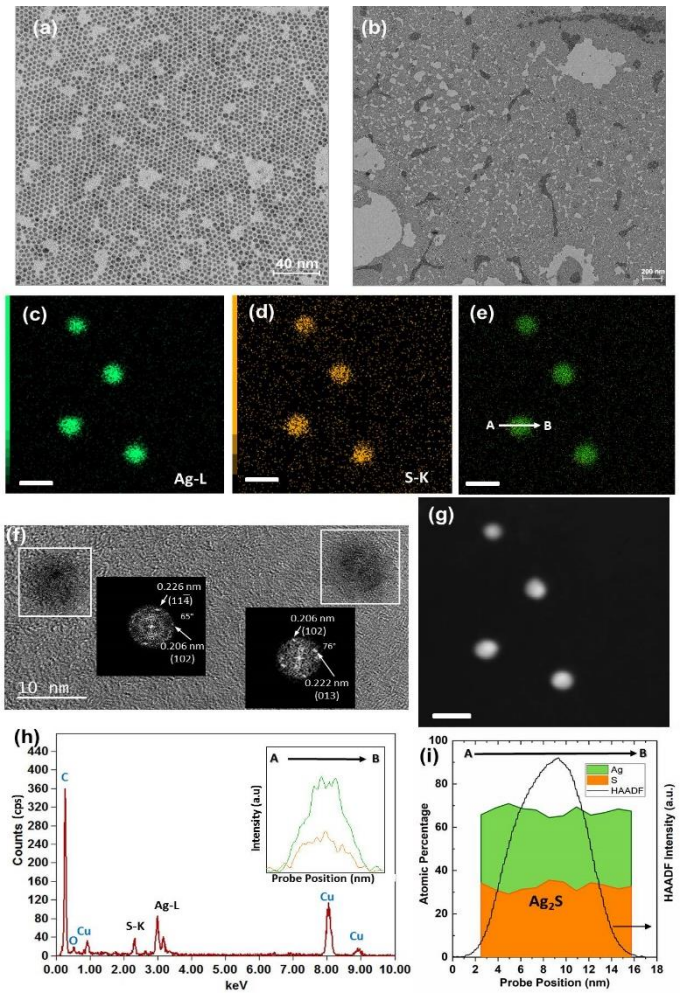

Figure 3.6. (a) and (b) TEM images of Ag_2S NPs obtained by the hot injection route at different magnifications. (c-e) EDS elemental mapping showing the spatial distribution of (c) Ag (green), (d) S (orange), and (e) Ag and S of the set of nanoparticles shown in (g). (f) HTREM images of Ag_2S nanoparticles. Insets show the FFT performed on each nanoparticle. g) HAADF-STEM of Ag_2S NPs used for the EDS mapping analysis. (h) Representative EDS spectrum of a NC. The corresponding X-ray intensity profiles extracted from the white arrow marked in image, (i) Atomic percentage of the previous intensity profile revealing Ag_2S composition for the NPs.

Figure 3.6c-e shows the elemental mapping distribution of the HAADF-STEM image of Figure 3.6g acquired in an aberration-corrected JEOL-JEM ARM300cF microscope operating at 80 kV in order to minimize the electron beam damage. The distances and angles obtained from the images and FFT analysis (Figure 3.6f) correspond to monoclinic acanthite Ag_2S phase (α-Ag_2S). The homogeneous distribution of Ag and S is revealed by the analysis of the EDS spectrum (inset of Figure 3.h) across the NC marked with an arrow in Figure 3.6e. The corresponding X-Ray intensity profile shown in Figure 3.6h as inset, as well as the quantification of the intensity profile shown in Figure 3.6I, confirm the presence of NPs with a composition close to the stoichiometric Ag_2S. The α-Ag_2S phase acanthite is also acertained by XRD measurements, as shown in the diffractogram shown in Figure 3.7, showing peaks corresponding to the (-112), (-

121) and (200) planes. The broadened peaks are the result of the nanocrystal size, which is estimated in 7.9 nm following the Scherrer formula, a size in relative good agreement with the HRTEM inspections previously reported in Figure 3.6.

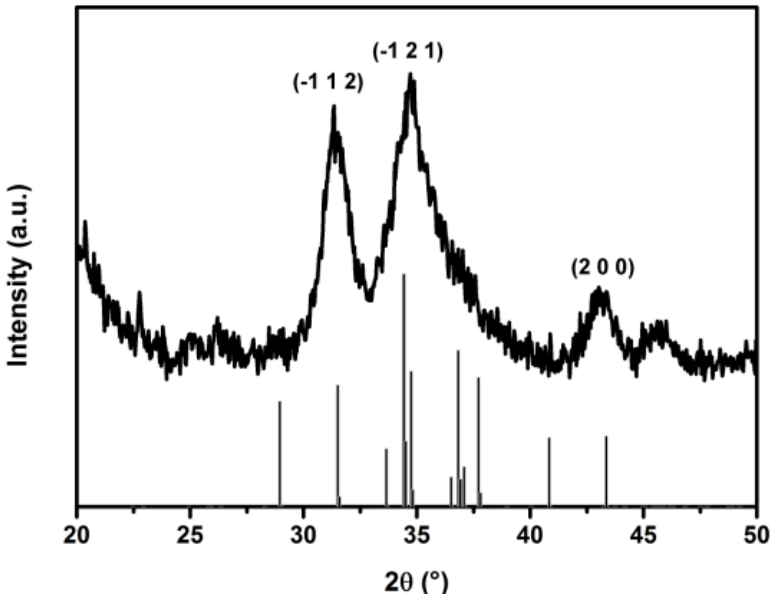

Figure 3.7. XRD diffractogram of the Ag_2S NPs synthesized by the newly described synthetic procedure

This synthetic route does not allow fine emission wavelength tunability due to a combination of the rapid growth of the nanocrystals and the limited size-range to observed quantum confinement effects, as discussed in Chapter 2. This low tunability and the size-PL relation matches the ones obtained in non-polar syntheses as compared to data presented in Figure 1.8. (Chaper 1).[125] Therefore, as it is shown in Figure 3.8a, the absorption and the PL emission spectra hardly change during growth for NPs above 6 nm. On the other hand, the emission lineshape suffers a modulation as a consequence of the optical absorption of water after ligand exchange, as shown in 3.8b, similarly to that reported in the previous Chapter.

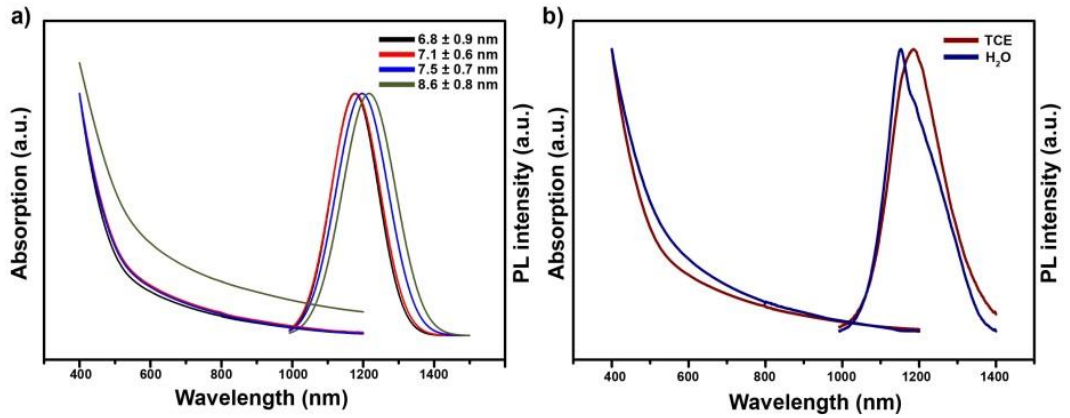

Figure 3.8. a) Optical absorption and photoluminescence spectra of different aliquots of Ag_2S NPs with different sizes (specified in the legend) and b) optical absorption and photoluminescence spectra before (dark red) and after (dark blue) the ligand exchange procedure. Red line corresponds to NPs in tetrachloroethylene (TCE) and blue line for NPs transferred to water.

The role of OLA in this synthesis is not only the activation of sulfur to produce H_2S, but also to define the final surface chemistry of the NPs, as evidenced in the ^1H NMR spectra shown in Figure 3.9. Indeed, OLA is found to bind strongly to the surface of these NPs, as suggested by the broad peaks at δ = 5.3 ppm and δ = 2.0 ppm in the ^1H NMR spectrum. In these samples we can also observe narrow signals from dodecyl disulfide and free $AgSC_{12}H_{25}$, suggesting that these species might be intercalated between the anchored OLA ligands. However, no evidence for the broad signal at δ = 3.10 ppm can be distinguished, which confirms the absence of anchored $AgSC_{12}H_{25}$ to the NPs surface.

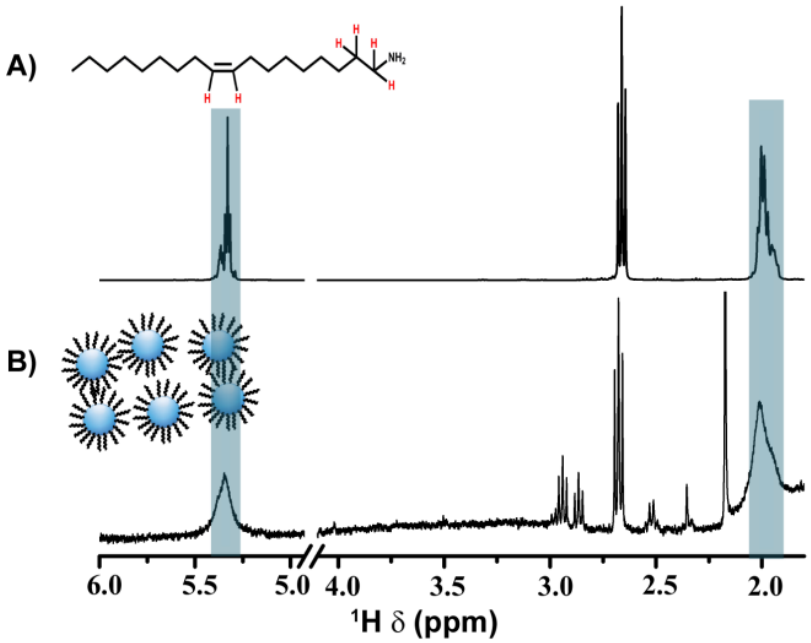

Figure 3.9. ^1H NMR spectrum of a) Oleylamine and b) NPs synthesized by the hot injection route.

The importance of this difference in the NPs' surface is that the Ag_2S NPs obtained by this novel route, free of the $AgSC_{12}H_{25}$ polymer as ligand, are easily ligand-exchangeable with water-soluble polymers like thiol-modified polyethylene glycol, providing bright water-soluble NPs stable in solution for months. The evidence for a better ligand exchange process due to the presence of OLA on the surface of the NPs is studied by Inductive Coupled Plasma Optical Absorption Spectrometry (ICP-OES). When heat-up NPs are exposed to a ligand exchange procedure, only 15% of the silver mass in the NPs is transferred to water. However, when the hot injection NPs are exposed to the same ligand exchange procedure, 67% of them end up in the aqueous phase. Thus, the elimination of the dense coating of the polymer is a major advantage for post-reaction treatments of the NPs.

Sample	Ag^+ mass in chloroform (mg)	Ag^+ mass in water (mg)	Yield (%)
Heat-up NPs	1.923±0.008	0.282±0.005	15
Hot injection NPs	1.536±0.004	1.022±0.001	67

Table 3.1. Ligand exchange yield measured by ICP-OES

3.2.3. Synthesis and optical properties of Ag_2S/Ag_2(S,Se)NPs

The disaggregation and good colloidal stability provided by this route allows not only for an easier ligand exchange, but also for further control of their optical properties by post synthetic procedures. The aggregation and dense coating of the heat-up synthesized NPs has hindered their controlled surface modification due to the dense coating that prevents the NPs to react, individually, with new chemical species. However, the novel hot-injection synthesized NPs can be used as seeds for the preparation of more complex structures with improved properties. The addition of a solution of Se powder in TOP (Se@TOP) in a quantity equivalent to the growth of roughly a monolayer of Ag_2Se on the surface of the NPs yields NPs with improved optical properties while maintaining their size dispersion as observed in Figure 3.10. Figures 3.10a-b correspond to TEM images of Ag_2S NPs after the treatment with Se@TOP. Figure 3.10.c shows an histogram with the size of those treated NPs, with a mean size of 8 nm, what implies the growth of about 1 nm respect to the Ag_2S seeds while the size dispersity is

maintained. Thus, the addition of Se increases the NP size around 1 nm in diameter and slightly shifts the PL response to the red, as observed in Figure 3.10.d.

The addition of a higher quantity of Se does not generate an improvement in their optical properties and degrades their colloidal stability due to the presence of unreacted Se@TOP.

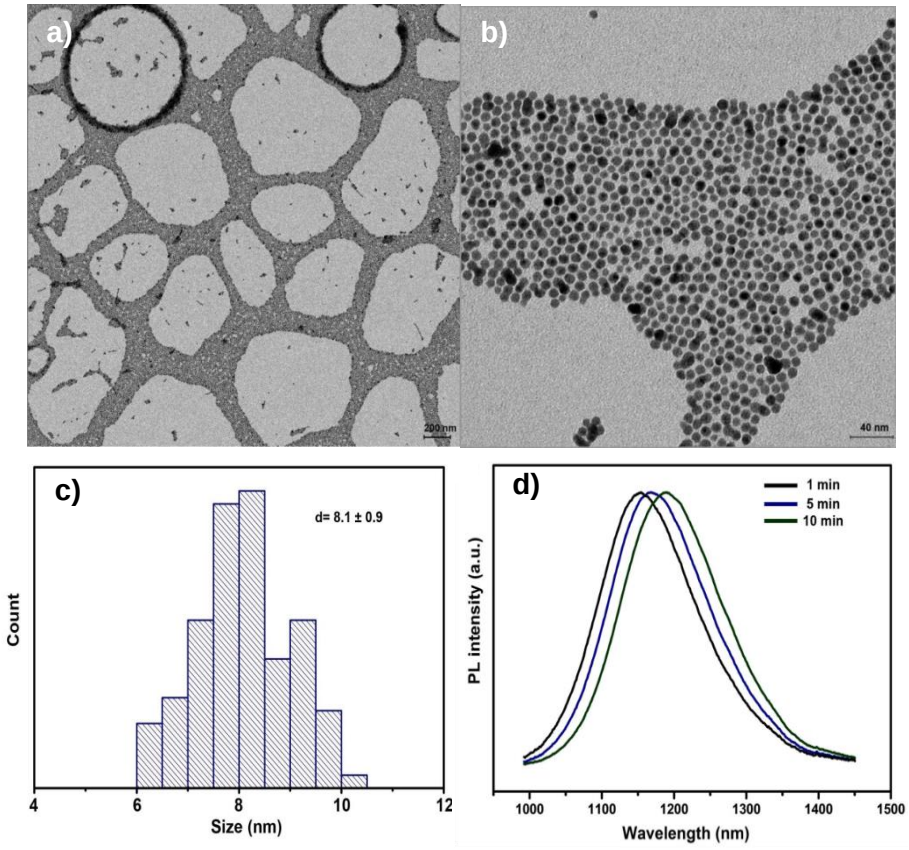

Figure 3.10. a) and b) TEM images at different magnification of the as-synthesized $Ag_2S/(Ag_2S,Se)$. c) Size dispersion of the NPs and d) PL evolution since the Se@TOP injection

The increase in the PL intensity can be easily observed in Figure 3.11.a, where a comparison of the PL intensity of Ag_2S and Ag_2S NP treated with Se at λ=822 nm is shown. The QY measured using an integrating sphere (Figure 3.11.b) was found to be up to 3 times higher than that of the original Ag_2S NPs. The fact that the PLQY of the hot injection NPs in organic media is lower than the one of the heat-up synthetized NPs (PLQY=2.5 %) might be related to the surface. As discussed in Chapter 2, surface capping is one of the most critical parameters in the emission efficiency in NPs. The dense coating around the NPs produced by means of the heat-up route may isolate very effectively the surface from oxygen and water thus protecting the emissive

core. In contrast, the hot injection NPs' surface, with a lighter surface density is more exposed to oxidation or uncapped surface defects that may harm their efficiency.

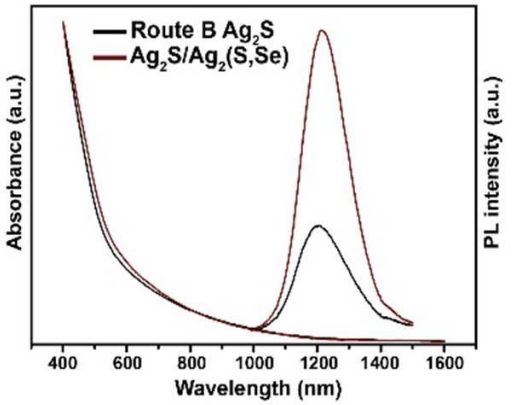

Sample	PLQY (%)
Ag_2S NCs	0.24
$Ag_2S_{1-x}Se_x$ NCs	0.65

Figure 3.11. a) Comparison of the PL of Ag_2S and $Ag_2S/(Ag_2S,Se)$ NPs at λ_{exc}=822 nm and b) PLQY measured using an integrating sphere

Furthermore, and importantly, according to its ^1H NMR spectrum (Figure 3.12), the growth step in the presence of Se does not modify the ligand sphere of the hot-injection NPs, allowing for similar ligand exchange procedures as the one developed for the previously described Ag_2S NPs.

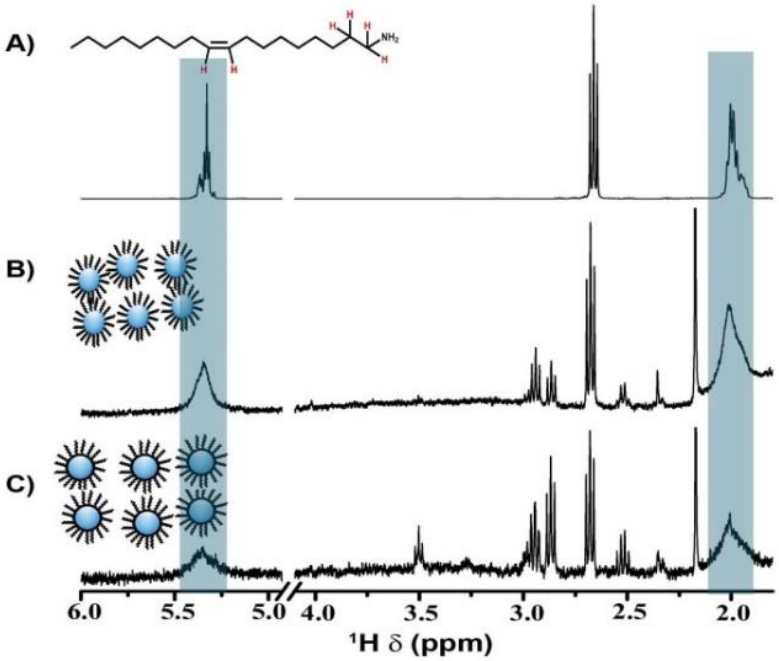

Figure 3.12. ^{1}HNMR spectra of a) OLA, b) route B NPs, and c) $Ag_2S_{1-x}Se_x$ NPs.

Since the main application of these NPs requires their aqueous compatibility, rather than PLQY values in organic media, those in water or a fair comparison of their PL in aqueous media are far more relevant.

Figure 3.13 shows the comparison of Ag_2S NP and $Ag_2S/Ag_2(S,Se)$ NPs produced by hot-injection compared with commercial ones, presumably synthesized by heat-up methods. All samples have the same optical density (0.1 a.u) and have been excited at the same wavelength (822 nm). As it can be observed the PL of $Ag_2S/Ag_2(S,Se)$ NPs is 3 times more intense than that of the commercial Ag_2S NPs. Thus, the Se coating successfully allows for the improvement of the PLQY even after the ligand exchange. This hot-injection method allows for the synthesis of water soluble NPs with enough PLQY to be used for biological applications, as will be further evidenced.

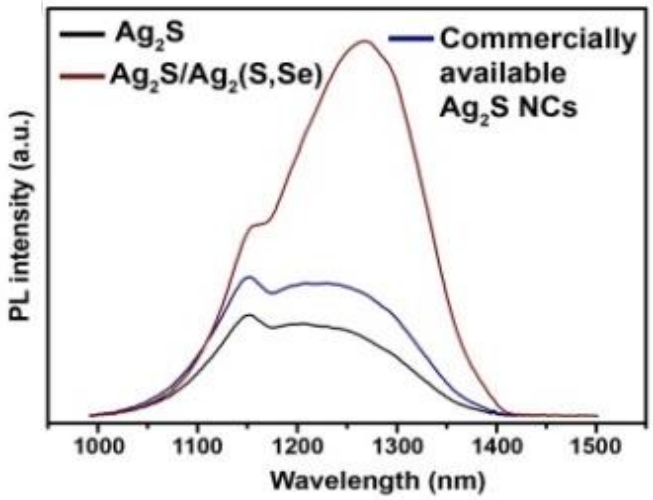

Figure 3.13. Comparison of the PL between Ag_2S, and $Ag_2S/Ag2(S,Se)$ NPs both produced by hot-injection and commercial ones .

3.2.4. Chemical and structural composition of the $Ag_2S/Ag_2(S,Se)$ NPs

In order to elucidate the incorporation of Se in the Ag_2S matrix (its location on the surface or in the volume), EDX and EELS studies were performed in an aberration-corrected JEOL-JEM ARM300cF microscope. However, due to the low quantity of Se in the samples EDX mapping was not able to properly resolve the structure. For this reason, XAS studies including XANES (X-Ray Absorption Near Edge Structure) and EXAFS (Extended X-Ray Absorption Fine Structure), were performed by our collaborator Martín Mizrahi from Félix G. Requejo's group, at the Universidad Nacional de La Plata (Argentina). The results at the Ag L3- and S K-edges can be seen in Figure 3.14A and 3.14B for Ag_2S NPs before and after ligand exchange and with and

without Se. As can be seen in Figure 3.14A, the XANES spectra at the Ag L3-edge in Total Electron Yield (TEY) mode, are almost identical in all samples. The same results are obtained from the signal acquired in fluorescence mode (not shown here). The shape of these spectra is also similar to those that present for reference materials, Ag_2S, Ag_2Se[141] and for silver NPs with dodecanethiol.[142] Thus, a clear identification of the formed species is not straightforward in the silver edge.

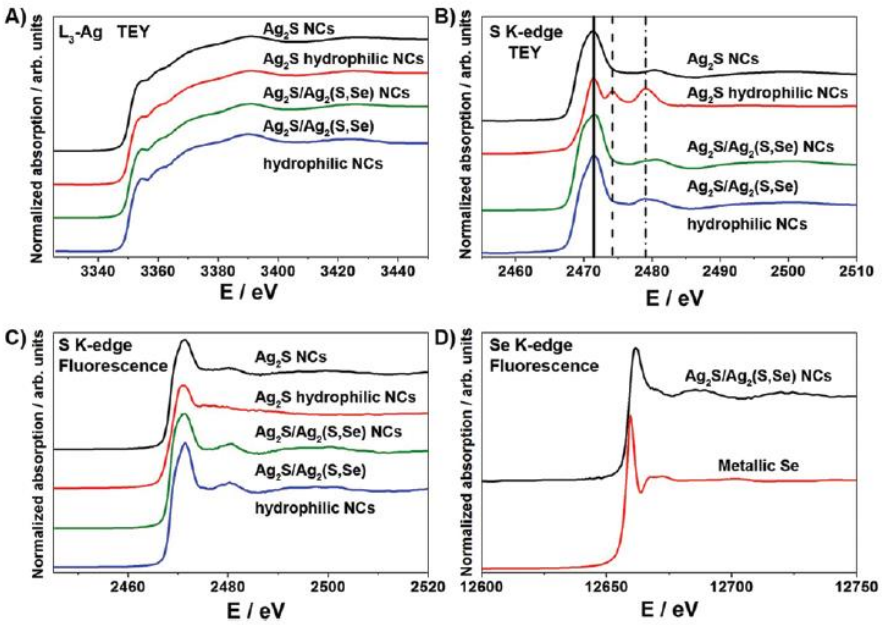

Figure 3.14. XANES spectra of the studied Ag_2S samples before and after ligand exchange, and with and without Se, performed in TEY mode at the Ag L3-edge (A) and S K-edge (B). (C) XANES spectra of the studied Ag_2S samples before and after ligand exchange, and with and without Se, performed in fluorescence mode at the S K-edge. (D) XANES spectra of the $Ag_2S/(Ag_2S,Se)$ sample, performed in fluorescence mode at the Se K-edge.

XANES spectra at the S K-edge taken in TEY mode (Figure 3.14B), show a main contribution at 2473 eV (vertical solid line) associated to the presence of S^{-2} in all samples. Ag_2S NPs after ligand exchange (denoted as Ag_2S hydrophilic NPs, red line), present other two resonances at 2476 eV (vertical dashed line) and 2481 eV (vertical dashed-dotted line), corresponding to the presence of sulfur with valence states +4, and a mixture of +5 and +6, respectively. It is worth to note that these resonances do not appear in the hydrophilic sample with Se, and were not observed in any of the samples when the absorption signal is taken in fluorescence mode (Figure 3.14c), being in this last case all the signals measured corresponding to S^{-2}.

TEY mode is sensitive to the surface atoms state, while the fluorescence mode is volume sensitive, giving an averaged information from the whole NC. The comparison of both spectra shows that the Se atoms are located on the surface of the NPs, preventing the oxidation of S when the sample is in aqueous media. This extra layer is not only favoring the PLQY of the NPs but is also acting as a protection layer that isolates their surface from the air oxidation improving their long-term stability. However, the XANES spectra do not present any information about the chemical state of Se in the Ag and S absorption edges due to the difference in the concentration of Ag and S compared to the one of Se. For this reason, XAS measurements (XANES and EXAFS) were performed at the Se K-edge. The XANES region performed in fluorescence mode (Figure 3.14D) for Ag_2S NPs treated with Se@TOP show all the features present in the spectrum corresponding to the Ag_2Se reference sample,[143] and completely different from the spectrum of metallic Se, so the presence of Se^0 covering the NPs can be discarded. The Se atomic distribution in the Se-treated NPs was analysed by probing the local structure around Se atoms by EXAFS. This technique provides structural information of both homogeneous and non-homogeneous nanomaterials by the analysis of the fitted averaged coordination numbers and interatomic distances.[144] Figure 3.15A shows the magnitude of the Fourier Transform (FT) of the EXAFS oscillation obtained at the Se K-edge, and simulated spectra using FEFF code[145] for Ag_2Se and SeS_2. The FT of the sample presents two principal peaks at 1.8 Å and 2.5 Å (without phase correction). These contributions are approximately in the same positions that the obtained for the Ag_2Se structure, in accordance with the XANES results.

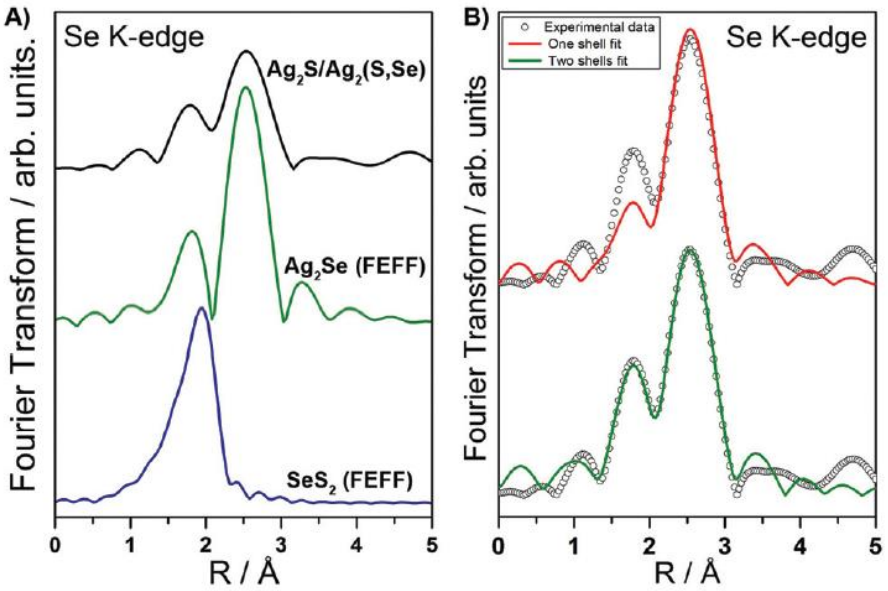

Figure 3.15. A) k^2-weighted Fourier Transform of the EXAFS oscillation for the $Ag_2S/(Ag_2S,Se)$ NPs (black line), simulated spectra obtained using the FEFF code for Ag_2Se (green line) and SeS_2 (blue line). B) k^2-weighted Fourier Transform of the EXAFS oscillation for the $Ag_2S/Ag_2(S,Se)$ NPs (circles), together with the fitting models proposed: one shell Se-Ag (red line) and two shells Se-Ag and Se-S (green line).

We can observe a difference in the intensity ratio between these peaks, being roughly 1/2 for the studied sample, and roughly 1/3 for the theoretical structure of Ag_2Se (see Figure 3.15A). This difference can be attributed to the presence of some S atoms in the neighborhood of Se. To verify this hypothesis, two fit models were proposed. The first one considers only one shell of Ag atoms around the Se sites. The result of the fit is shown in Figure 3.15B (in red), and as it can be seen, its quality is not satisfactory enough, especially for the first peak. The second model, which adds a new coordination shell for Se, containing S atoms, shows a much better fitting result (Figure 3.15B (in green) and Table 1 in Section 3.7 of APPENDIX I.

The Ag_2Se alloy has seven Ag atoms as first neighbors of the Se ones, with interatomic distances (R_{Se-Ag}) between 2.7 and 2.9 Å. For the sample treated with Se, the average coordination number (N_{Se-Ag}) obtained from the fit (N_{Se-Ag}= 2.8, see Section 3.7 in APPENDIX I) is lower than expected (i.e. seven Ag atoms), and also the presence of some S atoms in the structure is needed to improve the quality of the fit (Figure 3.15B). The presence of some S atoms in the structure would lead to a reduction in the N_{Se-Ag}, but this could not fully explain the reduction found. On the other hand, the reduction in the N_{Se-Ag} can be a consequence of both, the nanometric size of the NPs and the superficial location of Se in the NPs. Indeed,

those Se atoms on the surface of a NC contribute with a lower N_{Se-Ag} that those in the bulk. Thus, for a NC of about 8 nm of diameter (according to TEM measurements), a reduction of less than a 5% in the N_{Se-Ag} can be expected. Since in these NPs the decrease is higher (60%), to explain this additional reduction for the N_{Se-Ag}, it is necessary that the Se atoms form an $Ag_2S/(Ag_2S,Se)$ structure, preferably in a thin layer (less than 1 nm) over the surface of the Ag_2S NPs.

3.2.5. Synthesis and optical properties of $Ag_2S/(Ag_2S,Se)/ZnS$ NPs

The amount of available surface on the individual $Ag_2S/(Ag_2S,Se)$ NPs synthesized by the hot-injection route allows for more post-synthetic reactions. As previously discussed, the growth of semiconductors of different nature on Ag_2S is a tricky task due to the impossibility of using classical shell growing techniques for this semiconductor. Treatments at high temperatures cause the irreversible quenching of the PL in these NPs due to ripening. Consequently, other techniques are required for the growth of this kind of structures. Different approaches were followed to obtain the coating of the NP with an homogeneous layer of a Zn-based semiconductor (see Scheme 3.1). However, only one was found to produce an increase in the PL intensity, which is described in Section 3.9 of APPENDIX I. In this procedure, $(ZnOA)_2$ is generated from the reaction of $Zn(Ac)_2{\cdot}2H_2O$ and oleic acid at 100°C.

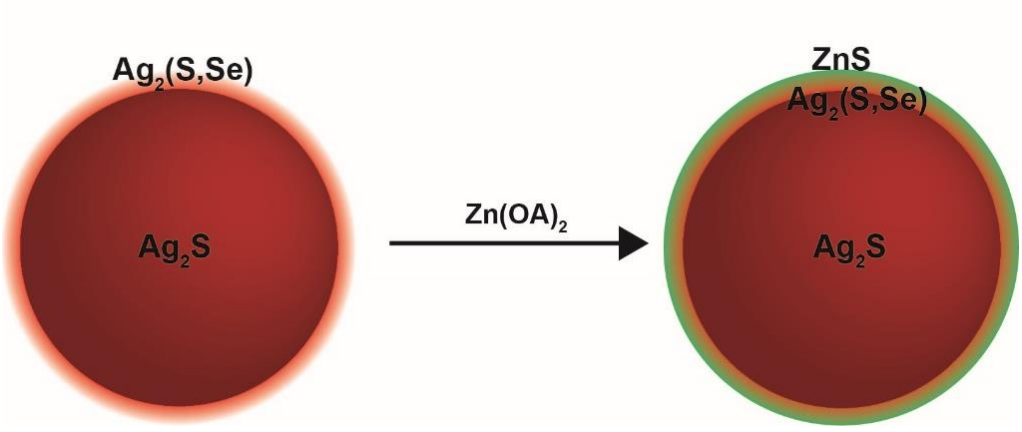

Scheme 3.1. Shelling reaction of the $Ag_2S/Ag_2(S,Se)$ NPs.

The addition of the $Ag_2S/(Ag_2S,Se)$ NPs triggers the decomposition of the zinc precursor forming a thin layer of ZnS around the NPs. Three different Zn quantities were introduced in the reaction system as calculated for the growth from 1 to 5 monolayers (MLs) of ZnS (detailed

calculation of the quantities required for the growth are in Section 3.10 of APPENDIX I). The obtained NPs can be observed in the TEM images shown in Figure 3.16.

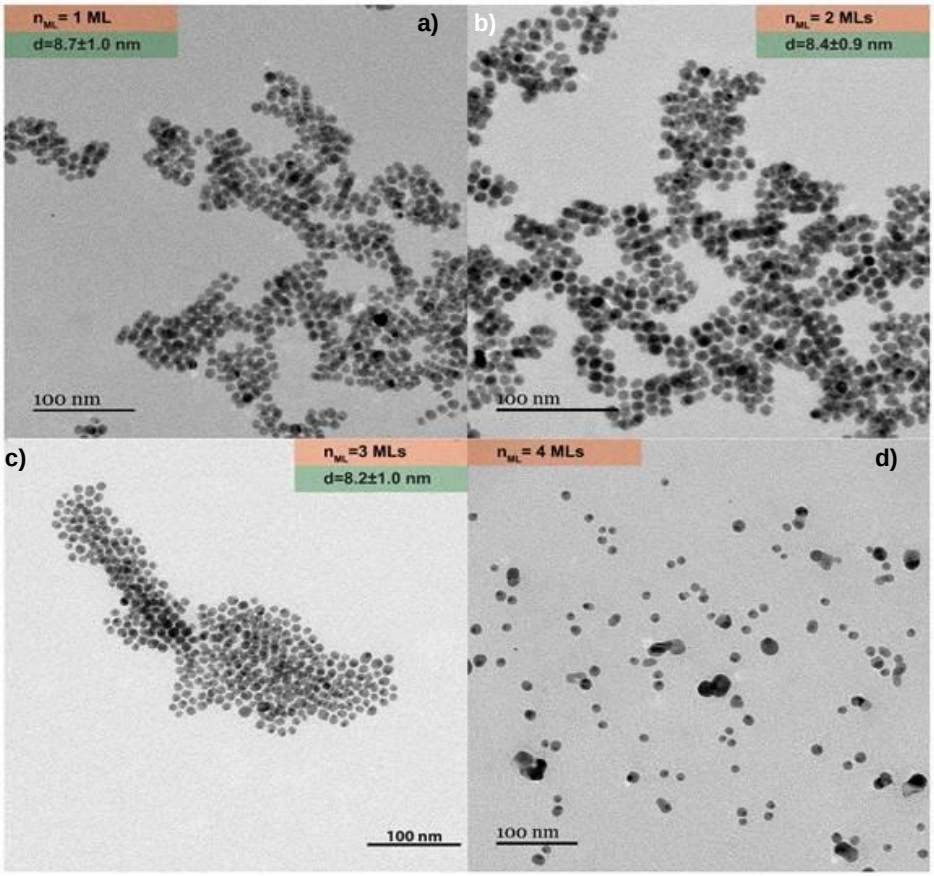

Figure 3.16. Size and morphology of different CS Ag_2S/ZnS NPs depending on the feeding ratio of Zn precursor

The size and size dispersion of the NPs are included in each TEM image for the different number of ZnS MLs. As can be observed, the size of the CS NPs is not appreciably increased after the Zn coverage except for the highest amount of Zn precursor, where NPs lose their morphology and photo luminescent properties due to ripening. In this last case, the presence of a second population of Zn-based NPs is also observable, which is the result of a new homogeneous nucleation and growth events out of the NPs´ surface.

The improvement in the optical properties of these NPs is evident when the PL intensity emitted by the NPs (Figure 3.17) is studied. The PL intensity at the same NP concentration is found to increase up to three times for Ag_2S/Ag_2(S,Se) treated with the equivalent of 1-3 MLs.

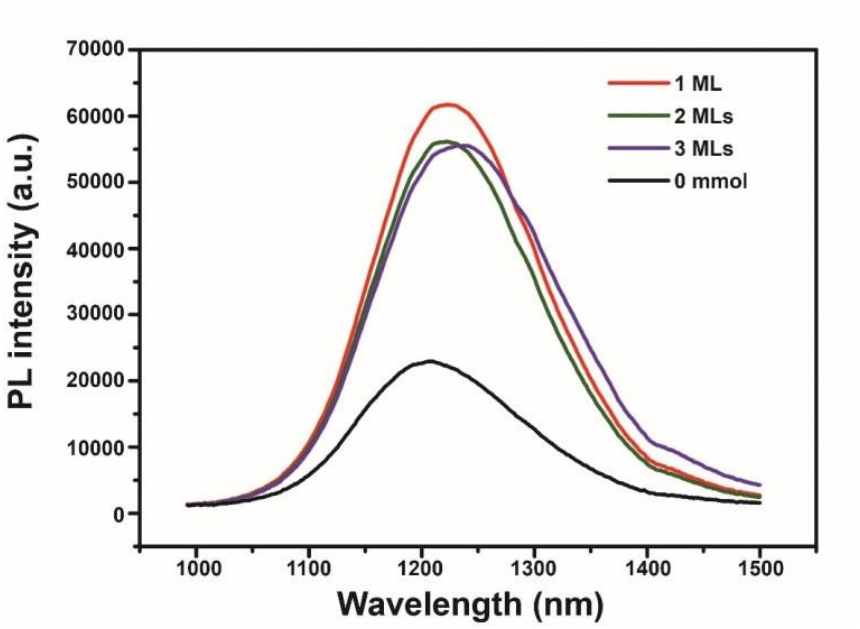

Figure 3.17 PL intensity of $Ag_2S/Ag_2(S,Se)$ samples with different ZnS monolayers.

In order to fully characterize the material grown on the surface of the NPs, XAS measurement were carried out following the same procedure developed for the study of the $Ag_2S/(Ag_2S,Se)$. For the XAS measurements it was found that thorough washing of the NPs was necessary in order to unambiguously assign the chemical state of Zn in the structure. Zinc salts are generally difficult to wash out from NPs, due to their low solubility in the commonly used organic washing solvents. The correct assignation was not possible in non-thoroughly washed (around 15 washing steps, as described in APPENDIX I) samples since the resonances coming from the unreacted Zn precursor blurred the signal from the Zn chalcogenide.

Figure 3.18 compares the K-Zn absorption edge of $Ag_2S/Ag_2(S,Se)$ NPs treated with 3 MLs of Zn precursor with three standard samples consisting on commercially available ZnSe, ZnS and Zn acetate. Since $Ag_2S/Ag_2(S,Se)$ NPs contain Se, so it is expected that a ZnSe shell forms upon treatment with Zn. Interestengly, as depicted in Figure 3.18, as a first sight, the absorption edge of the NPs in the Zn K edge resembles that of ZnS (not ZnSe), although it does not completely match any of the references. In order to unambiguously determine the Zn species formed in the reaction, the atomic environment of the Zn atoms was studied using EXAFS (Figure 3.19).

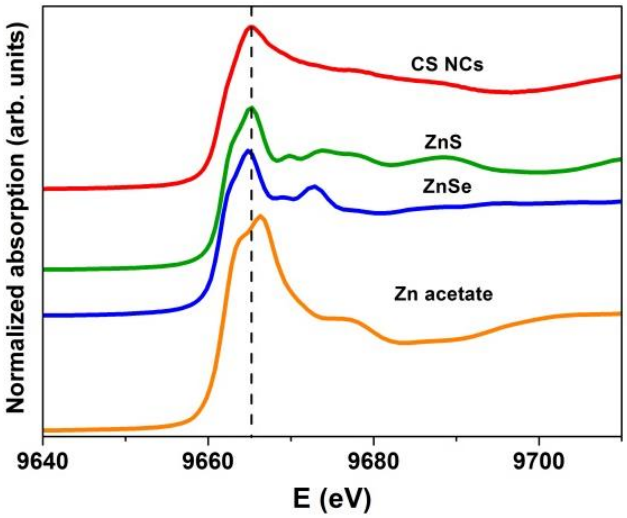

Figure 3.18. XANES spectra of the NPs compared to ZnS, ZnSe and $Zn(Ac)_2$

EXAFS confirms that the atomic distances are consistent with the model of Zn bound to S atoms since the maxima and minima of the oscillation match the ones of ZnS. However, a closer examination of the EXAFS oscillations, reveals a contribution from the Zn-O bond in $Zn(Ac)_2$, which can be observed as a shoulder of the Zn-S bond distance. This implies that the washing steps after the shelling reaction (15 washing steps) were not enough to fully eliminate the entire Zn precursor from the sample.

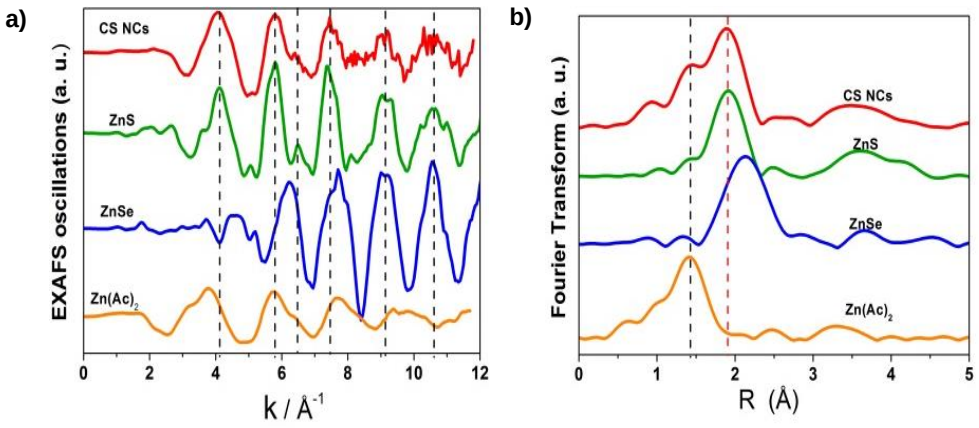

Figure 3.19. a) EXAFS oscillations of the NPs compared to the references and b) FT of the XANES spectra

Due to the chemical nature of ZnS, different surface ligands have been used for the capping of CS NPs with a ZnS shell. Different atoms, like oxygen or nitrogen, have a higher binding energy to the surface of ZnS that to a Ag_2S one. It is then expected that, if the NPs are correctly and homogeneously covered by ZnS, they show a change in the affinity for different ligands. To test this hypothesis, we subject these CS Ag_2S/(Ag_2S,Se)/ZnS NPs to the previously described ligand exchange procedure, this time with molecules showing different functional groups. The results are shown in Figure 3.20a, which shows the PL response of water soluble CS Ag_2S/(Ag_2S,Se)/ZnS NPs functionalized with Polyvinylpyrrolidone (PVP), methoxypolyethylene glycol amine (PEG-NH_2) and poly(ethylene glicol) bis(amine) (NH_2-PEG-NH_2).

These polymers were similarly attempted on the Ag_2S/(Ag_2S,Se) without success. PVP did not bond to the surface (the binding energy of O to Ag is lesser than the one of S) and in the case of amine-derived PEG polymers the NPs could be transferred to water but were reduced in a few minutes interval (easily observable since the dissolution of the NPs formed a silver mirror appearance). Figure 3.20 demonstrates that using non-thiol containing polymers successful hydrophilic NPs could be prepared due to the change in the surface chemistry after the addition of the ZnS external layer. Therefore, the formation of the ZnS not only allows for the preparation of more efficient light emitters but it also improves the versatility and functionalization of the as-synthesized NPs.

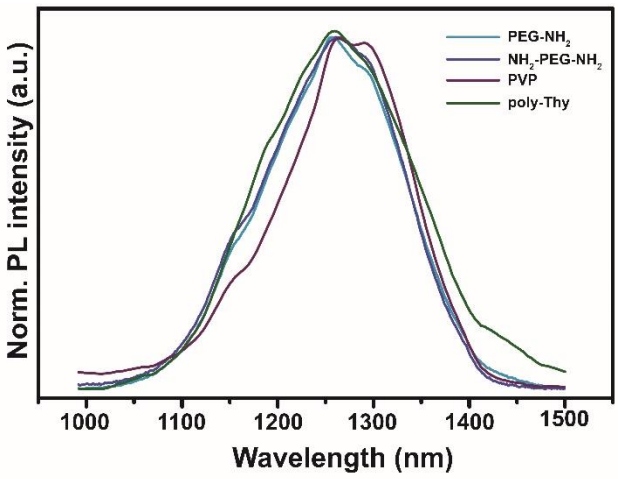

Figure 3.20. a) PL intensity of hydrophilic NPs capped with PVP, PEG-NH_2, NH_2-PEG-NH_2 and with a polythymine oligonucleotide.

Furthermore, the CS NPs could be exchanged using a poly-thymine oligonucleotide synthesized by Álvaro Somoza's group at IMDEA Nanociencia. Different oligonucleotides have been used in the last years for the modification of NPs due to their ability to bond to complementary bases of RNA or DNA. This is exploited to promote cell death or the inhibition of a certain gene. In this case, a thiol modified polythymine oligonucleotide composed of 12 monomers was incubated with the CS NPs. Polythymine terminated oligonucleotides are known to promote cell death. The success in the functionalization of CS NPs with this ligand opens up the possibility of a simple one-step functionalization of these highly efficient CS NPs with biomolecules that could have a direct therapeutic, targeting application or to favor the internalization in certain tumorous cells.

3.3. Conclusions

The reason for the formation of aggregates in the heat-up synthesis of Ag_2S NPs has been elucidated thanks to XRD and NMR studies. The results show that the intermediate species silver (I) dodecanethiolate does not completely decompose under the synthesis conditions not only affecting the colloidal stability of the as-synthesized NPs but also strongly capping their surface, generating aggregated systems, where further functionalization is hindered. The removal of this intermediate was possible by adding the effect of hot toluene in the separation of the polymeric lamellae and the effect of a primary amine (in this case oleylamine) as a sulfur activator in a new hot-injection synthetic route. The NPs synthesized using the newly developed route have proven to consist on purely Ag_2S and show NIR PL in the NIR-II plus a much efficient surface modification due to the more labile oleylamine molecules capping their original surface. Furthermore, their easier surface chemistry allows for their surface modification opening the door to grow layers of different compositions on their surface

including a simple passivation with Se $Ag_2S/Ag_2(S,Se)$ or core-shell NPs $Ag_2S/(Ag_2S,Se)/ZnS$ with improved PLQY and chemical stability. The ZnS shell growing step is found to not only increase the PLQY but to ease the ligand exchange allowing a wide range of chemical species to decorate their surface, including biomolecules.

Chapter 4. Preparation of multifunctional composites based on SPIONS and Ag_2S-based NPS

4.1. Introduction

As previously discussed in Chapter 1, the applications of diverse NPs for magnetic or optical hyperthermia have appeared in the last 20 years as an appealing methodology for the treatment of different tumors.[146] This is due to the possibility to target and selectively influence in a controlled way, cancerous cells, avoiding secondary effects in healthy tissues. However, temperature measurements during these treatments are accompanied by large uncertainties due to the absence of local temperature measurements. Temperature measurements are commonly acquired by means of a thermographic camera that reads the skin (surface) temperature. This reading has been proven not to be accurate in the case of injections at different depths due to the heat diffusivity of the tissues, which generates a temperature difference between outer and inner locations.[147, 148] These temperature discrepancies have negative consequences in hyperthermia treatments, since applying inappropriate temperatures may unnecessarily damage healthy surrounding cells and tissues.[149] Thus, magnetic hyperthermia treatments relies on accurate control of the heat dose supplied by magnetic NPs leading to a local temperature enhancement and must therefore be ideally combined with careful local temperature monitoring. Due to the size, colloidal stability and thermal sensitivity of Ag_2S-based NPs (as exposed in previous chapters), these NPs are an ideal system to this aim.

The NPs widely used as nanoheaters in magnetic or optical hyperthermia are SPIONS which can be heated using either an alternate magnetic field or laser radiation due to their superparamagnetism and high light absorption from the visible to the NIR-I with the great advantage of their negligible toxicity. A close contact between the heat generator and the thermometer is desirable in order to maximize the reliability of the measurement since the PL from "colder" areas would blur the response from the real "hot" areas near the heater. Previously, the encapsulation of different kinds of functional NPs has been carried out using SiO_2,[27, 63, 150-154] biocompatible polymers[102, 155-157] or phospholipids.[65, 158-162] The growth of silica spheres by sol-gel is a well-established procedure based on the hydrolysis and condensation of a Si precursor, (mainly tetraethyl orthosilicate, TEOS), in alcoholic media, and catalyzed by ammonia (this procedure is known as the Stöber-Fink-Born method).[163] This approach is not very common to encapsulate semiconductor NPs if monodispersed systems below 100 nm are pursued, due to the final size of the SiO_2 sols, typically larger than this size. Instead, the

principal strategy for the silica coating of NPs is through a water-in-oil (w/o) microemulsion process, which assures the encapsulation of individual NPs or small clusters.[27] By means of this approach, microdroplets of water are stabilized in a non-miscible organic solvent (hexane, cyclohexane, isooctane…) using a (typically) nonionic surfactant. One of the accepted mechanisms of the NPs encapsulation involves the exchange of initial ligands by the non-ionic surfactant, facilitating the introduction of the NPs in the water microdroplets. The SiO_2 sphere is then obtained through the hydrolysis and condensation of TEOS in the presence of a catalyst, (ammonia, as in the case of the Stöber method). This process is illustrated in Figure 4.1.

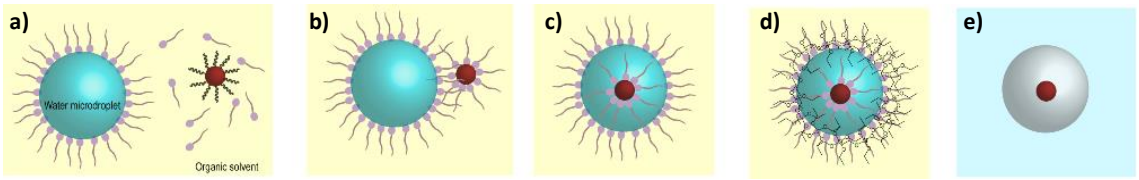

Figure 4.1. The most popular SiO_2 encapsulation mechanism of a hydrophobic NPs based on the water-in-oil reverse microemulsion:

Another well-studied approach to encapsulate NPs includes the use of PEG-modified phospholipids. These chemical species can be used for the formation of liposomes, which consist on sphere capsules that are formed by a bilayer (or a stack of bilayers) of amphiphilic phospholipids. Liposomes have been used to reduce secondary effects of some drugs, for specific drug delivery or as MRI probe carriers.[164] Their use for the encapsulation of different kinds of NPs was first reported by Dubertret et al. in 2002.[65] These nanostructures are optimal for their use in biological applications due their biocompatibility and their high interaction with cell membranes allowing for their easy internalization inside cells. For the formation of these kind of nanostructures there are different approaches, being the film hydration method the most used due to its simplicity. In this approach, the phospholipid is dissolved in an organic solvent (e.g. Chloroform) which is afterwards evaporated. On the remaining film on the bottom of the recipient containing the phospholipid is then added water. When the phospholipid molecules are in contact with water they start bending until they form the micelles. In this approach, the NPs are added in chloroform solution or as an aqueous solution in the final hydration step.

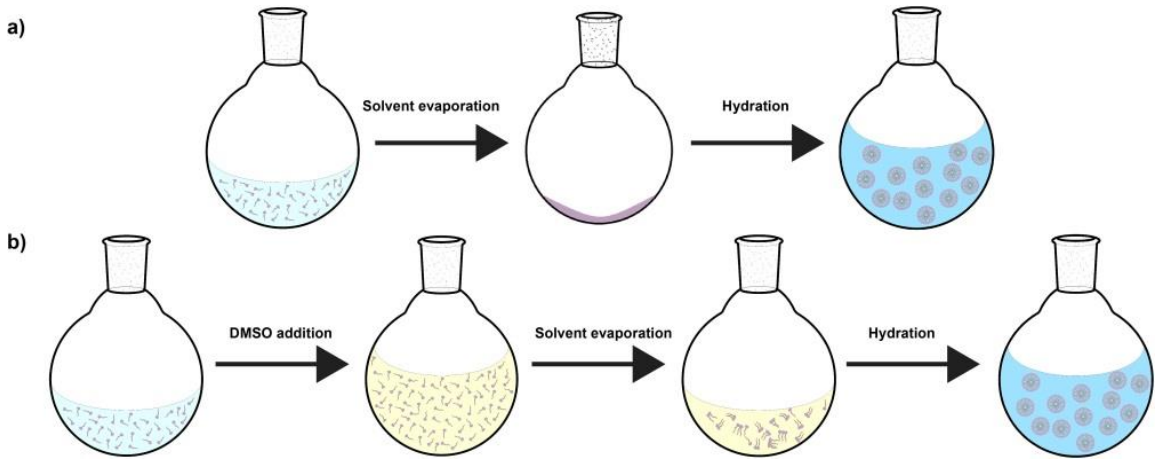

Figure 4.2. a) Film hydration method and b) Solvent exchange method for the loading of NPs inside liposomes

Another popular approach for the encapsulation of NPs is the solvent exchange method. In this case, a solvent of an intermediate polarity and miscible with the organic and the polar solvent (e.g. DMSO) is used. After the addition of the intermediate solvent, the organic solvent is evaporated remaining a stable solution of the NPs covered with the phospholipid. The final step involves the hydration in the presence of the DMSO. In this case, the micelles are formed in this DMSO:water mixture. In the final step, the DMSO is washed off by centrifugation. This last method has been successfully used for the synthesis of hydrophilic micelle containing SPIONs. There are a variety of other different methods for the formation of liposomes however, in this Chapter only the SiO_2 encapsulation and the solvent exchange method will be discussed.

The main objective of this Chapter is the preparation of all-in-one multifunctional composites containing SPIONS and Ag_2S NPs that fulfill the requirements to be used in hyperthermia treatments. The composites contain SPIONs capable to act as a nanoheaters, and Ag_2S NPs that can be simultaneously be used for NIR imaging and luminescent nanothermometry.

4.2. Results and discussion

4.2.1. Encapsulation in SiO_2

Even though the encapsulation of SPIONs using the w/o microemulsion method have been described by several groups, this route does not yield a successful coating of the here studied Ag_2S-based NPs. The formation of metallic silver observed after the addition of the ammonia solution points out that the reason may be the high reactivity of Ag to form metal-ammine complexes, such as $[Ag(NH_3)_2]^+$. Several recipes were then developed in order to avoid its presence. Among them, it is worth nothing a procedure in with the NPs were first transferred from chloroform to water using dodecyltrimethylammonium bromide (DTAB). This ionic

surfactant forms micelles when it is in contact with water due to its amphiphilic nature interacting with the NPs by its apolar tails and encapsulating them. This way, through sonication, little aggregates of water dispersible NPs are stabilized in aqueous media inside the DTAB micelles. After that, a Si precursor (TEOS) was added at room temperature and in constant agitation. The correct encapsulation of the NPs was achieved without the addition of a base (although at longer reaction times that in classic microemulsion or Stöber procedures).

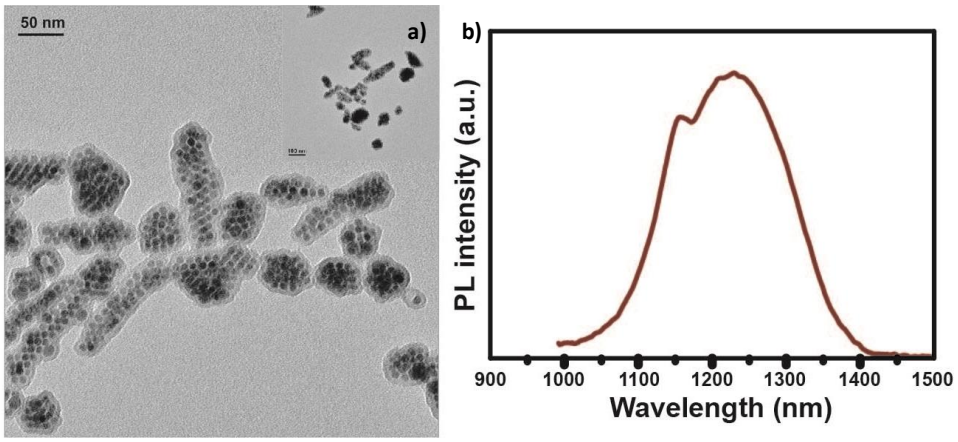

Figure 4.3.a) TEM image of the SiO_2 aggregates of $Ag_2S/Ag_2(S,Se)$ NPs. b) PL of the silica-coated NPs

The absence of catalyst allows for the slow condensation of the TEOS molecules around the surface of the DTAB micelles encapsulating the Ag_2S NPs. As can be seen in Figure 4.3a, the correct encapsulation of little (100-250 nm) groups of NPs was achieved inside silica capsules of a thickness of less than 10 nm. It should be noted that this encapsulation does not quench the NIR PL of the NPs, therefore allowing for their use as NIR emitters (Figure 4.3b). Given the ability of this method to form small groups of Ag_2S-based NPs, it was explored to obtain the multifunctional composite. By adding the SPIONs at the first step of the encapsulation procedure (as chloroform dispersion before the emulsion formation), the encapsulation of both NPs was achieved as can be observed in Figure 4.4. However, due to their different surface chemistry the sample presents groups of only SPIONs, only Ag_2S-based NPs and some that contain both species in an uncontrolled fashion. Thus, although successful SiO_2 encapsulation maintaining the initial PL and superparamagnetic properties these non-homogeneous composites lack from a close contact between the heater (SPION) and the nanothermometer (Ag_2S-based NPs), which is essential to obtain reliable temperature measurements in hyperthermia experiments.

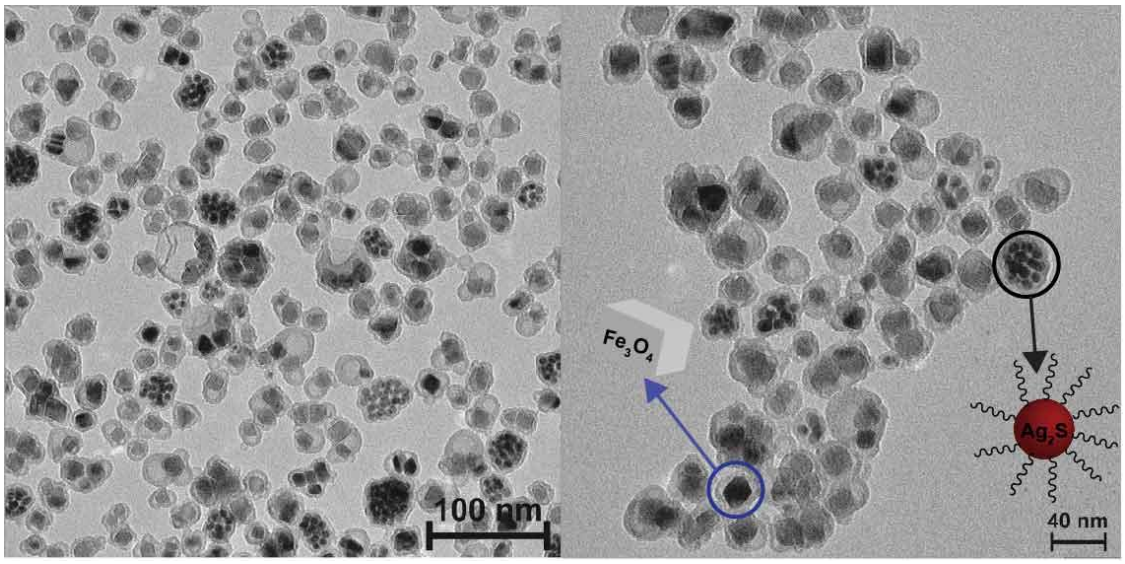

Figure 4.4. TEM images of the attempt for the encapsulation of both NPs

4.2.2. Encapsulation in phospholipidic micelles

The applications of phospholipids in several fields and the possibility of using them as encapsulating agents for NPs motivated their use for the preparation of the multifunctional composites. Among all of them, we chose 1,2-dipalmitoyl-sn-glycero-3-phosphoethanolamine-N-[methoxy(polyethyleneglycol)-2000] (ammonium salt) (PE:PEG2000) due to its proven efficiency in the coating of QDs.[65] As discussed in the Introduction, two different methods were followed to achieve the encapsulation although in this chapter only the results of the solvent exchange method will be discussed (results of the encapsulation using the film hydration method can be found in Section 4.6. of APPENDIXI). A higher degree of interaction between the phospholipid molecules and the NPs was achieved by means of this method. To encapsulate the Ag_2S-based NPs first, the NPs were thoroughly washed to remove as many hydrophobic ligands as possible. It was also observed, that a slight functionalization prior to the encapsulation was found to be necessary for the correct formation of the coated NPs due to the low affinity of the PE:PEG2000 to the NPs' surface. Otherwise, big amorphous micelles (>500 nm) were formed with some NPs inside and some outside (not shown). This intermediate functionalization was achieved through the incubation of the NPs with a small amount of PEG-SH whose long tails interact more easily with the phospholipid than the native ligands. This intermediate step favors the correct encapsulation.

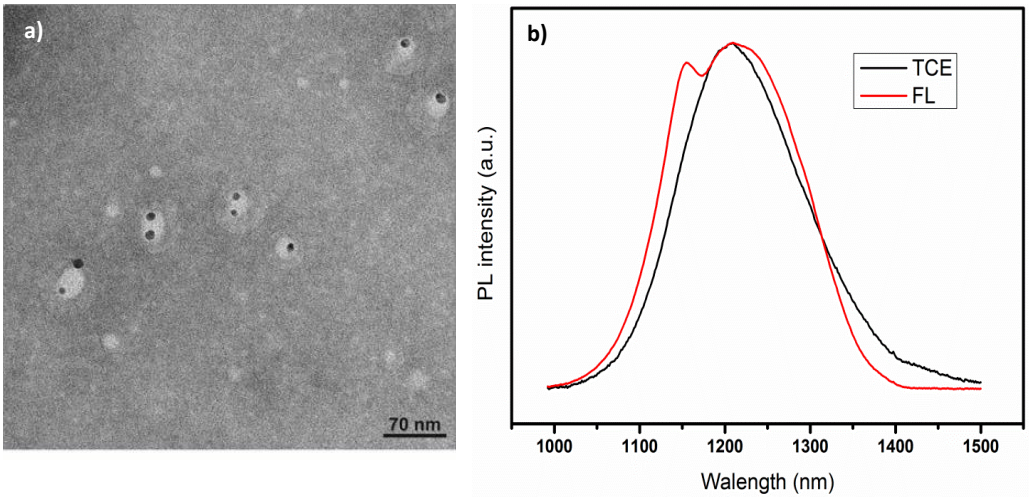

Figure 4.5. a,b) TEM images of the PE:PEG2000 micelles containing the Ag_2S-based NPs and c) NIR PL of the NPs before and after the encapsulation

TEM images of the NPs inside the micelles after this intermediate step are presented on Figure 4.5a. In order to observe the micelle coating, a dyeing step is necessary during the TEM grid preparation. In our case, the dye was a water solution of phosphotungstic acid (PTA) at 1% wt. As shown the use of the PEG-SH as surface functionalizer leads to the formation of small lipids containing small groups of NPs. Importantly, the encapsulation does not quench their NIR PL observing a PL spectrum like the one in the previously described hydrophilic NPs from Chapter 2 and 3 (Figure 4.5b). For the final encapsulation of both kinds of NPs, SPIONS and Ag_2S, no other ligand was further needed. Both NPs were dispersed in chloroform and subjected to the previously developed solvent exchange method, which is exemplified in Figure 4.6, and thoroughly described in Section 4.7 of APPENDIX I.

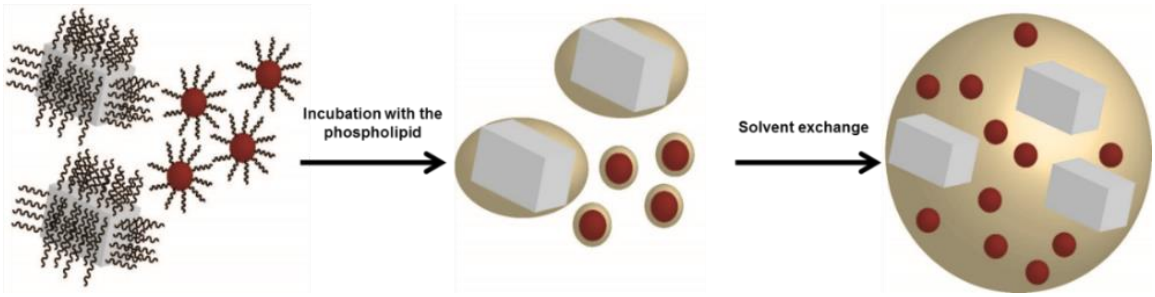

Figure 4.6. Solvent exchange method used for the encapsulation of both Ag_2S-based NPs and MNPS

The encapsulated system can be observed in Figure 4.7. In order to confirm the internalization of the NPs inside the micelle the TEM grids were stained using PTA 1% wt. Using this dye, the bilayer can be observed with white contrast. Unlike the micelles synthesized using the film hydration method, in this sample it can be clearly observed that the NPs are mainly located in

the center of the sphere. The integration of both kinds of NPs inside the phospholipidic micelles is further confirmed by a simple macroscopic experiment in which a magnet is placed near a cuvette containing a water dispersion of the composites. It can be clearly observed on Figure 4.7c,d how from the starting dispersion not only the MNPs are attracted to the magnet, but also the Ag_2S-based NPs as evidenced by the strong NIR PL observed near the magnet, as compared with the one in the rest of the dispersion. The rest of the NIR emission may come from bigger aggregates that have a smaller drag coefficient or encapsulates of only Ag_2S-based NPs. The optical image was taken with an InGaAs camera belonging to the FIG group at UAM by Yingli Shen.

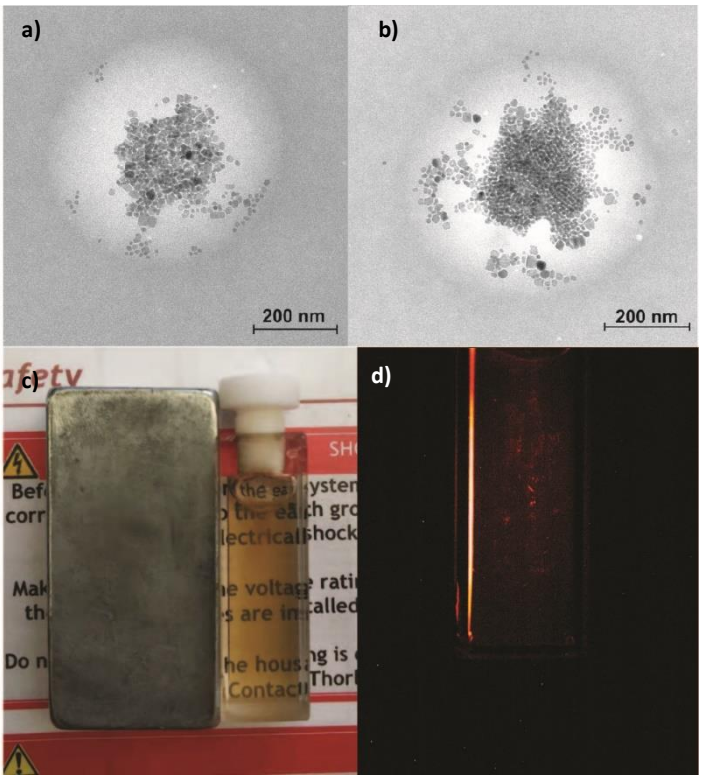

Figure 4.7. a-d) TEM images of the as-synthesized multifunctional nanocomposites containing Ag_2S-based NPs and SPIONS inside the PE:PEG2000 micelles c) Day light and d) IR image of the nanocomposite solution when a strong magnet is applied at a side of the cuvette. The SPIONS are attracted to the magnet transporting as well the Ag_2S-based NPs

The magnetic and optical properties of the composite were measured to check whether the encapsulation process produces modifications on the properties of the starting NPs. Concerning the optical properties of the semiconductor NPs, the Ag_2S-based NPs still show their bright PL upon encapsulation at the same wavelength, as shown in Figure 4.12.a, which depicts the absorption and PL response of the micelles. The PL lineshape reminds that previously shown in Chapter 2 for NPs in aqueous media, because of water absorption. Figure 4.12.b shows the AC measurements of the specific absorption rate (SAR), which is an indicative

of how efficient are the SPIONS transforming magnetic energy into heat. The average of 3 measurements for the micelles gave a result of 104 W/g at 24 kA/m and 105 kHz, a slight decrease from the starting NPs (140 W/g at those same conditions). This reduction could be a result of the aggregation of the MNPs that hinders the free move of the MNPs. Since the heat generation essentially comes from the field driven movement, the aggregation of the MNPs is a critical parameter driving their heating capacity.[165] If their move is obstructed, the heat generation may be less efficient.

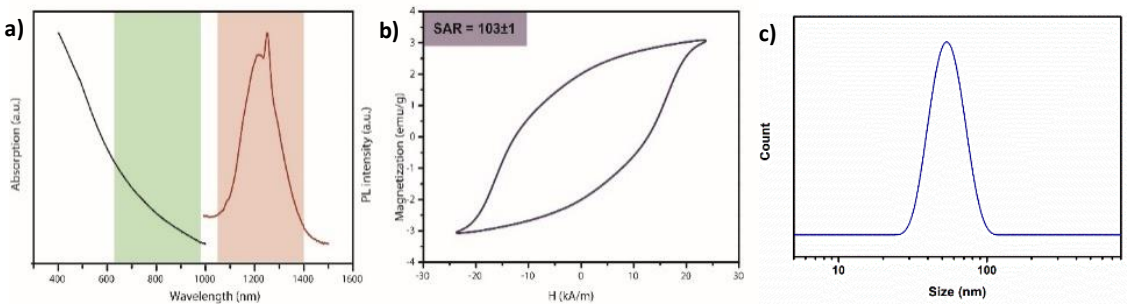

Figure 4.12. a) Optical properties of the nanocomposite and b) Magnetic behavior of the composite and c) DLS spectrum of one sample of the nanocomposite

The size of the micelles measured by TEM images is between 200-500 nm. However, soft polymeric spheres are known to deform when deposited on surfaces due to interface interactions, what may alter the real size. For this reason, DLS experiments were carried out to confirm their size in solution.

Surprisingly, as observed in Figure 4.12.c, the main hydrodynamic size of the as-synthesized structures in solution is below 100 nm, suggesting that the TEM images are not reliable when measuring the size of these capsules. Indeed, samples in a TEM have been previously dehydrated, (in vacuum), what makes soft colloids to appear as bigger flat “pump-cakes”.

The mild encapsulation procedure not only preserves the NIR PL and magnetic properties of the NPs but it also maintains unaffected the thermal sensitivity in the NIR range previously studied, as depicted in Figure 4.10, where the integrated emission intensity of the nanocomposite with temperature is plotted. According to equation 2.X (Chapter 2), the thermal sensitivity is 3%·$^{\circ}C^{-1}$ at room temperature.

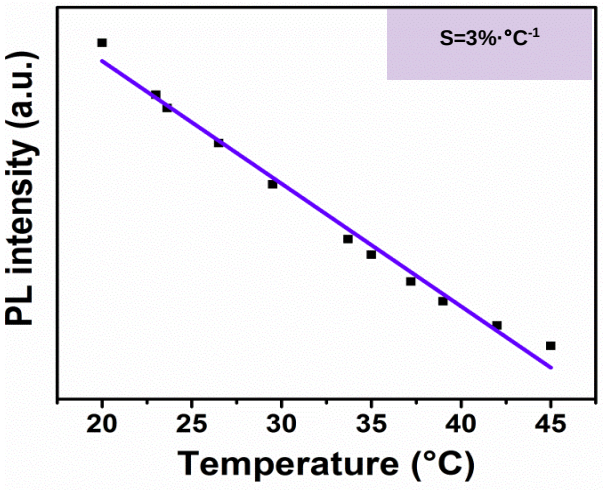

Figure 4.10. Calibration of the integrated emission intensity of the nanocomposite with temperature

Therefore, the as-synthesized composites can be successfully used to activate local temperature changes induced by the optical or magnetic excitation of the NPs, NIR imaging, and temperature reading with a sensitivity as high as 3%·°C^{-1}.

4.2.2.1. Cell internalization studies

Liposomes are made of phospholipids with a similar structure of those forming cell membranes. They are widely used in several biological applications, including cell culture studies. In order to test if our nanocomposite could be easily internalized by tumorous cells a dispersion of the composite was incubated at different concentrations in the cell culture of MCF-7 cells (breast cancer cells). The results are shown in Figure 4.11. This experiment was performed by Dra. Ana Espinosa, from IMDEA Nanoscience.

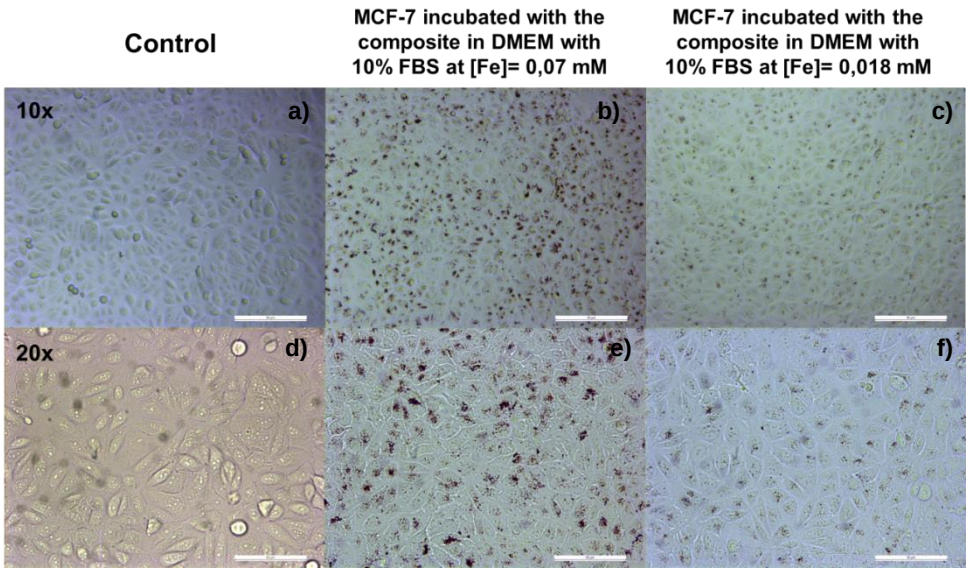

Figure 4.11. Cell internalization studies using MCF-7 cells with different concentrations of the nanocomposite.

The images on the left (a,d) correspond to control images at different magnifications (10x and 20x, respectively) of the cells where no composites have been incubated. Images at different magnifications in the middle (b,e) and on the right (c,f) correspond to cells incubated with the composite at an Iron concentration of 0.07mM (b,e) and 0.018 mM (c,f) (obtained by ICP-OES analysis). The images show high density of black spots, which are related to the presence of the composites in the cells (due to the high dielectric constant of iron oxide) which are located out of the nucleus. Further studies to confirm low cytotoxicity are in progress.

4.3. Conclusions and future work

The encapsulation of different nanomaterials is a powerful tool to obtain multifunctional nanocomposites that could be used as all-in-one theranostics agents. In this Chapter, a multifunctional nanocomposite was synthesized joining the attractive superparamagnetic properties of iron oxide NPs and the thermometric properties of Ag_2S-based NPs. This composite can be used as an optical/magnetic probe and at the same time as a thermometer that will provide temperature reading at the same spot in which the hyperthermia treatment is being applied. Furthermore, this nanocomposite is a potential tool for bioimaging in two different techniques. Since iron oxide NPs are active for MRI and the Ag_2S-based NPs can be used for fluorescence or photoacoustic imaging with high penetration, both imaging techniques could be simultaneously used for the acquisition of images. Furthermore, first studies suggest good cell internalization in the cell line MCF-7. This work set the basis to further confirm the viability of these composites for simultaneous heat release and temperature control in cancer cells.

General conclusions

- Ag_2S NPs are optimum systems for fluorescence-based biological applications due to their photoluminescence response centered in the NIR-II. In this thesis, a new application for these NPs has been developed, namely, their use as high-sensitivity luminescence nanothermometers. The strong dependence of their photoluminescence spectral position, intensity and lifetime with temperature allow for temperature measurement with high sensitivity. Their performance as nanothermomethers has been explored both in *ex vivo* and *in vivo* experiments, with outstanding results.
- The dense surface coating and aggregation observed in heat-up synthesized Ag_2S NPs have been identified to be caused by an unreacted intermediate during the synthesis. A new synthetic route is proposed that avoids this surface coating, allowing higher yield in ligand exchange procedures and the possibility to carry out post-synthetic treatments. These treatments include passivation with selenium or the growth of different number of outer layers of ZnS to produce a type I core/shell structure with improved photoluminescence quantum yield and with a more versatile surface chemistry.

- The encapsulation of Ag_2S-based NPs and Fe_3O_4 NPs (SPIONs) inside micelles formed by a PEG-modified phospholipid is found to retain the heating ability of the SPIONs and the photoluminescence response of the Ag_2S-based NPs. Incipient cell culture studies suggest their correct internalization in cells, opening the door for simultaneous heating and temperature control in cancer cells.

Conclusiones generales

- Las NPs de Ag_2S son sistemas óptimos para aplicaciones biológicas basadas en fluorescencia debido a su fotoluminiscencia centrada en el rango NIR-II. En esta tesis, una nueva aplicación para estas NPs ha sido desarrollada: su uso como nanotermómetros. La fuerte dependencia de la posición espectral de su emisión, la intensidad y el tiempo de vida con la temperatura permite la medición de temperatura con alta sensibilidad. Su uso como nanotermómetros ha sido descrito en experimentos tanto *ex vivo* como *in vivo* con muy buenos resultados.
- La causa de la agregación y alta densidad de ligandos en superficie observada en las NPs sintetizadas por el método "heat-up" ha sido identificada como la formación de un intermedio en la síntesis. Una nueva ruta ha sido desarrollada para evitar este fuerte recubrimiento, aumentando el rendimiento de las reacciones de cambio de ligando y permitiendo tratamientos después de la síntesis sobre las NPs. Estos tratamientos incluyen la pasivación con seleniuro de plata y el crecimiento de diferente número de capas de ZnS para producir estructuras "core/shell" de tipo I, que permiten obtener NPs con un mayor rendimiento cuántico y una química de superficie más versátil.
- La encapsulación de las NPs basadas en Ag_2S junto con NPs de Fe_3O_4 dentro de micelas de un fosfolípido modificado con un extremo de polietilenglicol retiene la capacidad de generar calor de las NPs mágneticas y las propiedades fotoluminiscentes de las NPs basadas en Ag_2S. Los primeros estudios en células sugieren que estas estructuras se internalizan bien abriendo la puerta la observación de terapias de hipertermia con un control de la temperatura en tiempo real.

APPENDIX I: Experimental section

Chapter 2

2.1. Chemicals

Silver (I) diethyldithiocarbamate (AgDDTC, 99%), 1-dodecanethiol (DT, >98%), toluene (TOL, 99.8%), 1-octadecene (ODE, 90%), acetone (technical grade), oleylamine (OLA, 70%), polyethylene glycol methyl ether thiol (PEG-SH, average Mn 6000), chloroform ($CHCl_3$, >99.8%), tetrachloroethylene (TCE, >99%) and ethanol (EtOH, 96%). All chemicals were used without further purification

2.2. Synthesis of Ag2S nanocrystals

In this work the synthesis of Ag_2S NCs is based on a previously reported thermal decomposition of AgDDTC in DDT with slight variations.[62] The syntheses have been performed in standard Schlenk lines using a temperature controller connected to a PC unit for accurate temperature programming, which provides reproducible results for each batch. On each synthesis, 0.05 mmol of silver (I) diethyldithiocarbamate, 12.5 mmol of 1-dodecanethiol, and 9 mmol of 1-octadecene were mixed in a three-neck round bottom flask and degassed under vacuum at room temperature. The flask is then backfilled with nitrogen and heated up to 200°C at a rate of 17°C/min. The solution is stirred for one hour at 200°C and then cooled down to room temperature using a room temperature water bath. After the synthesis, the black colloidal dispersion is washed in several cycles of precipitation with ethanol and re-dispersion in toluene.

2.3. Thin films fabrication

The thin film used for the thermometry studies was fabricated by a simple room temperature spin coating procedure on a polyethylene terephthalate flexible substrate. The thin film used for TAS measurement described in Figure 2.5 of the thesis was prepared by drop casting of a NCs suspension on a quartz substrate.

2.4. Ligand exchange

In order to obtain bright Ag_2S NPs samples in water, an entire batch of NPs was sonicated during 90 min in the presence of 100 mg of PEG-SH. Afterwards; it was left in a mechanical agitator for another hour. The sediment portion (which did not exchange the native ligands) was removed by centrifugation and the stable portion was dried using a N_2 flow. After that, the deposit was dispersed in ethanol and was filtered to remove the excess of PEG-SH. Finally, the ethanol was blown away to disperse the NPs in water.

2.5. Characterization

2.5.1. Basic optical characterization

Steady-state NIR to UV optical absorption measurements were carried out in solution using a Varian Spectrophotometer (Cary 5000) UV-Vis-NIR. Photoluminiscence spectra in solution were recorded in a spectrofluorometer (Fluorolog TCSPC Horiba Jobin Yvon) equipped with an InGaAs NIR detector (Horiba Symphony II). Thin film NIR emission spectra at different temperatures and depths were recorded using an InGaAs CCD camera (Andor iDus DU490A). The sample was optically excited with an 800 nm fiber-coupled laser diode (Lumics) focused by a long working distance microscope objective and the emission was spectrally analyzed by an Andor Shamrock 193i spectrometer after passing through appropriate filters to remove the pump background.

2.5.2. HREM characterization

Samples were characterized by High Angle Annular Dark Field Scanning Transmission Electron Microscopy (HAADF-STEM) using a JEOL-2010F microscope operated at 200 kV. HAADF-STEM images were recorded using a 0.5 nm electron probe at a camera length of 10 cm.

A FEI Titan3 Themis 60-300 microscope was used to acquire High Resolution Transmission Electron Microscopy (HRTEM) images at 80kV to minimize beam damage. The monochromator was excited in these experiments in order to minimize the effect of the chromatic aberration. Afterward, using the Zemlin tableau, the defocus and the third-order aberration coefficients of the objective lens were measured and adequately compensated. Additionally, very high spatial resolution X-EDS maps were acquired using the ChemiSTEM capabilities of the FEI Titan3 Themis 60–300 microscope working in scanning transmission electron microscopy mode at 80 kV. In this case, a high brightness, sub-angstrom diameter, electron probe was combined with a highly stable stage to record these maps. Maps were acquired with a beam current of 150 pA and a pixel dwell time of 128 □s.

This dwell time ends up in a frame acquisition time of approximately 30 s after which the drift was corrected using cross correlation. A 5 pixels smooth filter was used on the images as provided in the Esprit software. The X-EDS quantification was carried out using the K factor of Sulfur K line and Silver L line transitions provided by the Bruker Esprit 1.94 software.

2.5.3. Transient Absorption Spectroscopy

Transient Absorption Spectroscopy (TAS) was carried out with a femtosecond Clark-MXR CPA210 regenerative amplifier delivering 120 fs pulses at 775 nm and 1 KHz repetition rate. The primary beam was splitted into pump and probe beams. The pump beam was sent to a computer-controlled delay line to anticipate it respect to the probe and finally focused onto the sample (1 mJ cm-2). The probe beam was focused on a sapphire plate to generate a supercontinuum pulse and then spatially overlapped with the pump on the sample. The transmitted probe beam was sent to a prism spectrometer (Entwicklungsburo Stressing) and detected with a linear CCD array (VIS-Enhanced InGaAs Hamamatsu Photonics). A software synchronized the delay line with the acquisition system and recorded spectra at single shot. Measurements were performed with pump and probe beams polarized at magic angle.

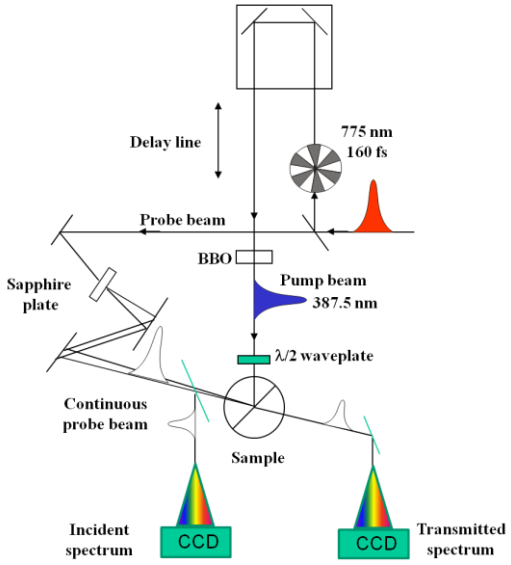

Figure 1. TAS experimental setup

Section 2.5.4. Determination of the PLQY

Fluorescence spectra were obtained using a calibrated spectrofluorimeter (Edinburgh Instruments, FLS920), with a xenon lamp as excitation source, an integrating sphere (Jobin-Yvon), and a liquid nitrogen cooled NIR photo-multiplier tube (Hamamatsu, R5509-72). The monochromator was centered at a wavelength of 822 nm. The excitation bandwidth was 15 nm and the emission bandwidth was 10 nm. Ultimately, the internal PLQY was measured for each sample with the absorbed photons having been calculated by subtracting the intensity of the beam after it had passed through a sample from the intensity of the beam when no sample was present.

2.5.5. *Ex vivo* experiment

NIR emission spectra at different temperatures and depths were recorded using an InGaAs CCD camera (Andor iDus DU490A). The sample was optically excited with an 800 nm fiber-coupled laser diode (Lumics) focused by a long working distance microscope objective and the emission was spectrally analyzed by an Andor Shamrock 193i spectrometer after passing through appropriate filters to remove the pump background. A temperature-controlled stage (Linkam PE120) was used for calibrating the emission with temperature.

Section 2.5.6. Time resolved spectroscopy

The luminescence generated by the solution was recorded using the Fluorimeter NanoLog™ (HORIBA) with double-grating excitation and two emission monochromators. The software used in this case was the Fluorescence. The detector used was a liquid-N2 cooled R5509-73 photomultiplier tube, operating in the 300–1700 nm range. Luminescence decay curves were obtained by exciting the colloidal suspensions of Ag2S NCs by using a pulsed diode laser (HORIBA, model DeltaDiode DD-450L) operating at 450 ± 10 nm and providing pulses of 80 ps duration with a maximum repetition rate of 100 MHz. The fluorescence time decay curve was finally obtained with time-domain TCSPC using the Datastation software.

Section 2.5.7. NIR-II imaging setup in the *in vivo* experiment

For imaging experiments, the anesthetized mouse was placed in an optical setup specially designed for NIR fluorescence imaging. Optical excitation is achieved with an 808 nm fibercoupled laser diode (LIMO) operating in pulsed mode (pulse width: 100 ms; pulse period: 500 ms). The laser power during the ON cycles was set to 100 mW. The laser beam was collimated using a F220-SMA collimator (Thorlabs) and its vertical position was adjusted so that the spot diameter at the mice skin surface was 0.5 cm. The NIR fluorescence images were acquired by an InGaAs camera (Xeva 17 from Xenics INC), sensitive in the 900-1700 nm range, operating synchronized with the excitation laser. The array size of the detector in this camera is 320x256 pixels. The images were focused on the detector array by means of a 35 mm lens designed for NIR wavelengths (Optica Kowa LM35HC-SW). The distance between the lens and the mouse was approximately 25 cm, so that the lateral resolution of our images was in the order of 300 µm. An 850 nm longpass filter was used to eliminate any possible scattered laser radiation from the images. The signal was further filtered by a 1200 nm long pass filter to avoid any autofluorescence-related background noise.

Chapter 3

3.1. Chemicals

Silver (I) diethyldithiocarbamate (AgDDTC, 99%), 1-dodecanethiol (DT, >98%), toluene (TOL, 99.8%), acetone (technical grade), oleylamine (OLA, 70%), sulfur powder (S, synthesis grade), polyethylene glycol methyl ether thiol (PEG-SH, average Mn 6000), chloroform ($CHCl_3$, >99.8%), tetrachloroethylene (TCE, >99%), trioctylamine (TOA, 98%), silver (I) nitrate ($AgNO_3$, >99.0%), acetonitrile (99.8%), deuterated chloroform ($CDCl_3$, 99.8% D), deuterium oxide (D_2O, 99.9 atom % D), toluene-d_8 (99.6 atom % D), hexane (reagent grade), ethanol (EtOH, 96%), selenium powder (Se, 99.99%), trioctylphosphine (TOP, 97%), oleic acid (OA, technical grade 90%), Zinc acetate dihydrate ($Zn(Ac)_2{\cdot}2H_2O$), methoxypolyethylene glycol amine (PEG-NH_2), poly(ethylene glicol) bis(amine) (NH_2-PEG-NH_2), poleyvinylpirrolidone (PVP, W_t= 50000 Da) . All chemicals were used without further purification.

3.2. Synthesis of Ag_2S NCs by hot injection

In this case, 0.2 mmol of AgDDTC, 60 mmol of DT and 10 ml of toluene were mixed in a three neck round bottom flask. The mixture was heated to 100°C and when the silver salt is completely dissolved and the solution turns to a bright yellow color 100 μL of a solution of 0.4 mmol of sulfur powder in 1 ml of OLA is swiftly injected. The solution is then left to react until it is quenched using a water bath. The content is passed to a plastic centrifuge tube and precipitated with acetone.

These NCs were found to be very stable in the reaction media, so several cycles of centrifugation at 9000 rpm and cooling of the centrifuge tube were necessary to precipitate all the NCs. The addition of ethanol has a positive influence in the destabilization of the NCs but it was also found to irrevocably quench the NCs PL almost completely. Typically, the washing steps were carried out using the same amount of acetone as the reaction media and a few drops of ethanol if the NCs were too stable to precipitate.

3.3. Syntheses of Ag_2S/Ag_2(S,Se) NCs

For the synthesis of these NCs 0.2 mmol of AgDDTC, 60 mmol of DT and 10 ml of toluene were mixed in a three neck round bottom flask. The mixture was heated to 100°C and when the silver salt is completely dissolved and the solution turns to a bright yellow color 100 L of a solution of 0.4 mmol of sulfur powder in 1 ml of OLA is swiftly injected.

After 5 minutes 100 μL of a 1 M solution of Se powder in TOP is injected into the NCs dispersion. The solution is left to react for 10 minutes and then, it is left to naturally cool to room temperature. The washing steps were carried out with acetone and chloroform.

3.4. Ligand exchange reactions

All batches are dispersed in 10 ml of chloroform and from that solution, 1 ml of NCs ($[Ag^+] \cong 1.5$ mg/ml) is added to a 5 ml chloroform solution containing 100 mg of PEG-SH. The mixture is sonicated at room temperature for half an hour and then is left in a mechanical agitator for 1.5 h. After that, the chloroform is blown dry using a N_2 flow and 5-10 ml of ethanol is added to the NCs deposit. The solution is vortexed and sonicated until an optically clear dispersion is obtained. In order to remove the excess polymer two centrifugation steps were followed with ethanol using Sartorius Vivaspin 20 MWCO= 100 KDa ultracentrifugation tubes. After that, three cycles of centrifugation and redispersion in water were found to be enough to eliminate the ethanol and the remaining polymer. The NCs obtained using this method were stable in the water dispersion for months in storage at 4°C.

In order to compare the behavior of the two kinds of NCs in ligands exchange reactions, aliquots with the same quantity of Ag^+ (measured by ICP-MS) where subjected to the above procedure. The amount of NCs transferred to water where measured as the quantity of Ag+ detected in the water samples measured using ICP-MS.

3.5. Isolation of the intermediate silver compound

In order to isolate the chemical compound that undergoes the decomposition to Ag_2S a mixture of 0.2 mmol of AgDDTC, 60 mmol of DT and 10 ml of toluene is heated to 100°C in a three neck round bottom flask. When the silver salt is completely dissolved and the reaction media presents a bright yellow color the reaction is quenched using a water bath. Upon cooling, the reaction starts to present turbidity and a darker color, due a partial decomposition of the precursor. The white solid is isolated from the reddish liquid by centrifugation and washed with hexane.

3.6. Synthesis of silver (I) dodecanethiolate

The synthesis of the silver polymer was carried out based on a previously reported procedure.[133] A solution of 1 mmol of $AgNO_3$ in 5 ml of acetonitrile is slowly injected into a solution of 2 mmol of 1-dodecanethiol and 2 mmol of trioctylamine in 10 ml of acetonitrile.

The $AgSC_{12}H_{25}$ is formed immediately upon the injection of the silver solution. The white powder is washed by centrifugation in hexane to eliminate the excess products and dried using an oven at 50°C.

3.7. Calculation of the hydrodynamic size through DOSY

The calculation of the hydrodynamic size using the diffusion coefficient value obtaining by DOSY can be carried out using the Stokes-Einstein equation.

$$d_H = \frac{k_B T}{3\pi\eta D}$$

Where k_B is the Boltzmann constant, T is the temperature at which the spectrum has been recorded; η is the solvent density and D the diffusion coefficient given by DOSY

3.8. Synchrotron measurements

X-ray absorption spectroscopy (XAS) experiments were performed at the SXS (S K- and Ag L_3-edges) and XAFS2 (Se K-edge) beamlines at the LNLS (Laboratório Nacional de Luz Síncrotron), Campinas, Brazil. X-ray Absorption Near Edge Structure (XANES) spectroscopy measurements at the S K-edge (2472 eV) and Ag L_3-edge (3351 eV) were carried out using a InSb(111) double-crystal monochromator, giving an energy resolution of 2 eV at the S K-edge, and 1 eV at the Ag L_3-edge. Experiments with soft X-rays were performed in a vacuum chamber at 10^{-9} mbar and room temperature (RT). The incident beam intensity (I_0) was measured using a thin foil of Al. Samples were dropped on carbon tapes to be measured in Total Electron Yield (TEY) and Fluorescence (FL) modes simultaneously. The photon energies were calibrated using a Mo and Ag metallic foil setting the first inflection point of the Mo L_3 absorption edge at 2520 eV for S, and to the Ag L_3 absorption edge (3351 eV) for Ag measurements. The final XANES spectra were obtained after background subtraction and normalization to the postedge intensity.

XANES and Extended X-ray Absorption Fine Structure (EXAFS) experiments at the Se K-edge (12658 eV) were measured at room temperature using a Si(111) single channel-cut crystal monochromator in fluorescence mode. An ionization chamber was used to detect the incident flux and a 15-element germanium solid-state detector was used to sense the fluorescence signal from the sample. The EXAFS data was extracted from the measured absorption spectra by standard methods using the ATHENA software which is part of the Demeter package.[166] The Fourier transforms were calculated using the Hanning filtering function. EXAFS modeling was carried out using the ARTEMIS program (Demeter package). Structural parameters (coordination numbers, interatomic distances and Debye–Waller factor) were obtained by

nonlinear least-squares fit of the theoretical EXAFS signal to the data in R space by Fourier Transforming both the experimental and calculated data. Theoretical scattering path amplitudes and phase shifts for all paths used on the fits and simulations were calculated using the FEFF code.[145] The passive reduction factor S_0^2 was restrained to the value of 0.72. This value was obtained fitting the EXAFS spectrum of metallic Se foil and constraining the coordination number of the first coordination shell to 2.

Sample	N_{Se-Ag}	R_{Se-Ag} (Å)	DWF_{Se-Ag} (Å^2)	N_{Se-S}	R_{Se-S} (Å)	DWF_{Se-S} (Å^2)
Ag_2S+Se NCs	2.8(4)	2.6 - 2.8	0.010(3)	1.0(4)	2.10(4)	0.06(1)
Ag_2S standard	7	2.7 - 2.9				

Table 1. Fitted structural parameters (N: average coordination number; R: interatomic distance; DWF: Debye-Waller factor) obtained from the EXAFS analysis using a two-shell model

3.9. Zn precursor calculation for the shelling reactions

The total amount of NCs obtained in the hot injection synthesis is determined to be ≅18 mg as determined by ICP-AES.

In order to calculate the quantity of Zn precursor that we need to cover the surface of all the NCs in the sample we first need to know how many NCs are in our sample.

$$m_{Ag_2S} = \frac{n_{Ag}}{2} \cdot Mw_{Ag_2S} = \frac{0.018\ g}{2} \cdot 247.8 \frac{g}{mol} = 1.10 \cdot 10^{-2}\ g_{Ag_2S}$$

Now, we need to know the mass of one NCs to obtain how many NCs are necessary to achieve that final mass. First we calculate the volume and mass of its smaller unit, the unit cell. Since the unit cell in □-Ag_2S is cubic its volume is:

$$V_{UC} = a \cdot b \cdot c = 0.423nm \cdot 0.691\ nm \cdot 0.787\ nm = 0.23\ nm^3$$

Thus, the mass of the unit cell is:

$$\rho = \frac{m}{V}; m = \rho \cdot V = 7.23 \frac{g}{cm^3} \cdot (0.23 \cdot 10^{-21}\ cm^3) = 1.66 \cdot 10^{-21} g$$

Now that we know the mass of a single unit we can calculate the total mass of NCs by calculating the number of unit cells they contain. For that we do the same calculations but for 1 NCs instead for a unit cell:

$$V_{1NC} = \frac{4}{3}\pi(4nm)^3 = 268.1\ nm^3$$

To calculate we number of unit cells in every NC:

$$n_{UC} = \frac{V_{1NC}}{V_{UC}} = \frac{268.1\ nm^3}{0.23\ nm^3} = 1165.4\ unit\ cells\ in\ every\ NC$$

Thus:

$$m_{1\ NC} = 1165.4 \cdot 1.66 \cdot 10^{-21} g = 1.93 \cdot 10^{-18} g$$

So, in order to obtain the number of NCs in the sample:

$$m_{total} = \frac{m_{Ag_2S}}{m_{1NC}} = \frac{1.10 \cdot 10^{-2} g}{1.93 \cdot 10^{-18}} = 5.7 \cdot 10^{15}\ NCs\ in\ the\ sample$$

To determine the quantity of Zn necessary to form a few monolayers over the Ag_2S NCs it is necessary to calculate the volume of the NCs and the volume of the final core/shell NCs taking into account that the minimal amount of Zn to form a layer would be a layer form by only one lattice parameter thick. So, first of all we have to calculate the volume of a single unit cell of ZnS (zinc-blende):

$$V_{UCZnS} = a \cdot b \cdot c = a^3 = 0.541^3 = 0.16\ nm^3$$

The increase in the diameter of the NCs would then be (for one layer of ZnS) the sum of one lattice parameter on every side of the NC:

$$d_{CS} = d_{Core} + 2 \cdot a_{ZnS} = 8 + 2 \cdot 0.541 = 9.1\ nm$$

$$V_{CS} = \frac{4}{3}\pi(\frac{9.1\ nm}{2})^3 = 392\ nm^3$$

$$V_{shell} = V_{CS} - V_{core} = 392\ \ nm^3 - 268\ \ nm^3 = 124\ \ nm^3$$

In order to now calculate the total mass of Zn to grow that volume:

$$n_{UCZnS} = \frac{V_{shell}}{V_{UCZnS}} = \frac{124\ \ nm^3}{0.16\ \ nm^3} = 784\ unit\ cells\ of\ ZnS$$

The number of moles necessary for the growth of that amount would be:

$$n_{ZnS} = \frac{m_{UCZnS}}{Mw_{ZnS}};\ m_{UCZnS} = \rho \cdot V_{UC} = 4\frac{g}{cm^3} \cdot (0.541 \cdot 10^{-21}\ cm^3)^3 = 6.3 \cdot \frac{10^{-22} g}{unit\ cell}$$

$$n_{ZnS} = \frac{6.3 \cdot 10^{-22}}{97.47\ g/mol} = 6.5 \cdot 10^{-24}\frac{moles}{unit\ cell}$$

So, since the salt we are going to use is for the reactions is $Zn(Ac)_2 \cdot 2H_2O$ (M_w=219.51):

$$m_{Zn(Ac)_{\cdot 2H_2O}} = 6.5 \cdot \frac{10^{-24} moles}{unit\ cell} \cdot 784\ cells \cdot 219.51\frac{g}{moles} = 1.12 \cdot 10^{-18} g/NC$$

Since that is the mass of Zn precursor needed for the coating of one NC, to cover the whole sample:

$$m_{total} = m_{NC} \cdot N_{NCs} = 1.12 \cdot 10^{-18} \cdot 5.7 \cdot \frac{10^{15} g}{NC} \cdot \frac{1\ mg}{10^{-3} g} = 6.4\ mg/layer$$

3.10. Synthesis of $Ag_2S/Ag_2(S,Se)/ ZnS$

For the shelling reaction the calculated quantity of $Zn(Ac)_2$ is placed inside a three neck round bottom flask along with 6 ml of OA and 3 ml of ODE. The mixture is then heated up to 100°C and degassed under vacuum for 1 h to eliminate all the oxygen and water in the sample. After that, the dispersion of the Ag_2S-based NCs in ODE is injected. Right after the injection, the system is degassed and the reaction is left to proceed in vacuum during 30 minutes. After that, the reaction is quenched using a water bath and the NCs are washed in successive steps of centrifugation redispersation in chloroform and acetone.

Chapter 4

4.1. Chemicals

Silver (I) diethyldithiocarbamate (AgDDTC, 99%), 1-dodecanethiol (DT, >98%), toluene (TOL, 99.8%), acetone (technical grade), oleylamine (OLA, 70%), dodecyltrimethylammonium bromide (DTAB, >98%), sulfur powder (S, synthesis grade), tetraethyl orthosilicate (TEOS, 98%), polyethylene glycol methyl ether thiol (PEG-SH, average Mn 6000), chloroform ($CHCl_3$, >99.8%), tetrachloroethylene (TCE, >99%),dimethylsulfoxide (DMSO, >99%), 1,2-dipalmitoyl-sn-glycero-3-phosphoethanolamine-N-[methoxy(polyethylene glycol)-2000] (ammonium salt) (PE:PEG2000)

4.2. Synthesis and characterization of the Ag_2S-based NCs

The Ag_2S-based NCs used in this Chapter were synthesized by the route previously discussed in Chapter 3 and described in Section 3.3. of APPENDIX I. The as-synthesized NCs have an average size of 8.5±0.9 nm an a PL spectrum centered in 1210 nm.

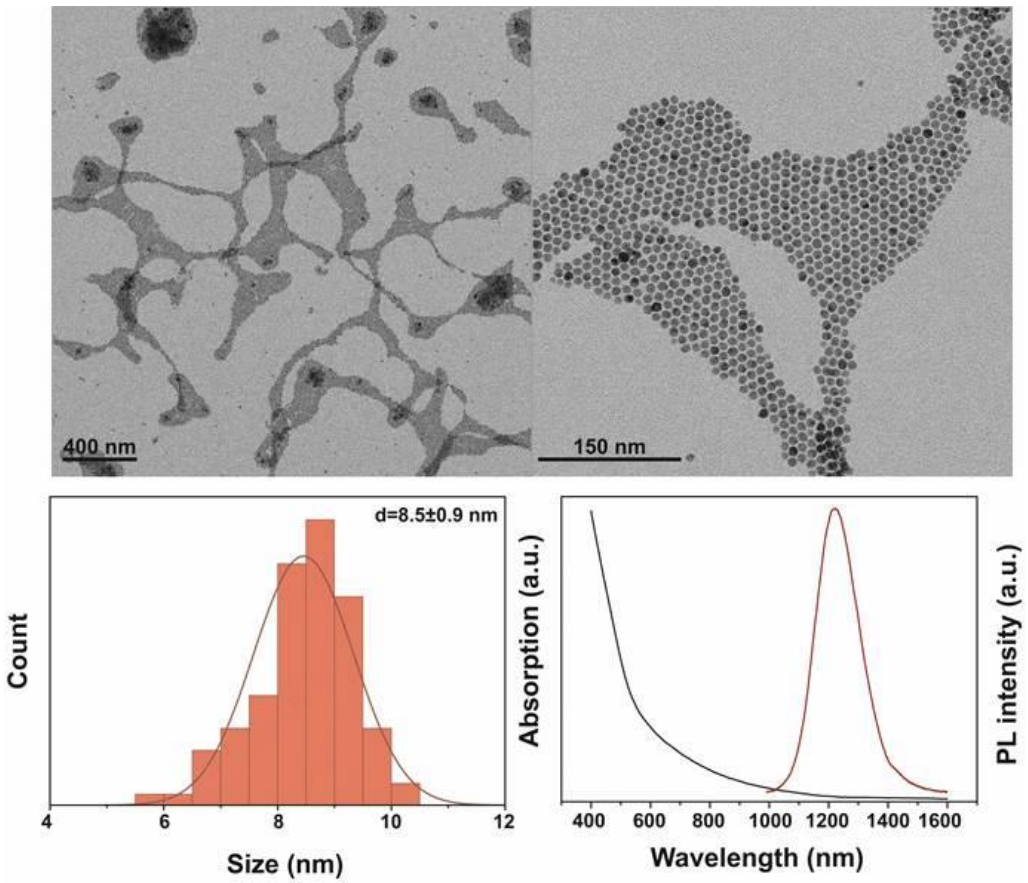

Figure 3. a) and b) TEM images of the Ag2S/Ag2(S,Se) NCs used for the encapsulation. C) Size distribution and d) room temperature PL

4.3. Synthesis and characterization of the SPIONs

Magnetite nanoparticles were synthesized by our collaborators from Dr. Gorka Salas' lab following the method reported by Sun et al.[167] using $[Fe(acac)_3]$ as metal precursors. In a typical synthesis, $[Fe(acac)_3]$ (5 mmol), oleic acid (15 mmol), oleylamine (15 mmol) and 1,2-dodecanediol (25 mmol) and 1-octadecene (50 mL) were mixed in a three-neck round-bottomed flask with mechanical stirring under a flow of nitrogen at atmospheric pressure. It was heated at a constant rate of 2°C/min until the temperature reached around 100°C and the dark solution was kept for 1 h, following with nitrogen flux cut off and then heated until 200°C with the same temperature rate. In that plateau, we maintained the temperature for 120 minutes and increased the heat until reflux (315-320°C) with a constant rate of 3°C/min. When the synthesis reached at reflux, we waited for 1 h and stopped the reaction, allowing the mixture to cool down to ambient temperature. Finally, the solution was extracted in hexane, washed by centrifugation with ethanol repeatedly and stored in hexane. The Fe_3O_4 NCs used for the encapsulation have an average size of 19±3 nm. These NCs were synthesized by Gorka Salas' group and dispersed in ODE for their later use at Fe=2.4 mg/ml.

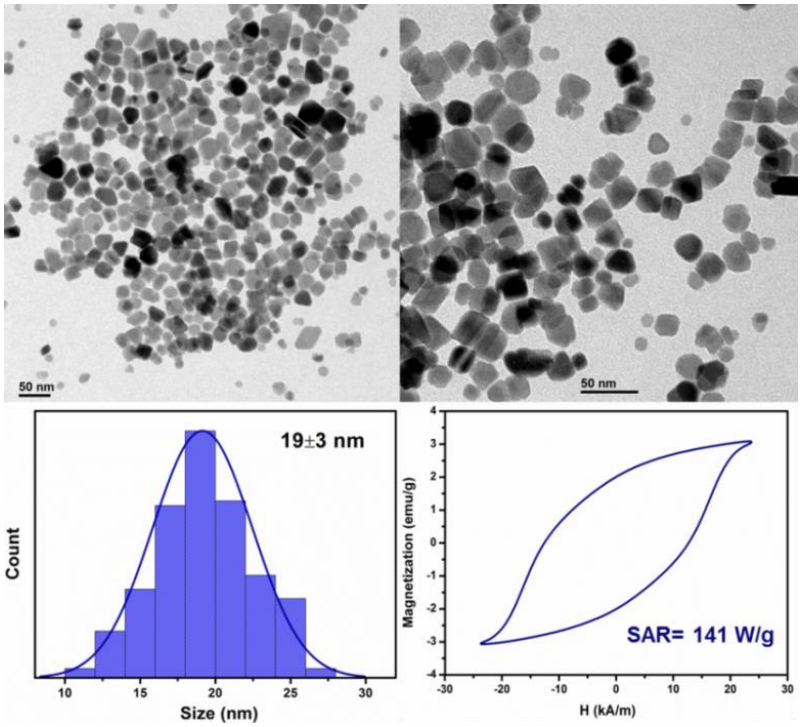

Figure 4. Morphological and magnetic characterization of the IONPs used in this Chapter

4.4. Microemulsion reaction

As previously discussed, SiO_2 has been used for the effective coating and water solubilization of different kinds of NCs like QDs or SPIONS. However, classic water-in-oil microemulsion method have failed to produce high quality silica coated Ag_2S NCs. The use of non-ionic surfactants in these reverse microemulsion systems leads to the destabilization of the colloidal solution of Ag_2S NCs making the homogeneous growth of silica spheres around the NC impossible. This effect is observed in Figure 4.2. The loss of the colloidal stability due to the presence of the aqueous face makes the NCs aggregate in order to minimize the surface in contact to the polar phase. This is why when the spheres form once the base is added the spheres form without the NCs.

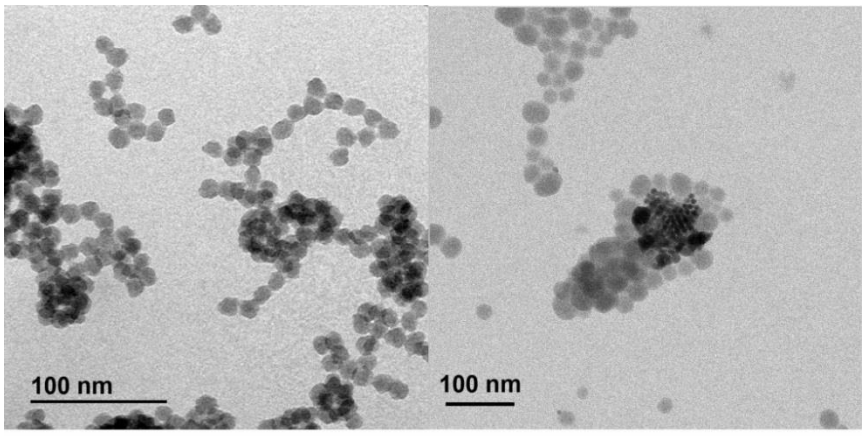

Figure 5. TEM images of attempts to encapsulate the Ag_2S-based NCs in SiO_2 spheres using the reverse microemulsion method

4.5. Silica encapsulation of $Ag_2S/Ag_2(S,Se)$ nanocrystals

In order to obtain the SiO_2-coated NCs 1 ml of a 1.8 mg/ml chloroform dispersion of Ag_2S-based NCs were mixed with a 3 ml water solution containing 30 mg of DTAB. The mixture was roughly sonicated and agitated until a homogeneous emulsion was achieved. After that, the chloroform was evaporated using a N_2 flow obtaining optically clear water dispersion. After that, 100 μl of TEOS was added to the water dispersion and the sample was left to slowly react at room temperature during 3 days in a mechanical agitator. After that, the excess silica was removed in several washing steps with ultrapure water.

4.6. Film hydration encapsulation of NCs

For the film hydration approach, 35 mg of PE:PEG2000 was first dissolved in 10 ml of chloroform. After that, 1 ml of Ag_2S-based NCs (1.8 mg/ml) were added to the phospholipid solution. The mixture was sonicated and agitated to achieve highest contact between both chemical species and after that the chloroform was evaporated using a N_2 flow. After that, 10 ml of ultrapure pure water are added and the dispersion is thoroughly agitated and sonicated until the phospholipids are closed. The first approach that was attempted to fabricate the magneto-optic multifunctional composite was the film hydration method as described in Section 4.4 of APPENDIX I. However, as TEM images point out, the NCs are not trapped inside the phospholipidic micelle, ending up interacting with the just the hydrophobic chains of its surface. This interaction between the phospholipid and the NCs has already been observed for CdSe QDs.[168]

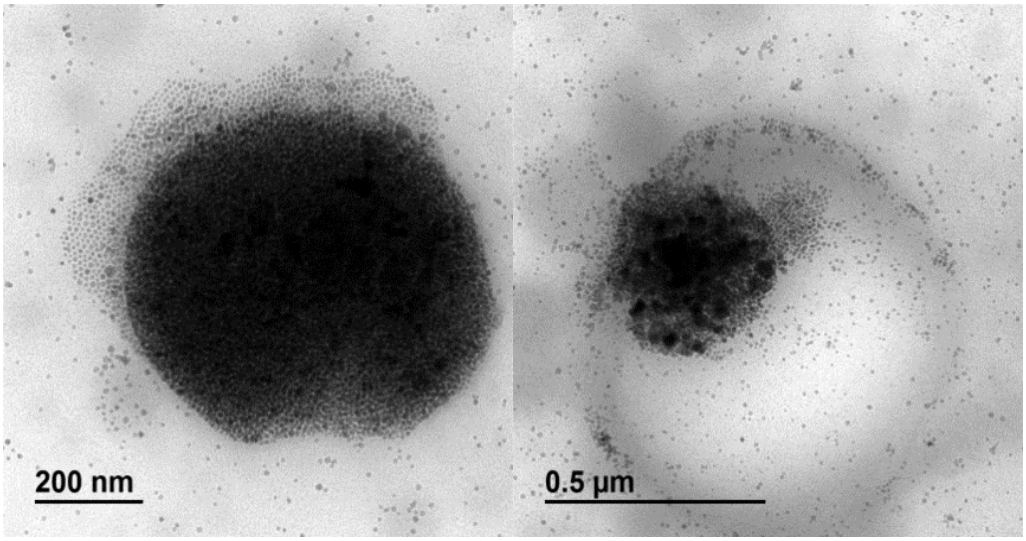

Figure 6. TEM images of the attempt to encapsulate both NCs using the film hydration method

4.7. Solvent exchange encapsulation

For the successful encapsulation of Ag_2S-based and Fe_3O_4 NCs 4 ml of 2 mg/ml chloroform dispersion of the MNPS and 8 ml of a 1.8 mg/ml dispersion of Ag_2S-based NCs are mixed together. After that, 2 ml of a 15 mg/ml solution of the PE:PEG2000 is added. The mixture is left 30 minutes in a mechanical agitator to promote the interaction between the NCs and the phospholipid. After that, 40 ml of DMSO are added to the chloroform mixture and after agitation and sonication the mixture is left so the chloroform evaporates at room temperature overnight. After that, the remaining chloroform is evaporated using a N_2 flow. Once the chloroform is completely removed, aliquots are taken from the DMSO batch. Every aliquot is diluted to half the concentration and then the double amount of water is added. After applying this last step to the whole batch the DMSO is removed from the sample by ultracentrifugation using Sartorius Vivaspin tubes with molecular cutoff of 10000 KDa.

4.8. Cell internalization studies

For the in vitro measurements, breast cancer cells (MCF-7 cells) were cultured in Dulbecco's modified Eagle's medium (DMEM) supplemented with 5% fetal bovine serum (FBS) and 1% penicillin, and maintained at 37°C with 5% CO2 until confluence.

The cells were incubated for 24 h with the Ag_2S-based NCs (FL13), at the following concentrations within the extracellular medium: [Fe] = 0.07 and 0.018 mM. At the end of the incubation, the medium was removed and the cells were rinsed three times with culture medium, and further placed at 37°C for an additional 30 min chase period. Particle-loaded living cells were visualized by optical microscopy. Cells were then detached by means of trypsin-EDTA solution and resuspended in phosphate-buffered saline (PBS) solution.

Bibliography

1. De Mello Donegá, C., *Nanoparticles: Workhorses of Nanoscience*. Springer: 2014.
2. Litvin, A. P.; Martynenko, I. V.; Purcell-Milton, F.; Baranov, A. V.; Fedorov, A. V.; Gun'ko, Y. K., Colloidal quantum dots for optoelectronics. *Journal of Materials Chemistry A* **2017,** *5* (26), 13252-13275.
3. Colombo, M.; Carregal-Romero, S.; Casula, M. F.; Gutiérrez, L.; Morales, M. P.; Böhm, I. B.; Heverhagen, J. T.; Prosperi, D.; Parak, W. J., Biological applications of magnetic nanoparticles. *Chemical Society Reviews* **2012,** *41* (11), 4306-4334.
4. Brown, W. F., The Fundamental Theorem of Fine-Ferromagnetic-Particle Theory. *Journal of Applied Physics* **1968,** *39* (2), 993-994.
5. Andrés Vergés, M.; Costo, R.; Roca, A. G.; Marco, J. F.; Goya, G. F.; Serna, C. J.; Morales, M. P., Uniform and water stable magnetite nanoparticles with diameters around the monodomain–multidomain limit. *Journal of Physics D: Applied Physics* **2008,** *41* (13), 134003.
6. Frey, N. A.; Peng, S.; Cheng, K.; Sun, S., Magnetic nanoparticles: synthesis, functionalization, and applications in bioimaging and magnetic energy storage. *Chemical Society Reviews* **2009,** *38* (9), 2532-2542.
7. Toraya-Brown, S.; Fiering, S., Local tumour hyperthermia as immunotherapy for metastatic cancer. *International journal of hyperthermia : the official journal of European Society for Hyperthermic Oncology, North American Hyperthermia Group* **2014,** *30* (8), 531-539.
8. Silva, A. C.; Oliveira, T. R.; Mamani, J. B.; Malheiros, S. M. F.; Malavolta, L.; Pavon, L. F.; Sibov, T. T.; Amaro, E., Jr.; Tannús, A.; Vidoto, E. L. G.; Martins, M. J.; Santos, R. S.; Gamarra, L. F., Application of hyperthermia induced by superparamagnetic iron oxide nanoparticles in glioma treatment. *International journal of nanomedicine* **2011,** *6*, 591-603.
9. Kumar, C. S. S. R.; Mohammad, F., Magnetic nanomaterials for hyperthermia-based therapy and controlled drug delivery. *Advanced Drug Delivery Reviews* **2011,** *63* (9), 789-808.
10. Xia, Y.; Xiong, Y.; Lim, B.; Skrabalak, S. E., Shape-Controlled Synthesis of Metal Nanocrystals: Simple Chemistry Meets Complex Physics? *Angewandte Chemie International Edition* **2009,** *48* (1), 60-103.
11. Sperling, R. A.; Rivera Gil, P.; Zhang, F.; Zanella, M.; Parak, W. J., Biological applications of gold nanoparticles. *Chemical Society Reviews* **2008,** *37* (9), 1896-1908.
12. Brus, L., Electronic wave functions in semiconductor clusters: experiment and theory. *The Journal of Physical Chemistry* **1986,** *90* (12), 2555-2560.
13. Vorobiev, Y. V.; Mera, B.; Vieira, V. R.; Horley, P. P.; González-Hernández, J., Weak and strong confinements in prismatic and cylindrical nanostructures. *Nanoscale research letters* **2012,** *7* (1), 371-371.
14. García de Arquer, F. P.; Armin, A.; Meredith, P.; Sargent, E. H., Solution-processed semiconductors for next-generation photodetectors. *Nature Reviews Materials* **2017,** *2* (3), 16100.
15. Bi, Y.; Pradhan, S.; Gupta, S.; Akgul, M. Z.; Stavrinadis, A.; Konstantatos, G., Infrared Solution-Processed Quantum Dot Solar Cells Reaching External Quantum Efficiency of 80% at 1.35 μm and Jsc in Excess of 34 mA cm−2. *Advanced Materials* **2018,** *30* (7), 1704928.
16. Chinnathambi, S.; Shirahata, N., Recent advances on fluorescent biomarkers of near-infrared quantum dots for in vitro and in vivo imaging. *Science and Technology of Advanced Materials* **2019,** *20* (1), 337-355.
17. Hong, G.; Antaris, A. L.; Dai, H., Near-infrared fluorophores for biomedical imaging. *Nature Biomedical Engineering* **2017,** *1* (1), 0010.
18. Smith, A. M.; Mancini, M. C.; Nie, S., Second Window for *in Vivo* Imaging. *Nature Nanotechnology* **2009,** *4*, 710-711.
19. Shrestha, A.; Batmunkh, M.; Tricoli, A.; Qiao, S. Z.; Dai, S., Near-Infrared Active Lead Chalcogenide Quantum Dots: Preparation, Post-Synthesis Ligand Exchange, and Applications in Solar Cells. *Angewandte Chemie International Edition* **2019,** *58* (16), 5202-5224.
20. Wise, F. W., Lead Salt Quantum Dots: the Limit of Strong Quantum Confinement. *Accounts of Chemical Research* **2000,** *33* (11), 773-780.
21. Weidman, M. C.; Beck, M. E.; Hoffman, R. S.; Prins, F.; Tisdale, W. A., Monodisperse, Air-Stable PbS Nanocrystals via Precursor Stoichiometry Control. *ACS Nano* **2014,** *8* (6), 6363-6371.
22. Benayas, A.; Ren, F.; Carrasco, E.; Marzal, V.; del Rosal, B.; Gonfa, B. A.; Juarranz, Á.; Sanz-Rodríguez, F.; Jaque, D.; García-Solé, J., PbS/CdS/ZnS Quantum Dots: A Multifunctional Platform for In Vivo Near-Infrared Low-Dose Fluorescence Imaging. *Advanced Functional Materials* **2015,** *25* (42), 6650-6659.
23. Tsukasaki, Y.; Morimatsu, M.; Nishimura, G.; Sakata, T.; Yasuda, H.; Komatsuzaki, A.; Watanabe, T. M.; Jin, T., Synthesis and optical properties of emission-tunable PbS/CdS core–shell quantum dots for in vivo fluorescence imaging in the second near-infrared window. *RSC Advances* **2014,** *4* (77), 41164-41171.
24. Cao, J.; Zhu, H.; Deng, D.; Xue, B.; Tang, L.; Mahounga, D.; Qian, Z.; Gu, Y., In vivo NIR imaging with PbS quantum dots entrapped in biodegradable micelles. *Journal of Biomedical Materials Research Part A* **2012,** *100A* (4), 958-968.
25. Lu, H.; Carroll, G. M.; Neale, N. R.; Beard, M. C., Infrared Quantum Dots: Progress, Challenges, and Opportunities. *ACS Nano* **2019,** *13* (2), 939-953.
26. Rogach, A. L.; Eychmüller, A.; Hickey, S. G.; Kershaw, S. V., Infrared-Emitting Colloidal Nanocrystals: Synthesis, Assembly, Spectroscopy, and Applications. *Small* **2007,** *3* (4), 536-557.

27. Yang, Y.; Jing, L.; Yu, X.; Yan, D.; Gao, M., Coating Aqueous Quantum Dots with Silica via Reverse Microemulsion Method: Toward Size-Controllable and Robust Fluorescent Nanoparticles. *Chemistry of Materials* **2007,** *19* (17), 4123-4128.
28. Girma, W. M.; Fahmi, M. Z.; Permadi, A.; Abate, M. A.; Chang, J.-Y., Synthetic strategies and biomedical applications of I–III–VI ternary quantum dots. *Journal of Materials Chemistry B* **2017,** *5* (31), 6193-6216.
29. Wang, R.; Zhang, F., NIR luminescent nanomaterials for biomedical imaging. *Journal of Materials Chemistry B* **2014,** *2* (17), 2422-2443.
30. Dong, B.; Li, C.; Chen, G.; Zhang, Y.; Zhang, Y.; Deng, M.; Wang, Q., Facile Synthesis of Highly Photoluminescent Ag2Se Quantum Dots as a New Fluorescent Probe in the Second Near-Infrared Window for in Vivo Imaging. *Chemistry of Materials* **2013,** *25* (12), 2503-2509.
31. Li, X.; Liu, Z.; Luo, K.; Yin, X.; Lin, X.; Zhu, C., Biomimetic Synthesis of Ag2Se Quantum Dots with Enhanced Photothermal Properties and as "Gatekeepers" to Cap Mesoporous Silica Nanoparticles for Chemo–Photothermal Therapy. *Chemistry – An Asian Journal* **2019,** *14* (1), 155-161.
32. Tang, H.; Yang, S.-T.; Ke, D.-M.; Yang, Y.-F.; Liu, J.-H.; Chen, X.; Wang, H.; Liu, Y., Biological behaviors and chemical fates of Ag(2)Se quantum dots in vivo: the effect of surface chemistry. *Toxicology research* **2017,** *6* (5), 693-704.
33. Liu, T.-M.; Conde, J.; Lipiński, T.; Bednarkiewicz, A.; Huang, C.-C., Revisiting the classification of NIR-absorbing/emitting nanomaterials for in vivo bioapplications. *NPG Asia Materials* **2016,** *8* (8), e295-e295.
34. Vogel, R.; Hoyer, P.; Weller, H., Quantum-Sized PbS, CdS, Ag2S, Sb2S3, and Bi2S3 Particles as Sensitizers for Various Nanoporous Wide-Bandgap Semiconductors. *The Journal of Physical Chemistry* **1994,** *98* (12), 3183-3188.
35. Murray, C. B.; Norris, D. J.; Bawendi, M. G., Synthesis and characterization of nearly monodisperse CdE (E = sulfur, selenium, tellurium) semiconductor nanocrystallites. *Journal of the American Chemical Society* **1993,** *115* (19), 8706-8715.
36. LaMer, V. K.; Dinegar, R. H., Theory, Production and Mechanism of Formation of Monodispersed Hydrosols. *Journal of the American Chemical Society* **1950,** *72* (11), 4847-4854.
37. van Embden, J.; Chesman, A. S. R.; Jasieniak, J. J., The Heat-Up Synthesis of Colloidal Nanocrystals. *Chemistry of Materials* **2015,** *27* (7), 2246-2285.
38. Henglein, A.; Gutiérrez, M.; Weller, K.; Fojtik, A.; Jirkovský, J., Photochemistry of colloidal semiconductors 30. Reactions and fluorescence of AgI and AgI — Ag2S colloids. *Berichte der Bunsengesellschaft für physikalische Chemie* **1989,** *93* (5), 593-600.
39. Motte, L.; Billoudet, F.; Lacaze, E.; Pileni, M.-P., Self-organization of size-selected, nanoparticles into three-dimensional superlattices. *Advanced Materials* **1996,** *8* (12), 1018-1020.
40. Motte, L.; Billoudet, F.; Lacaze, E.; Douin, J.; Pileni, M. P., Self-Organization into 2D and 3D Superlattices of Nanosized Particles Differing by Their Size. *The Journal of Physical Chemistry B* **1997,** *101* (2), 138-144.
41. Motte, L.; Billoudet, F.; Pileni, M. P., Self-Assembled Monolayer of Nanosized Particles Differing by Their Sizes. *The Journal of Physical Chemistry* **1995,** *99* (44), 16425-16429.
42. Pileni, M. P.; Motte, L.; Billoudet, F.; Mahrt, J.; Willig, F., Nanosized silver sulfide particles: characterization, self-organization into 2D and 3D superlattices. *Materials Letters* **1997,** *31* (3), 255-260.
43. Hocaoglu, I.; Demir, F.; Birer, O.; Kiraz, A.; Sevrin, C.; Grandfils, C.; Yagci Acar, H., Emission tunable, cyto/hemocompatible, near-IR-emitting Ag2S quantum dots by aqueous decomposition of DMSA. *Nanoscale* **2014,** *6* (20), 11921-11931.
44. Jiang, P.; Zhu, C.-N.; Zhang, Z.-L.; Tian, Z.-Q.; Pang, D.-W., Water-soluble Ag2S quantum dots for near-infrared fluorescence imaging in vivo. *Biomaterials* **2012,** *33* (20), 5130-5135.
45. Tang, R.; Xue, J.; Xu, B.; Shen, D.; Sudlow, G. P.; Achilefu, S., Tunable Ultrasmall Visible-to-Extended Near-Infrared Emitting Silver Sulfide Quantum Dots for Integrin-Targeted Cancer Imaging. *ACS Nano* **2015,** *9* (1), 220-230.
46. Zhang, Y.; Zhao, N.; Qin, Y.; Wu, F.; Xu, Z.; Lan, T.; Cheng, Z.; Zhao, P.; Liu, H., Affibody-functionalized Ag2S quantum dots for photoacoustic imaging of epidermal growth factor receptor overexpressed tumors. *Nanoscale* **2018,** *10* (35), 16581-16590.
47. Wang, Z.; Ma, Y.; Yu, X.; Niu, Q.; Han, Z.; Wang, H.; Li, T.; Fu, D.; Achilefu, S.; Qian, Z.; Gu, Y., Targeting CXCR4–CXCL12 Axis for Visualizing, Predicting, and Inhibiting Breast Cancer Metastasis with Theranostic AMD3100–Ag2S Quantum Dot Probe. *Advanced Functional Materials* **2018,** *28* (23), 1800732.
48. Kong, L.; Liu, W.; Chu, X.; Yao, Y.; Zhu, P.; Ling, X., Glutathione-directed synthesis of luminescent Ag_2S nanoclusters as nanosensors for copper(ii) ions and temperature. *RSC Advances* **2015,** *5* (98), 80530-80535.
49. Wang, C.; Wang, Y.; Xu, L.; Zhang, D.; Liu, M.; Li, X.; Sun, H.; Lin, Q.; Yang, B., Facile Aqueous-Phase Synthesis of Biocompatible and Fluorescent Ag2S Nanoclusters for Bioimaging: Tunable Photoluminescence from Red to Near Infrared. *Small* **2012,** *8* (20), 3137-3142.
50. Gui, R.; Wan, A.; Liu, X.; Yuan, W.; Jin, H., Water-soluble multidentate polymers compactly coating Ag2S quantum dots with minimized hydrodynamic size and bright emission tunable from red to second near-infrared region. *Nanoscale* **2014,** *6* (10), 5467-5473.
51. Chen, J.; Kong, Y.; Wo, Y.; Fang, H.; Li, Y.; Zhang, T.; Dong, Y.; Ge, Y.; Wu, Z.; Zhou, D.; Chen, S., Facile synthesis of β-lactoglobulin capped Ag2S quantum dots for in vivo imaging in the second near-infrared biological window. *Journal of Materials Chemistry B* **2016,** *4* (37), 6271-6278.
52. Yang, T.; Tang, Y. a.; Liu, L.; Lv, X.; Wang, Q.; Ke, H.; Deng, Y.; Yang, H.; Yang, X.; Liu, G.; Zhao, Y.; Chen, H., Size-Dependent Ag2S Nanodots for Second Near-Infrared Fluorescence/Photoacoustics Imaging and Simultaneous Photothermal Therapy. *ACS Nano* **2017,** *11* (2), 1848-1857.

53. Du, Y.; Xu, B.; Fu, T.; Cai, M.; Li, F.; Zhang, Y.; Wang, Q., Near-Infrared Photoluminescent Ag2S Quantum Dots from a Single Source Precursor. *Journal of the American Chemical Society* **2010,** *132* (5), 1470-1471.
54. Jiang, P.; Tian, Z.-Q.; Zhu, C.-N.; Zhang, Z.-L.; Pang, D.-W., Emission-Tunable Near-Infrared Ag_2S Quantum Dots. *Chemistry of Materials* **2012,** *24* (1), 3-5.
55. Zhang, H.; Hyun, B.-R.; Wise, F. W.; Robinson, R. D., A Generic Method for Rational Scalable Synthesis of Monodisperse Metal Sulfide Nanocrystals. *Nano Letters* **2012,** *12* (11), 5856-5860.
56. Zhu, G.; Xu, Z., Controllable Growth of Semiconductor Heterostructures Mediated by Bifunctional Ag2S Nanocrystals as Catalyst or Source-Host. *Journal of the American Chemical Society* **2011,** *133* (1), 148-157.
57. Doh, H.; Hwang, S.; Kim, S., Size-Tunable Synthesis of Nearly Monodisperse Ag_2S Nanoparticles and Size-Dependent Fate of the Crystal Structures upon Cation Exchange to $AgInS_2$ Nanoparticles. *Chemistry of Materials* **2016,** *28* (22), 8123-8127.
58. Ruiz, D.; Mizrahi, M.; Santos, H. D. A.; Jaque, D.; Jones, C. M. S.; Marqués-Hueso, J.; Jacinto, C.; Requejo, F. G.; Torres-Pardo, A.; González-Calbet, J. M.; Juárez, B. H., Synthesis and characterization of Ag 2 S and Ag 2 S/Ag 2 (S,Se) NIR nanocrystals. *Nanoscale* **2019,** *11* (18), 9194-9200.
59. Sahu, A.; Qi, L.; Kang, M. S.; Deng, D.; Norris, D. J., Facile Synthesis of Silver Chalcogenide (Ag2E; E = Se, S, Te) Semiconductor Nanocrystals. *Journal of the American Chemical Society* **2011,** *133* (17), 6509-6512.
60. Munro, A. M.; Jen-La Plante, I.; Ng, M. S.; Ginger, D. S., Quantitative Study of the Effects of Surface Ligand Concentration on CdSe Nanocrystal Photoluminescence. *The Journal of Physical Chemistry C* **2007,** *111* (17), 6220-6227.
61. Jeong, S.; Achermann, M.; Nanda, J.; Ivanov, S.; Klimov, V. I.; Hollingsworth, J. A., Effect of the Thiol−Thiolate Equilibrium on the Photophysical Properties of Aqueous CdSe/ZnS Nanocrystal Quantum Dots. *Journal of the American Chemical Society* **2005,** *127* (29), 10126-10127.
62. Hong, G.; Robinson, J. T.; Zhang, Y.; Diao, S.; Antaris, A. L.; Wang, Q.; Dai, H., In Vivo Fluorescence Imaging with Ag_2S Quantum Dots in the Second Near-Infrared Region. *Angewandte Chemie International Edition* **2012,** *51* (39), 9818-9821.
63. Nann, T.; Mulvaney, P., Single Quantum Dots in Spherical Silica Particles. *Angewandte Chemie International Edition* **2004,** *43* (40), 5393-5396.
64. Bollhorst, T.; Rezwan, K.; Maas, M., Colloidal capsules: nano- and microcapsules with colloidal particle shells. *Chemical Society Reviews* **2017,** *46* (8), 2091-2126.
65. Dubertret, B.; Skourides, P.; Norris, D. J.; Noireaux, V.; Brivanlou, A. H.; Libchaber, A., In Vivo Imaging of Quantum Dots Encapsulated in Phospholipid Micelles. *Science* **2002,** *298* (5599), 1759-1762.
66. Zhang, Y.; Liu, Y.; Li, C.; Chen, X.; Wang, Q., Controlled Synthesis of Ag_2S Quantum Dots and Experimental Determination of the Exciton Bohr Radius. *The Journal of Physical Chemistry C* **2014,** *118* (9), 4918-4923.
67. Wu, P.-J.; Yu, J.-W.; Chao, H.-J.; Chang, J.-Y., Silver-Based Metal Sulfide Heterostructures: Synthetic Approaches, Characterization, and Application Prospects. *Chemistry of Materials* **2014,** *26* (11), 3485-3494.
68. Ruiz, D.; Mizrahi, M.; Santos, H. D. A.; Jaque, D.; Jones, C. M. S.; Marqués-Hueso, J.; Jacinto, C.; Requejo, F. G.; Torres-Pardo, A.; González-Calbet, J. M.; Juárez, B. H., Synthesis and characterization of Ag2S and Ag2S/Ag2(S,Se) NIR nanocrystals. *Nanoscale* **2019,** *11* (18), 9194-9200.
69. Wang, Y.; Yan, X.-P., Fabrication of vascular endothelial growth factor antibody bioconjugated ultrasmall near-infrared fluorescent Ag_2S quantum dots for targeted cancer imaging in vivo. *Chemical Communications* **2013,** *49* (32), 3324-3326.
70. He, H.; Lin, Y.; Tian, Z. Q.; Zhu, D. L.; Zhang, Z. L.; Pang, D. W., Ultrasmall Pb:Ag2S Quantum Dots with Uniform Particle Size and Bright Tunable Fluorescence in the NIR-II Window. *Small* **2018,** *14* (11), 1703296.
71. Wang, Y.; Li, X.; Xu, M.; Wang, K.; Zhu, H.; Zhao, W.; Yan, J.; Zhang, Z., Pressure induced photoluminescence modulation in a wide range and synthesis of monodispersed ternary AgCuS nanocrystal based on Ag2S nanocrystals. *Nanoscale* **2018,** *10* (5), 2577-2587.
72. Jiang, P.; Zhu, D.-L.; Zhu, C.-N.; Zhang, Z.-L.; Zhang, G.-J.; Pang, D.-W., A highly reactive chalcogenide precursor for the synthesis of metal chalcogenide quantum dots. *Nanoscale* **2015,** *7* (45), 19310-19316.
73. Song, J.; Ma, C.; Zhang, W.; Li, X.; Zhang, W.; Wu, R.; Cheng, X.; Ali, A.; Yang, M.; Zhu, L.; Xia, R.; Xu, X., Bandgap and Structure Engineering via Cation Exchange: From Binary Ag2S to Ternary AgInS2, Quaternary AgZnInS alloy and AgZnInS/ZnS Core/Shell Fluorescent Nanocrystals for Bioimaging. *ACS Applied Materials & Interfaces* **2016,** *8* (37), 24826-24836.
74. Yang, H.-Y.; Zhao, Y.-W.; Zhang, Z.-Y.; Xiong, H.-M.; Yu, S.-N., One-pot synthesis of water-dispersible Ag2S quantum dots with bright fluorescent emission in the second near-infrared window. *Nanotechnology* **2013,** *24* (5), 055706.
75. Öberg, V. A.; Zhang, X.; Johansson, M. B.; Johansson, E. M. J., Hot-Injection Synthesized Ag2S Quantum Dots with Broad Light Absorption and High Stability for Solar Cell Applications. *ChemNanoMat* **2018,** *4* (12), 1223-1230.
76. Gao, J.; Wu, C.; Deng, D.; Wu, P.; Cai, C., Direct Synthesis of Water-Soluble Aptamer-Ag2S Quantum Dots at Ambient Temperature for Specific Imaging and Photothermal Therapy of Cancer. *Advanced Healthcare Materials* **2016,** *5* (18), 2437-2449.
77. Tan, L.; Wan, A.; Li, H., Ag2S Quantum Dots Conjugated Chitosan Nanospheres toward Light-Triggered Nitric Oxide Release and Near-Infrared Fluorescence Imaging. *Langmuir* **2013,** *29* (48), 15032-15042.
78. Asik, D.; Yagci, M. B.; Demir Duman, F.; Yagci Acar, H., One step emission tunable synthesis of PEG coated Ag2S NIR quantum dots and the development of receptor targeted drug delivery vehicles thereof. *Journal of Materials Chemistry B* **2016,** *4* (11), 1941-1950.

79. Lin, S.; Feng, Y.; Wen, X.; Zhang, P.; Woo, S.; Shrestha, S.; Conibeer, G.; Huang, S., Theoretical and Experimental Investigation of the Electronic Structure and Quantum Confinement of Wet-Chemistry Synthesized Ag_2S Nanocrystals. *The Journal of Physical Chemistry C* **2015,** *119* (1), 867-872.
80. Ruiz, D.; del Rosal, B.; Acebrón, M.; Palencia, C.; Sun, C.; Cabanillas-González, J.; López-Haro, M.; Hungría, A. B.; Jaque, D.; Juarez, B. H., Ag/Ag2S Nanocrystals for High Sensitivity Near-Infrared Luminescence Nanothermometry. *Advanced Functional Materials* **2017,** *27* (6), 1604629.
81. Ding, C.; Cao, X.; Zhang, C.; He, T.; Hua, N.; Xian, Y., Rare earth ions enhanced near infrared fluorescence of Ag2S quantum dots for the detection of fluoride ions in living cells. *Nanoscale* **2017,** *9* (37), 14031-14038.
82. Zhang, Y.; Hong, G.; Zhang, Y.; Chen, G.; Li, F.; Dai, H.; Wang, Q., Ag_2S Quantum Dot: A Bright and Biocompatible Fluorescent Nanoprobe in the Second Near-Infrared Window. *ACS Nano* **2012,** *6* (5), 3695-3702.
83. Zhao, J.; Zhong, D.; Zhou, S., NIR-I-to-NIR-II fluorescent nanomaterials for biomedical imaging and cancer therapy. *Journal of Materials Chemistry B* **2018,** *6* (3), 349-365.
84. Chen, G.; Tian, F.; Zhang, Y.; Zhang, Y.; Li, C.; Wang, Q., Tracking of Transplanted Human Mesenchymal Stem Cells in Living Mice using Near-Infrared Ag2S Quantum Dots. *Advanced Functional Materials* **2013,** *24* (17), 2481-2488.
85. Li, C.; Zhang, Y.; Wang, M.; Zhang, Y.; Chen, G.; Li, L.; Wu, D.; Wang, Q., In vivo real-time visualization of tissue blood flow and angiogenesis using Ag_2S quantum dots in the NIR-II window. *Biomaterials* **2014,** *35* (1), 393-400.
86. Wu, C.; Zhang, Y.; Li, Z.; Li, C.; Wang, Q., A novel photoacoustic nanoprobe of ICG@PEG-Ag2S for atherosclerosis targeting and imaging in vivo. *Nanoscale* **2016,** *8* (25), 12531-12539.
87. Chenghao, L.; Guihuan, C.; Bing, Y.; Hailin, C., Recent Advances of Low Biological Toxicity Ag2S QDs for Biomedical Application. *Advanced Engineering Materials* **2018,** *0* (0), 1700940.
88. Cheng, K.; Yang, X.-Q.; Zhang, X.-S.; Chen, J.; An, J.; Song, Y.-Y.; Li, C.; Xuan, Y.; Zhang, R.-Y.; Yang, C.-H.; Song, X.-L.; Zhao, Y.-D.; Liu, B., High-Security Nanocluster for Switching Photodynamic Combining Photothermal and Acid-Induced Drug Compliance Therapy Guided by Multimodal Active-Targeting Imaging. *Advanced Functional Materials* **2018,** *28* (36), 1803118.
89. Cheng, K.; Zhang, X.-S.; An, J.; Li, C.; Zhang, R.-Y.; Ye, R.; Ye, B.-J.; Liu, B.; Zhao, Y.-D., Hitherto-Unexplored Photodynamic Therapy of Ag2S and Enhanced Regulation Based on Polydopamine In Vitro and Vivo. *Chemistry – A European Journal* **2019,** *25* (31), 7553-7560.
90. Brites, C. D. S.; Lima, P. P.; Silva, N. J. O.; Millan, A.; Amaral, V. S.; Palacio, F.; Carlos, L. D., Thermometry at the nanoscale. *Nanoscale* **2012,** *4* (16), 4799-4829.
91. Ring, E.; Ammer, K., Infrared thermal imaging in medicine. *Physiological measurement* **2012,** *33* (3), R33.
92. Labrador-Páez, L.; Pedroni, M.; Speghini, A.; García-Solé, J.; Haro-González, P.; Jaque, D., Reliability of rare-earth-doped infrared luminescent nanothermometers. *Nanoscale* **2018,** *10* (47), 22319-22328.
93. Jaque, D.; Vetrone, F., Luminescence nanothermometry. *Nanoscale* **2012,** *4* (15), 4301-4326.
94. Arora, N.; Martins, D.; Ruggerio, D.; Tousimis, E.; Swistel, A. J.; Osborne, M. P.; Simmons, R. M., Effectiveness of a noninvasive digital infrared thermal imaging system in the detection of breast cancer. *The American Journal of Surgery* **2008,** *196* (4), 523-526.
95. Ng, E.-K., A review of thermography as promising non-invasive detection modality for breast tumor. *International Journal of Thermal Sciences* **2009,** *48* (5), 849-859.
96. Herman, C.; Cetingul, M. P., Quantitative visualization and detection of skin cancer using dynamic thermal imaging. *Journal of Visualized Experiments* **2011,** *51*.
97. Madjid, M.; Naghavi, M.; Malik, B. A.; Litovsky, S.; Willerson, J. T.; Casscells, W., Thermal detection of vulnerable plaque. *The American journal of cardiology* **2002,** *90* (10), L36-L39.
98. Bashkatov, A.; Genina, E.; Kochubey, V.; Tuchin, V., Optical properties of human skin, subcutaneous and mucous tissues in the wavelength range from 400 to 2000 nm. *Journal of Physics D: Applied Physics* **2005,** *38* (15), 2543.
99. Weissleder, R., A clearer vision for in vivo imaging. *Nat Biotechnol* **2001,** *19* (4), 316-7.
100. Andersson, H.; Baechi, T.; Hoechl, M.; Richter, C., Autofluorescence of living cells. *Journal of microscopy* **1998,** *191* (Pt 1), 1-7.
101. Ximendes, E. C.; Santos, W. Q.; Rocha, U.; Kagola, U. K.; Sanz-Rodríguez, F.; Fernández, N.; Gouveia-Neto, A. d. S.; Bravo, D.; Domingo, A. M.; del Rosal, B.; Brites, C. D. S.; Carlos, L. D.; Jaque, D.; Jacinto, C., Unveiling in Vivo Subcutaneous Thermal Dynamics by Infrared Luminescent Nanothermometers. *Nano Letters* **2016,** *16* (3), 1695-1703.
102. Cerón, E. N.; Ortgies, D. H.; del Rosal, B.; Ren, F.; Benayas, A.; Vetrone, F.; Ma, D.; Sanz-Rodríguez, F.; Solé, J. G.; Jaque, D.; Rodríguez, E. M., Hybrid Nanostructures for High-Sensitivity Luminescence Nanothermometry in the Second Biological Window. *Advanced Materials* **2015,** *27* (32), 4781-4787.
103. Rocha, U.; Jacinto da Silva, C.; Ferreira Silva, W.; Guedes, I.; Benayas, A.; Martínez Maestro, L.; Acosta Elias, M.; Bovero, E.; van Veggel, F. C. J. M.; García Solé, J. A.; Jaque, D., Subtissue Thermal Sensing Based on Neodymium-Doped LaF_3 Nanoparticles. *ACS Nano* **2013,** *7* (2), 1188-1199.
104. Marciniak, L.; Bednarkiewicz, A.; Stefanski, M.; Tomala, R.; Hreniak, D.; Strek, W., Near infrared absorbing near infrared emitting highly-sensitive luminescent nanothermometer based on Nd^{3+} to Yb^{3+} energy transfer. *Physical Chemistry Chemical Physics* **2015,** *17* (37), 24315-24321.
105. Tang, A.; Wang, Y.; Ye, H.; Zhou, C.; Yang, C.; Li, X.; Peng, H.; Zhang, F.; Hou, Y.; Teng, F., Controllable synthesis of silver and silver sulfide nanocrystals via selective cleavage of chemical bonds. *Nanotechnology* **2013,** *24* (35), 355602.

106. Mir, W. J.; Swarnkar, A.; Sharma, R.; Katti, A.; Adarsh, K. V.; Nag, A., Origin of Unusual Excitonic Absorption and Emission from Colloidal Ag_2S Nanocrystals: Ultrafast Photophysics and Solar Cell. *The Journal of Physical Chemistry Letters* **2015,** *6* (19), 3915-3922.
107. Hatami, S.; Würth, C.; Kaiser, M.; Leubner, S.; Gabriel, S.; Bahrig, L.; Lesnyak, V.; Pauli, J.; Gaponik, N.; Eychmüller, A.; Resch-Genger, U., Absolute photoluminescence quantum yields of IR26 and IR-emissive Cd1−xHgxTe and PbS quantum dots – method- and material-inherent challenges. *Nanoscale* **2015,** *7* (1), 133-143.
108. Semonin, O. E.; Johnson, J. C.; Luther, J. M.; Midgett, A. G.; Nozik, A. J.; Beard, M. C., Absolute Photoluminescence Quantum Yields of IR-26 Dye, PbS, and PbSe Quantum Dots. *The Journal of Physical Chemistry Letters* **2010,** *1* (16), 2445-2450.
109. Zhang, Y.; Hong, G.; Zhang, Y.; Chen, G.; Li, F.; Dai, H.; Wang, Q., Ag2S quantum dot: a bright and biocompatible fluorescent nanoprobe in the second near-infrared window. *ACS Nano* **2012,** *6* (5), 3695-702.
110. del Rosal, B.; Ruiz, D.; Chaves-Coira, I.; Juárez, B. H.; Monge, L.; Hong, G.; Fernández, N.; Jaque, D., In Vivo Contactless Brain Nanothermometry. *Advanced Functional Materials* **2018,** *0* (0), 1806088.
111. Lehovec, K., On the Temperature Dependence of the Optical Absorption of β—Ag_2S. *The Journal of Chemical Physics* **1953,** *21*, 54-57.
112. Debruyne, D.; Deschaume, O.; Coutiño-Gonzalez, E.; Locquet, J.-P.; Hofkens, J.; Van Bael, M. J.; Bartic, C., The pH-dependent photoluminescence of colloidal CdSe/ZnS quantum dots with different organic coatings. *Nanotechnology* **2015,** *26* (25), 255703.
113. Santra, P. K.; Viswanatha, R.; Daniels, S. M.; Pickett, N. L.; Smith, J. M.; O'Brien, P.; Sarma, D. D., Investigation of the Internal Heterostructure of Highly Luminescent Quantum Dot−Quantum Well Nanocrystals. *Journal of the American Chemical Society* **2009,** *131* (2), 470-477.
114. Taleb, A.; Petit, C.; Pileni, M. P., Optical Properties of Self-Assembled 2D and 3D Superlattices of Silver Nanoparticles. *The Journal of Physical Chemistry B* **1998,** *102* (12), 2214-2220.
115. Shen, S.; Zhang, Y.; Peng, L.; Du, Y.; Wang, Q., Matchstick-Shaped Ag2S–ZnS Heteronanostructures Preserving both UV/Blue and Near-Infrared Photoluminescence. *Angewandte Chemie International Edition* **2011,** *50* (31), 7115-7118.
116. Zhuang, Z.; Lu, X.; Peng, Q.; Li, Y., A Facile "Dispersion–Decomposition" Route to Metal Sulfide Nanocrystals. *Chemistry – A European Journal* **2011,** *17* (37), 10445-10452.
117. Saldanha, P. L.; Brescia, R.; Prato, M.; Li, H.; Povia, M.; Manna, L.; Lesnyak, V., Generalized One-Pot Synthesis of Copper Sulfide, Selenide-Sulfide, and Telluride-Sulfide Nanoparticles. *Chemistry of Materials* **2014,** *26* (3), 1442-1449.
118. Kriegel, I.; Rodríguez-Fernández, J.; Como, E. D.; Lutich, A. A.; Szeifert, J. M.; Feldmann, J., Tuning the Light Absorption of Cu1.97S Nanocrystals in Supercrystal Structures. *Chemistry of Materials* **2011,** *23* (7), 1830-1834.
119. Turo, M. J.; Macdonald, J. E., Crystal-Bound vs Surface-Bound Thiols on Nanocrystals. *ACS Nano* **2014,** *8* (10), 10205-10213.
120. Xie, R.; Rutherford, M.; Peng, X., Formation of High-Quality I−III−VI Semiconductor Nanocrystals by Tuning Relative Reactivity of Cationic Precursors. *Journal of the American Chemical Society* **2009,** *131* (15), 5691-5697.
121. Gromova, M.; Lefrançois, A.; Vaure, L.; Agnese, F.; Aldakov, D.; Maurice, A.; Djurado, D.; Lebrun, C.; de Geyer, A.; Schülli, T. U.; Pouget, S.; Reiss, P., Growth Mechanism and Surface State of CuInS2 Nanocrystals Synthesized with Dodecanethiol. *Journal of the American Chemical Society* **2017,** *139* (44), 15748-15759.
122. Pan, Z.; Mora-Seró, I.; Shen, Q.; Zhang, H.; Li, Y.; Zhao, K.; Wang, J.; Zhong, X.; Bisquert, J., High-Efficiency "Green" Quantum Dot Solar Cells. *Journal of the American Chemical Society* **2014,** *136* (25), 9203-9210.
123. van Oversteeg, C. H. M.; Oropeza, F. E.; Hofmann, J. P.; Hensen, E. J. M.; de Jongh, P. E.; de Mello Donega, C., Water-Dispersible Copper Sulfide Nanocrystals via Ligand Exchange of 1-Dodecanethiol. *Chemistry of Materials* **2019,** *31* (2), 541-552.
124. Reiss, P.; Protière, M.; Li, L., Core/Shell Semiconductor Nanocrystals. *Small* **2009,** *5* (2), 154-168.
125. Shen, Y.; Lifante, J.; Ximendes, E.; Santos, H. D. A.; Ruiz, D.; Juárez, B. H.; Zabala Gutiérrez, I.; Torres Vera, V.; Rubio Retama, J.; Martín Rodríguez, E.; Ortgies, D. H.; Jaque, D.; Benayas, A.; del Rosal, B., Perspectives for Ag2S NIR-II nanoparticles in biomedicine: from imaging to multifunctionality. *Nanoscale* **2019**.
126. Kim, J.-U.; Cha, S.-H.; Shin, K.; Jho, J. Y.; Lee, J.-C., Synthesis of Gold Nanoparticles from Gold(I)−Alkanethiolate Complexes with Supramolecular Structures through Electron Beam Irradiation in TEM. *Journal of the American Chemical Society* **2005,** *127* (28), 9962-9963.
127. Sandhyarani, N.; Pradeep, T., An investigation of the structure and properties of layered copper thiolates. *Journal of Materials Chemistry* **2001,** *11* (4), 1294-1299.
128. Busupalli, B.; Kummara, S.; Kumaraswamy, G.; Prasad, B. L. V., Ultrathin Sheets of Metal or Metal Sulfide from Molecularly Thin Sheets of Metal Thiolates in Solution. *Chemistry of Materials* **2014,** *26* (11), 3436-3442.
129. Ye, Z.; de la Rama, L. P.; Efremov, M. Y.; Zuo, J.-M.; Allen, L. H., Approaching the size limit of organometallic layers: synthesis and characterization of highly ordered silver-thiolate lamellae with ultra-short chain lengths. *Dalton Transactions* **2016,** *45* (47), 18954-18966.
130. John, N. S.; Kulkarni, G. U.; Datta, A.; Pati, S. K.; Komori, F.; Kavitha, G.; Narayana, C.; Sanyal, M. K., Magnetic Interactions in Layered Nickel Alkanethiolates. *The Journal of Physical Chemistry C* **2007,** *111* (5), 1868-1870.

131. Chen, J.; Chen, L.; Wu, L.-M., The Solventless Syntheses of Unique PbS Nanowires of X-Shaped Cross Sections and the Cooperative Effects of Ethylenediamine and a Second Salt. *Inorganic Chemistry* **2007,** *46* (19), 8038-8043.
132. Bryks, W.; Smith, S. C.; Tao, A. R., Metallomesogen Templates for Shape Control of Metal Selenide Nanocrystals. *Chemistry of Materials* **2017,** *29* (8), 3653-3662.
133. Dance, I. G.; Fisher, K. J.; Banda, R. M. H.; Scudder, M. L., Layered structure of crystalline compounds silver thiolates (AgSR). *Inorganic Chemistry* **1991,** *30* (2), 183-187.
134. Bryks, W.; Wette, M.; Velez, N.; Hsu, S.-W.; Tao, A. R., Supramolecular Precursors for the Synthesis of Anisotropic Cu2S Nanocrystals. *Journal of the American Chemical Society* **2014,** *136* (17), 6175-6178.
135. Hens, Z.; Martins, J. C., A Solution NMR Toolbox for Characterizing the Surface Chemistry of Colloidal Nanocrystals. *Chemistry of Materials* **2013,** *25* (8), 1211-1221.
136. Acebrón, M.; Galisteo-López, J. F.; Granados, D.; López-Ogalla, J.; Gallego, J. M.; Otero, R.; López, C.; Juárez, B. H., Protective Ligand Shells for Luminescent SiO2-Coated Alloyed Semiconductor Nanocrystals. *ACS Applied Materials & Interfaces* **2015,** *7* (12), 6935-6945.
137. Reiss, P.; Carrière, M.; Lincheneau, C.; Vaure, L.; Tamang, S., Synthesis of Semiconductor Nanocrystals, Focusing on Nontoxic and Earth-Abundant Materials. *Chemical Reviews* **2016,** *116* (18), 10731-10819.
138. Fritzinger, B.; Capek, R. K.; Lambert, K.; Martins, J. C.; Hens, Z., Utilizing Self-Exchange To Address the Binding of Carboxylic Acid Ligands to CdSe Quantum Dots. *Journal of the American Chemical Society* **2010,** *132* (29), 10195-10201.
139. Levchenko, A. A.; Yee, C. K.; Parikh, A. N.; Navrotsky, A., Energetics of Self-Assembly and Chain Confinement in Silver Alkanethiolates: Enthalpy−Entropy Interplay. *Chemistry of Materials* **2005,** *17* (22), 5428-5438.
140. Thomson, J. W.; Nagashima, K.; Macdonald, P. M.; Ozin, G. A., From Sulfur−Amine Solutions to Metal Sulfide Nanocrystals: Peering into the Oleylamine−Sulfur Black Box. *Journal of the American Chemical Society* **2011,** *133* (13), 5036-5041.
141. Mikhlin, Y. L.; Pal'yanova, G. A.; Tomashevich, Y. V.; Vishnyakova, E. A.; Vorobyev, S. A.; Kokh, K. A., XPS and Ag L3-edge XANES characterization of silver and silver–gold sulfoselenides. *Journal of Physics and Chemistry of Solids* **2018,** *116*, 292-298.
142. Padmos, J. D.; Zhang, P., Surface Structure of Organosulfur Stabilized Silver Nanoparticles Studied with X-ray Absorption Spectroscopy. *The Journal of Physical Chemistry C* **2012,** *116* (43), 23094-23101.
143. Nakazawa, E.; Ikemoto, T.; Hokura, A.; Terada, Y.; Kunito, T.; Yamamoto, T.; Yamada, T. K.; Rosas, F. C. W.; Fillmann, G.; Tanabe, S.; Nakai, I., Silver speciation in liver of marine mammals by synchrotron X-ray absorption fine structure and X-ray fluorescence spectroscopies. *Journal of Environmental Monitoring* **2011,** *13* (6), 1678-1686.
144. Frenkel, A. I.; Yevick, A.; Cooper, C.; Vasic, R., Modeling the Structure and Composition of Nanoparticles by Extended X-Ray Absorption Fine-Structure Spectroscopy. *Annual Review of Analytical Chemistry* **2011,** *4* (1), 23-39.
145. Rehr, J. J.; Kas, J. J.; Vila, F. D.; Prange, M. P.; Jorissen, K., Parameter-free calculations of X-ray spectra with FEFF9. *Physical Chemistry Chemical Physics* **2010,** *12* (21), 5503-5513.
146. Ito, A.; Shinkai, M.; Honda, H.; Kobayashi, T., Medical application of functionalized magnetic nanoparticles. *Journal of Bioscience and Bioengineering* **2005,** *100* (1), 1-11.
147. Kossatz, S.; Ludwig, R.; Dähring, H.; Ettelt, V.; Rimkus, G.; Marciello, M.; Salas, G.; Patel, V.; Teran, F. J.; Hilger, I., High therapeutic efficiency of magnetic hyperthermia in xenograft models achieved with moderate temperature dosages in the tumor area. *Pharmaceutical research* **2014,** *31* (12), 3274-3288.
148. Rodrigues, H. F.; Capistrano, G.; Mello, F. M.; Zufelato, N.; Silveira-Lacerda, E.; Bakuzis, A. F., Precise determination of the heat delivery duringin vivomagnetic nanoparticle hyperthermia with infrared thermography. *Physics in Medicine and Biology* **2017,** *62* (10), 4062-4082.
149. Hirsch, L. R.; Stafford, R. J.; Bankson, J. A.; Sershen, S. R.; Rivera, B.; Price, R. E.; Hazle, J. D.; Halas, N. J.; West, J. L., Nanoshell-mediated near-infrared thermal therapy of tumors under magnetic resonance guidance. *Proceedings of the National Academy of Sciences* **2003,** *100* (23), 13549.
150. Liz-Marzán, L. M.; Giersig, M.; Mulvaney, P., Synthesis of Nanosized Gold−Silica Core−Shell Particles. *Langmuir* **1996,** *12* (18), 4329-4335.
151. Pastoriza-Santos, I.; Pérez-Juste, J.; Liz-Marzán, L. M., Silica-Coating and Hydrophobation of CTAB-Stabilized Gold Nanorods. *Chemistry of Materials* **2006,** *18* (10), 2465-2467.
152. Pietra, F.; van Dijk - Moes, R. J. A.; Ke, X.; Bals, S.; Van Tendeloo, G.; de Mello Donega, C.; Vanmaekelbergh, D., Synthesis of Highly Luminescent Silica-Coated CdSe/CdS Nanorods. *Chemistry of Materials* **2013,** *25* (17), 3427-3434.
153. Ding, H. L.; Zhang, Y. X.; Wang, S.; Xu, J. M.; Xu, S. C.; Li, G. H., Fe3O4@SiO2 Core/Shell Nanoparticles: The Silica Coating Regulations with a Single Core for Different Core Sizes and Shell Thicknesses. *Chemistry of Materials* **2012,** *24* (23), 4572-4580.
154. Hui, C.; Shen, C.; Tian, J.; Bao, L.; Ding, H.; Li, C.; Tian, Y.; Shi, X.; Gao, H.-J., Core-shell Fe3O4@SiO2 nanoparticles synthesized with well-dispersed hydrophilic Fe3O4 seeds. *Nanoscale* **2011,** *3* (2), 701-705.
155. Ortgies, D. H.; Teran, F. J.; Rocha, U.; Cueva, L. d. l.; Salas, G.; Cabrera, D.; Vanetsev, A. S.; Rähn, M.; Sammelselg, V.; Orlovskii, Y. V.; Jaque, D., Optomagnetic Nanoplatforms for In Situ Controlled Hyperthermia. *Advanced Functional Materials* **2018,** *28* (11).

156. Ortgies, D. H.; de la Cueva, L.; del Rosal, B.; Sanz-Rodríguez, F.; Fernández, N.; Iglesias-de la Cruz, M. C.; Salas, G.; Cabrera, D.; Teran, F. J.; Jaque, D.; Martín Rodríguez, E., In Vivo Deep Tissue Fluorescence and Magnetic Imaging Employing Hybrid Nanostructures. *ACS Applied Materials & Interfaces* **2016,** *8* (2), 1406-1414.
157. Thompson, K. L.; Williams, M.; Armes, S. P., Colloidosomes: Synthesis, properties and applications. *Journal of Colloid and Interface Science* **2015,** *447*, 217-228.
158. Li, M.; Luo, Z.; Zhao, Y., Self-Assembled Hybrid Nanostructures: Versatile Multifunctional Nanoplatforms for Cancer Diagnosis and Therapy. *Chemistry of Materials* **2018,** *30* (1), 25-53.
159. Tong, S.; Hou, S.; Ren, B.; Zheng, Z.; Bao, G., Self-Assembly of Phospholipid–PEG Coating on Nanoparticles through Dual Solvent Exchange. *Nano Letters* **2011,** *11* (9), 3720-3726.
160. Tong, S.; Quinto, C. A.; Zhang, L.; Mohindra, P.; Bao, G., Size-Dependent Heating of Magnetic Iron Oxide Nanoparticles. *ACS Nano* **2017,** *11* (7), 6808-6816.
161. Johnson, N. J. J.; He, S.; Nguyen Huu, V. A.; Almutairi, A., Compact Micellization: A Strategy for Ultrahigh T1 Magnetic Resonance Contrast with Gadolinium-Based Nanocrystals. *ACS Nano* **2016,** *10* (9), 8299-8307.
162. Erogbogbo, F.; Yong, K.-T.; Roy, I.; Xu, G.; Prasad, P. N.; Swihart, M. T., Biocompatible Luminescent Silicon Quantum Dots for Imaging of Cancer Cells. *ACS Nano* **2008,** *2* (5), 873-878.
163. Stöber, W.; Fink, A.; Bohn, E., Controlled growth of monodisperse silica spheres in the micron size range. *Journal of Colloid and Interface Science* **1968,** *26* (1), 62-69.
164. Torchilin, V. P., PEG-based micelles as carriers of contrast agents for different imaging modalities. *Advanced Drug Delivery Reviews* **2002,** *54* (2), 235-252.
165. Piñeiro-Redondo, Y.; Bañobre-López, M.; Pardiñas-Blanco, I.; Goya, G.; López-Quintela, M. A.; Rivas, J., The influence of colloidal parameters on the specific power absorption of PAA-coated magnetite nanoparticles. *Nanoscale research letters* **2011,** *6* (1), 383-383.
166. Ravel, B.; Newville, M., ATHENA, ARTEMIS, HEPHAESTUS: data analysis for X-ray absorption spectroscopy using IFEFFIT. *Journal of Synchrotron Radiation* **2005,** *12* (4), 537-541.
167. Sun, S.; Zeng, H., Size-Controlled Synthesis of Magnetite Nanoparticles. *Journal of the American Chemical Society* **2002,** *124* (28), 8204-8205.
168. Gopalakrishnan, G.; Danelon, C.; Izewska, P.; Prummer, M.; Bolinger, P.-Y.; Geissbühler, I.; Demurtas, D.; Dubochet, J.; Vogel, H., Multifunctional Lipid/Quantum Dot Hybrid Nanocontainers for Controlled Targeting of Live Cells. *Angewandte Chemie International Edition* **2006,** *45* (33), 5478-5483.

List of abbreviations

A.U.	Arbitrary units
CCD	Charge Coupled Device
CS	Core/Shell
DOSY	Diffusion Ordered Spectroscopy
EDS	X-ray Energy Dispersive Spectroscopy
EELS	Electron Energy Loss Spectroscopy
Eg	Energy band gap
EXAFS	Extended X-ray Absorption Fine Structure
HAADF	High-Angle Annular Dark Field
HREM	High Resolution Electron Microscopy
ICP-OES	Inductively Coupled Plasma Optic Emission Spectrometry
IR	Infrared
NIR	Near-infrared
NC(s)	Nanocrystal(s)
NMR	Nuclear Magnetic Resonance
PL	Photoluminescence
(PL)QY	Photoluminescence Quantum Yield
QD(s)	Quantum Dot(s)
SPION(s)	Superparamagnetic Iron Oxide Nanoparticle(s)
STEM	Scanning Transmission Electron Microscopy
TAS	Transient Absorption Spectroscopy
TEM	Transmission Electron Microscopy
TF	Thin Film

XANES	X-ray Absorption Near Edge Structure
XPS	X-ray Photoelectron Spectroscopy
XRD	X-ray Diffraction

List of publications

1. Ag/Ag_2S nanocrystals for high sensitivity near-infrared luminescence nanothermometry"

   Diego Ruiz, Blanca del Rosal, María Acebrón, Cristina Palencia, Chen Sun, Juan Cabanillas-González, Miguel López-Haro, Ana B. Hungría, Daniel Jaque and Beatriz H. Juárez.

   Advanced Functional Materials, **2017**, 27, *6*, 1604629

2. Time resolved spectroscopy of infrared emitting Ag2S nanocrystals for subcutaneous thermometry

   Harrisson D. A. Santos, **Diego Ruiz**, Ginés Lifante, Carlos Jacinto, Beatriz H. Juárez and Daniel Jaque

   Nanoscale, **2017**, *9*, 2505

3. In vivo contactless brain nanothermometry

   Blanca del Rosal, **Diego Ruiz**, Irene Chaves-Coira, Beatriz H. Juárez, Luis Monge, Guosong Hong, Nuria Fernández and Daniel Jaque

   Advanced Functional Materials, **2018**, 28, *52*, 1806088

4. Synthesis and characterization of Ag_2S and $Ag_2S(S,Se)$ NIR nanocrystals

   Diego Ruiz, Martín Mizrahi, Harrisson D. A. Santos, Daniel Jaque, Callum M. S. Jones, José Marqués-Hueso, Carlos Jacinto, Félix G. Requejo, Almudena Torres-Pardo, José M. González-Calbet and Beatriz H. Juárez.

   Nanoscale, **2019**, *11*, 9194

5. Perspectives for Ag_2S NIR-II nanoparticles in biomedicine: from imaging to multifunctionality.

   Yingli Shen, José Lifante, Erving Ximendes, Harrisson D. A. Santos, **Diego Ruiz**, Beatriz H. Juárez, Irene Zabala Gutiérrez, Vivian Torres Vera, Jorge Rubio Retama, Emma Martín Rodríguez, Dirk Ortgies, Daniel Jaque García, Antonio Benayas and Blanca del Rosal.

   Nanoscale, Accepted.

6. Hybrid opto-magnetic nanostructures based on SPIONs and near-infrared emitting nanocrystals for simultaneous hyperthermia and luminescence thermometry,

   In preparation

Oral communications

1. "Ag_2S nanocrystals as ratiometric luminescence nanothermometry probes"
   Authors: **Diego Ruiz**, María Acebrón, Chen Sun, Miguel López-Haro, Blanca del Rosal, Ana B. Hungría, Juan Cabanillas-González, Daniel Jaque and Beatriz H. Juárez.
   6th Early Stage Researchers Workshop (6th ESRW)
   IMDEA Nanoscience, June 22-23rd 2016
2. "Ag/Ag_2S nanocrystals for high sensitivity near-infrared luminescence nanothermometry"
   Authors: **Diego Ruiz**, Blanca del Rosal, María Acebrón, Cristina Palencia, Chen Sun, Juan Cabanillas-González, Miguel López-Haro, Ana B. Hungría, Daniel Jaque and Beatriz H. Juárez.
   2nd Workshop on Nanoparticles for Biomedical Applications (2nd NBA)
   IMDEA Nanoscience, June 26th 2017
3. "New strategies for heat-up and hot injection synthesis of Ag_2S nanocrystals"
   Authors: **Diego Ruiz** and Beatriz H. Juárez.
   3rd International Conference on Polyol Mediated Synthesis (3rd ICPMS)
   Instituto de Ciencia de Materiales de Madrid (ICMM-CSIC), June 25-27th 2018
4. "Ag_2S-based nanocrystals as infrared emitting probes in biological applications"
   Authors: **Diego Ruiz**, Blanca del Rosal, Irene Chaves-Coira, Luis Monge, Nuria Fernández, Daniel Jaque and Beatriz H. Juárez.
   2nd Spanish Conference on Biomedical Applications of Nanomaterials (2nd SBAN)
   Instituto de Ciencia de Materiales de Madrid (ICMM-CSIC), June 6-7th 2019

Posters

1. "Synthesis and characterization of NIR emitting Ag_2S quantum dots"
   Authors: **Diego Ruiz**, María Acebrón, Alberto Martín, Roberto Otero, José M. Gallego, Daniel Jaque, Juan Cabanilllas-González and Beatriz H. Juárez.
   5th Early Stage Researchers Workshop (5th ESRW)
   IMDEA Nanoscience, June 17-18th 2015
2. "Ag/Ag_2S nanocrystals for high sensitivity near-infrared luminescence nanothermometry"
   Authors: **Diego Ruiz**, Blanca del Rosal, María Acebrón, Cristina Palencia, Chen Sun, Juan Cabanillas-González, Miguel López-Haro, Ana B. Hungría, Daniel Jaque and Beatriz H. Juárez.

7nd Early Stage Researchers Workshop (7th ESRW)

IMDEA Nanoscience, June 21-22nd 2017

3. "Ag/Ag_2S nanocrystals for high sensitivity near-infrared luminescence nanothermometry"

   Authors: **Diego Ruiz**, Blanca del Rosal, María Acebrón, Cristina Palencia, Chen Sun, Juan Cabanillas-González, Miguel López-Haro, Ana B. Hungría, Daniel Jaque and Beatriz H. Juárez.

   8th Conference on Nanoscience with Nanocrystals (NANAX 8)

   Braga (Portugal), July 3-7nd 2017

4. "Hybrid opto-magnetic nanostructures based on SPIONs and near-infrared emitting nanocrystals encapsulated in phospholipidic micelles"

   Authors: **Diego Ruiz**, Ana Espinosa, Claudia Lozano-Pedraza, Rebeca Amaro, Harrisson D. Santos, Daniel Ortega, Daniel Jaque, Francisco J. Terán and Beatriz H. Juárez

   10th International Conference on Fine Particles Magnetism (10th ICFPM)

Awards

Best oral communication award in 2nd SBAN conference

Instituto de Ciencia de Materiales de Madrid (ICMM-CSIC), June 6-7th 2019

Research interships

Research fellow given by the European Soft Matter Infrasctructure (ESMI) for the realization of the project called "Synthesis and characterization of small Ag_2S nanocrystals using a continous-flow reactor" in the Institute Of Physical Chemistry of the University of Hamburg supervised by Dra. Cristina Palencia from the group of Dr. Horst Weller.

Acknowledgements

En primer lugar, como no puede ser de otra forma, me gustaría dar las gracias a los que siempre han estado a mi lado y que cuando me han visto bajo de ánimos en este largo camino siempre me han ayudado: mis padres, Estela y mis hermanos David y Pablo. Mención aparte merece Inés por aguantarme cada día con todos los altibajos desde hace ya algún tiempo…

Por supuesto tampoco querría olvidarme de mi directora de tesis Beatriz H. Juárez por todo el apoyo y el trabajo que me ha dedicado. Sin ellos esta tesis no habría llegado a poder terminarse.

Además, también me quiero acordar de toda la gente que ha hecho de esta tesis algo más que un trabajo de investigación, desde los primeros: María, Leo, Rebeca, Héctor, Ramón, Borja, Andrés, Fernando, Cosme, Gorka, Jose hasta lo más nuevos: David, Rial, Belén, Carlos, Arturo y espero no dejarme a nadie!

Muchas gracias a todos por haberlo hecho posible!!